MUTIPLE REFLECTOR SCANNING ANTENNAS

by

Bing Shen

Dissertation submitted to the Graduate Faculty of the Virginia Polytechnic Institute and State University in partial fulfillment of the requirements for the degree

of

Doctorate of Philosophy

in

Physics

APPROVED:

Warren L. Stutzman, Chairman

L. David Roper

John R. Ficenec

Guy J. Indebetouw

Rich A. Arndt

July, 1993

Blacksburg, Virginia

Multiple Reflector Scanning Antennas

by

Bing Shen

(Abstract)

Narrow beamwidth antenna systems are important to remote sensing applications and point-to-point communication systems. In many applications the main beam of the antenna radiation pattern must be scannable over a region of space. Scanning by mechanically skewing the entire antenna assembly is difficult and in many situations is unacceptable. Performance during scan is, of course, also very important. Traditional reflector systems employing the well-focused paraboloidal-shaped main reflector accomplish scan by motion of a few feeds, or by phase steering a focal plane feed array. Such scanning systems can experience significant gain loss.

Traditional reflecting systems with a spherical main reflector have low aperture efficiency and poor side lobe and cross polarization performance. This dissertation introduces a new approach to the design of scanning spherical reflector systems, in which the performance weaknesses of high cross polarization and high side lobe levels are avoided. Moreover, the low aperture utilization common in spherical reflectors is overcome. As an improvement to this new spherical main reflector configuration, a flat mirror reflector is introduced to minimize the mechanical difficulties to scan the main beam.

In addition to the reflector system design, reflector antenna performance evaluation is also important. The temperature resolution issue important for earth observation radiometer antennas is studied, and a new method to evaluate and optimize such temperature resolution is introduced.

ACKNOWLEDGEMENTS

First, I would like to express my gratitude to my advisor Dr. Warren L. Stutzman. He provided helpful and valuable guidance in my graduate studies, my Ph. D. research and the drafting of this dissertation. I would like to thank Dr. David Roper, Dr. John Ficenec, Dr. Guy Indebetouw and Dr. Rich Arndt for their support and encouragement in my graduate research.

My work is partially sponsored by NASA Langley Research Center. My fellow graduate students in the Satellite Communication Group, Paul Werntz, Koichiro Takamizawa, Jim Lapean, Mike Barts and Marco Terada, offered great help and encouragement in my research and the preparation of this dissertation. Special thanks to my fellow graduate students in the Physics Department, Dan Korwan, Charles Moller, Scott Massie and Calvin Doss, for their support and friendship during my graduate studies.

List of Figures

LIST OF TABLES

TABLE OF CONTENTS

Chapter 1
INTRODUCTION

Narrow beamwidth antenna systems are used in applications such as point-to-point communication systems which demand high gain antennas and in remote sensing systems which require high resolution. The antenna system of choice usually employs a large main reflector antenna because of its high gain and feed system simplicity. In many applications the main beam of the antenna radiation pattern must be scannable over a region of space. In communications applications varying traffic demands dictate the scan coverage region. In remote sensing applications a scanning scenario is employed to collect data over a desired observation region. Narrow beamwidth antennas are often physically large. Scanning by mechanically skewing the entire antenna assembly is difficult and in many situations is unacceptable. For example, in space-based systems large-mass mechanical motions would disturb the space platform that might also support other systems which are vibration sensitive. It is, therefore, desirable to have a scanning system which does not involve motion of the main reflector. Then scan is accomplished through mechanical motion of the feed subassembly and/or through electronic scanning using a phased array feed.

Performance during scan is, of course, also very important. In communications gain loss over the scan range should be as small as possible, while for passive remote sensing systems constant beam efficiency during scan is usually the most important. Traditional reflector systems employing the well-focused paraboloidal-shaped main reflector accomplish scan by motion of a few feeds, or by segmental excitation of several displaced feeds, or by phase steering a focal plane feed array. Such scanning systems can experience significant gain loss [2, 3].

Traditional reflecting systems with a spherical main reflector have low aperture efficiency and poor side lobe and cross polarization performance and, therefore, are not often used. However, in theory, the spherical reflector offers the significant advantage of constant performance during scan [4]. For wide scanning, high gain systems it was worth including the spherical reflector family

in tradeoff studies. This dissertation introduces a new approach to the design of scanning spherical reflector systems, in which the performance weaknesses of high cross polarization and high side lobe levels are avoided. Moreover, the low aperture utilization common in spherical reflectors is overcome. As an improvement to this new spherical main reflector configuration, a flat mirror reflector is introduced to minimize the mechanical difficulties to scan the main beam.

The application which motivated this study is that of microwave remote sensing from a geostationary platform in support of the Mission-to-Planet-Earth program. There are significant science benefits from a geostationary antenna of the 25-m size class [5]. Of course, there are many other applications for wide-scan, high gain antenna systems [10, 11].

In order to thoroughly explain the concept of the new spherical main reflector antenna design, the basics of reflector antenna performance evaluation and design are discussed first in Chapter 2. The temperature resolution issue important for earth observation radiometer antennas is studied. In addition, a new method to evaluate and optimize such temperature resolution is introduced in Chapter 3. Chapter 4 starts the spherical reflector antenna studies by introducing previous research results. The new spherical main reflector configurations resulting from our study are explained in Chapters 5 and 6, followed by an analysis of the results in Chapter 7.

Chapter 2
BACKGROUND ANTENNA PRINCIPLES

Antennas are essential parts of all radio transmission and sensing systems. They transmit radio frequency (RF) power from the connected power source in a spatial radiation pattern. In many applications transmitted power density is required to be concentrated in a specific direction; that is, the antenna pattern should be highly directive. An antenna operating in the receiving mode must collect as much power as possible from the incident wave which arrives from a fixed direction. Except for certain special circumstances, the performance of an antenna operating in the transmission mode is identical to that during reception, i.e. antennas are reciprocal [6].

The performance of an antenna is usually quantified by its radiation pattern which includes the information to evaluate the directivity D, antenna gain G, aperture efficiency ϵ_{ap}, beam efficiency ϵ_b and cross polarization level I_p, etc; these terms are defined in Section 2.4. The overall efficiency of complex antenna systems, which includes the performance of the feeding network, will not be discussed in this document. The radiation pattern can be determined either numerically or experimentally. Numerical results are usually most cost effective and are suitable for initial evaluation and for engineering decisions involving trade-off studies. Moreover, numerical results give insight into the basics of antenna design because they can eliminate external factors such as truss structures and mechanical errors common in antenna construction. This approach permits isolation of the primary effects; secondary effects can be included in sophisticated numerical methods such as those discussed in Chapter 8. Efficient numerical techniques can be used in antenna design as well, such as to optimize an antenna configuration. With the use of optimization techniques and a high speed computer, the most cost effective antenna design satisfying the desired performance values can be determined within a matter of hours.

The most commonly used numerical method uses physical optics (PO) integration. However, this method involves numerical integration and is highly time consuming; also, it is subject to round-off error in a digital computer. Therefore, alternative methods must be available to augment PO. The most

common such approximate method is the use of geometrical theory of diffraction (GTD). The combination of PO for evaluation of far field points in the main beam and GTD for the far out scene (PO/GTD) plays an important role in analysis. Geometrical optics (GO) is used almost exclusively in reflector antenna synthesis. Although GO is exact only when the frequency approaches infinity, it produces accurate results for electrically large reflectors and is efficient and offers physical insight into the reflector antenna operation mechanisms. Therefore, GO is widely used to establish the physical model of reflector antenna systems and to estimate the performance parameters of reflector antenna systems. An example is the establishment of partial differential equations (PDE) for reflector system synthesis problems based on GO. Optimizing reflector performance by varying the parameters of the configuration is most efficiently accomplished with GO techniques.

In this chapter the PO method is discussed first, followed by a discussion of GO methods. Since GO is the essential part of our reflector antenna design method, it will be studied in detail. The consistency between GO and PO will be proved and general GO methods will be explained. Fermat's principle and its applications will be emphasized, since Fermat's principle leads to various efficient GO analysis algorithms and optimization techniques. Fermat's principle is also important to the understanding of the derivation of the PDE for our reflector antenna synthesis problem.

2.1 Basic Reflector Antenna Analysis Technique-PO

The most commonly used method in reflector pattern numerical analysis is physical optics (PO). It is a short wavelength approximation of Maxwell's equations. It includes the lowest order diffraction terms, and therefore, describes the relatively detailed wave nature of electromagnetic radiation from a reflecting surface. PO is the most accurate reflector analysis method to determine the main beam peak and near-in side lobes of a reflector antenna pattern where diffraction is the predominant effect for beam spreading. It performs especially well when the reflecting surfaces are close together such as in beam waveguide and subreflector feed assemblies, because the electrically small size and short distances of the reflecting surfaces make diffraction effects significant.

In this section the PO method is explained using Huygen's principle for wave propagation. Although PO can be derived from Maxwell's equations with the short wavelength approximation, it follows more directly from simplified physical models. The mathematical derivation of PO from Maxwell's equations was presented in [6] and [18]. Here the derivation is based on the simplified physical model of Huygen's principle, which assumes the following:

1) The reflected electromagnetic field arises from the surface current created by the field incident on the reflecting surface.

2) The reflecting surface can be divided into differential surface elements and each surface element can be modeled as a dipole (called *differential dipole*).

3) The reflected electromagnetic field can be calculated by integrating the individual electromagnetic fields caused by each differential dipole on the reflecting surface.

In the following discussion we first calculate the radiation field caused by a differential dipole and then derive the physical optics surface integral equation (PO/SI).

Figure 2-1 shows a surface current element with surface current density $\vec{J}$ and surface area $d\vec{S}$. Since dS is infinitesimal, it can be treated as being planar. The coordinate system is set up such that the x′-axis is in the same direction as $\vec{J}$. With no loss of generality, the surface element is chosen to be rectangular and the boundaries are parallel to x′ and y′ directions. Therefore, dS=dx′·dy′; moreover, the total surface current dI in the surface element is J dy′, because $\vec{J}$ is in the x′-direction and y′ is the direction perpendicular to it along the surface. If this surface current element is treated as a dipole, then the dipole carries current dI in the x′-direction and has length dx′. Thus, the dipole moment of the surface element can be written as

$$d\vec{p} = (\vec{J}\, dy')\, dx' = \vec{J}\, dS \qquad (2\text{-}1)$$

The differential dipole moment of (2-1) will cause a radiated electromagnetic field which can be written in the far field as (see (1-71) in [6])

$$d\vec{H} = \frac{1}{4\pi}\, j\beta\, \frac{e^{-j\beta R}}{R}\, d\vec{p} \times \hat{R} \qquad (2\text{-}2)$$

where $\vec{R} = R\hat{R}$ is the distance vector from the surface element dS to the far field

observation point P and $\beta=2\pi/\lambda=\frac{\omega}{c}$. Therefore, the total radiated field from the reflecting surface is

$$\vec{H} = \int\int d\vec{H} = \int\int \frac{1}{4\pi} j\beta \frac{e^{-j\beta R}}{R} d\vec{p} \times \hat{R} \qquad (2\text{-}3)$$

Substituting (2-2) into (2-3) results in the following physical optics surface integral:

$$\vec{H} = \int\int \frac{1}{4\pi} j\beta \frac{e^{-j\beta R}}{R} \vec{J} \times \hat{R}\, dS \qquad (2\text{-}4)$$

In (2-4) $\vec{R} = \vec{r} - \vec{r}'$ where $\vec{r}$ is the location of the observation point and $\vec{r}'$ is the location of the surface element dS being integrated. In the far field the only factor that depends strongly on $\vec{R}$ is $e^{-j\beta R}$; this permits simplification of (2-4). Since the far field observation point P is much farther away from the coordinate origin than the surface element dS, $r \gg r'$, we can assume that $\frac{1}{R} \simeq \frac{1}{r}$ and $\hat{R} \simeq \hat{r}$. Moreover, the phase term $e^{-j\beta R}$ can be approximated by $R \simeq r - \hat{r} \cdot \vec{r}'$. Therefore, (2-4) can be rewritten as

$$\vec{H} = \frac{1}{4\pi} j\beta \frac{e^{-j\beta r}}{r} \left\{ \int\int e^{j\beta \hat{r} \cdot \vec{r}'} \vec{J}\, dS \right\} \times \hat{r} \qquad (2\text{-}5)$$

This equation is commonly implemented in computer codes to calculate the radiated field from a surface current distribution and is referred to as the PO/SI method.

The current density on the reflecting surface, $\vec{J}$ in (2-5), is determined from the incident electric field. The assumption that $\vec{J}$ is due entirely to the incident electromagnetic field is also an approximation; there is, in general, a field scattered from the reflecting surface (especially on reflector rims) that will be reflected twice or more times. However, in most cases the scattered field is usually much weaker than the direct incident electromagnetic field. The calculation of the surface current density from the direct incident field is performed by finding the surface current that satisfies the boundary condition on a reflecting surface (assumed to be a perfectly smooth conductor), i.e. surface of a conductor with zero field inside. It is shown in [6] that the current density

satisfying this boundary condition is

$$\vec{J} = 2\,\hat{n} \times \vec{H}_{inc} \qquad (2\text{-}6)$$

where $\hat{n}$ is the surface normal and $\vec{H}_{inc}$ the incident magnetic field at the surface. Of course, $\vec{H}_{inc}$ is complex and contains the phase delay between the source and the point on the reflecting surface. In reflector antenna analysis $\vec{H}_{inc}$ is found from the pattern of the feed antenna if the reflector is directly illuminated by the feed, or it is calculated from the scatter pattern of the previous reflector in multireflector configurations.

2.2. GO Fundamentals and Fermat's Principle

In the previous section we explained how antenna patterns are obtained using PO. However, PO can require significant computing time and can be inaccurate in the far-off-axis region. More efficient algorithms must be employed in cases of repeated pattern evaluation such as in synthesis using optimization. Also, a simplified model is needed to obtain an understanding of the reflector antenna operating mechanisms. Therefore, GO becomes an essential part in reflector antenna design and analysis. We first discuss the consistency between GO and PO, and follow by introducing a new ray tracing method and its implications.

GO is the high frequency approximation of PO. The foundation of GO is Snell's law of reflection which states (see Figure 2-2) that for the incoming ray $\overline{AB}$ striking the reflecting surface at point B, the outgoing ray $\overline{BC}$ must be in the same plane with $\overline{AB}$ and the surface normal at point B, $\hat{n}$; moreover, the included angle between $\overline{BC}$ and $\hat{n}$ is the same as that between $\overline{AB}$ and $\hat{n}$. Snell's law (stated as "The angle of reflection equals the angle of incidence") is a well-known principle and is one of the most important properties of wave propagation and is a consequence of PO. In order to understand the relationship between Snell's law and PO, we must first introduce another famous theorem, Fermat's principle.

2.2.1 Derivation of Fermat's Principle from PO

Fermat's principle states that for the ray emitted from a source located at

point A, reflected by the reflecting surface at point B and finally being received at point C, the total length of $\overline{AB}+\overline{BC}$ (*optical path length*) must be extremum, and is minimum in most applications, including the scope of this dissertation. In other words, as the reflection point moves from B along the reflecting surface to point B′, which does not satisfy Snell's law, then $\overline{AB'}+\overline{B'C}>\overline{AB}+\overline{BC}$, see Fig. 2-2. Mathematically, Fermat's principle holds only when the reflecting surface is second order differentiable; that is, when the surface is smooth without discontinuities. Fermat's principle is more general than Snell's law. We will first prove Fermat's principle from PO, followed by proof of Snell's law from Fermat's principle. The implications of Fermat's principle in reflector antenna system design is discussed in the next section.

Although Fermat's principle was known before the wave nature of light was discovered, it remains a useful result of wave propagation. As a high frequency approximation for wave functions, it simplifies the wave propagation model and is, therefore, widely used in optical system design and for studies of wave propagation in continuous media. Here we show the consistency between Fermat's principle and electromagnetic theory by deriving Fermat's principle from PO.

Consider a region surrounding the reflection point B in Fig. 2-2. Implicit in the use of a ray is the assumption that the wavelength, λ, of the incident beam is much smaller than any other dimensions of interest. As in deriving the PO integration formula, we divide the reflecting surface into small surface elements with surface area ΔS such that the surface element is small compared with the size and curvature of the reflecting surface, therefore, it can be treated as flat and the surface current on it has constant amplitude and polarization. Yet, this surface element differs from the one used for PO discussion in that it is much larger than the wavelength, i.e. $\Delta S \gg \lambda^2$. Hence, the surface element here cannot be treated as a short dipole and the phase variation on the surface element is important. The foregoing conditions must hold for GO to be valid and are summarized as follow:

1) Amplitude and polarization variation on the reflecting surface are slow, so that the amplitude and polarization can be treated as constants in regions with size $\gg \lambda$. This implies a reflector's size $\gg \lambda$.

2) The radius of curvature of the reflecting surface $\gg \lambda$, so that the regions with constant amplitude and polarization can be treated as flat.

The radiation at point C in Fig. 2-2 arising from the surface element ΔS induced by a source located at point A can be calculated from the PO integral of (2-4) as

$$\vec{H} = \int\int_{\Delta S} \frac{1}{4\pi} j\beta \frac{e^{-j\beta|\vec{r}_C - \vec{r}'|}}{|\vec{r}_C - \vec{r}'|^2} \vec{J} \times (\vec{r}_C - \vec{r}') \, dS \qquad (2\text{-}7)$$

where $\vec{r}'$ is the location of dS in integration. The surface current $\vec{J}$ is assumed to be constant in amplitude and polarization over ΔS, $\vec{J} = \vec{J}_0 \, e^{-j\beta|\vec{r}_A - \vec{r}'|}$. The locations of the points A, B′ and C are referenced to a fixed origin (not shown in Fig. 2-2) as illustrated in Fig. 2-1 and are denoted $\vec{r}_A$, $\vec{r}$, and $\vec{r}_C$. Substituting this surface current into (2-7) yields

$$\begin{aligned} H &\propto \int\int_{\Delta S} e^{-j\beta|\vec{r}_C - \vec{r}'|} e^{-j\beta|\vec{r}_A - \vec{r}'|} dS \\ &= \int\int_{\Delta S} e^{-j\beta(\overline{B'C} + \overline{AB'})} dS \end{aligned} \qquad (2\text{-}8)$$

where B′ is the point at the terminus of $\vec{r}'$ that locates the integration variable dS. The other factors in (2-7) are ignored because they are constant due to the small size of ΔS. We introduce the notation $\delta(\overline{B'C}+\overline{AB'})$ for the change of $(\overline{B'C}+\overline{AB'})$ as B′ moves within ΔS. It is obvious that as $\beta \to \infty$, even small $\delta(\overline{B'C}+\overline{AB'})$ will cause a large phase variation in the region of ΔS and the integral of (2-8) will approach zero. Therefore, it is necessary to have $\delta(\overline{B'C}+\overline{AB'})=0$ within the surface element ΔS in order that (2-8) contributes to the amplitude of the reflected field at point C. On the other hand, the whole reflector surface is divided into many small elements among which only the surface element that satisfies $\delta(\overline{B'C}+\overline{AB'})=0$ will be responsible for the reflected field to point C from a source at A; and this surface element ΔS is located by point B on the reflector surface. We use the notation $\delta(\overline{BC}+\overline{AB})$ for the change of $\overline{BC}+\overline{AB}$ when B moves an infinitesimal amount on the surface of the reflector (this movement of point B is referred to as $\delta\vec{r}_B$); then point B must satisfy $\delta(\overline{BC}+\overline{AB})=0$ (strictly, this should be written as $\delta(\overline{BC}+\overline{AB})=O(\delta\vec{r}_B)$). That is a

statement of Fermat's principle of minimum path for a reflection point; it was derived here from PO.

The pattern values obtained from PO approach the GO approximation gradually as frequency is increased. In order to calculate the field at point C reflected by the reflecting surface and originating from a source at point A, it is in general necessary to PO integrate the induced current on the whole reflecting surface; however, when the frequency is very high, it is sufficient to carry out the PO integration on a small surface element ΔS that is located at point B satisfying Fermat's principle. In GO sense the surface element ΔS is infinitely small, but as the frequency decreases ΔS must increase in order to offer reasonable accuracy for the PO integration; when the ΔS reaches the size close to the whole reflecting surface, the transition is made from GO to PO.

2.2.2 Applying Fermat's Principle to Multiple Reflectors

Although ΔS is important in the transition between GO and PO, it is never used when GO is performed. GO only involves ray reflectional points, such as B in Fig. 2-2. With the powerful tool of GO, the reflected radiation field can be conveniently derived from ray tracing without integration. Ray tracing in reflecting systems uses Snell's law. However, Snell's law describes a local phenomenon that does not reveal the relationship between adjacent rays. More sophisticated ray tracing methods based on Fermat's principle are necessary to analyze optical systems and reflector antenna systems where a bundle of rays must be traced to evaluate the performance such as aperture field distribution and phase error, or to establish a physical model for reflector antenna synthesis problems such as the PDE method discussed in Chapter 6. In the following discussion, we will prove Snell's law from Fermat's principle to show that the more general Fermat's principle is indeed consistent with Snell's law, and more importantly, to derive the mathematical formulation of Fermat's principle for our future discussion of GO methods.

The geometry for the ray tracing problem is shown in Fig. 2-3. A ray emerging from a source located at point P_0 reflects from the first reflector at point P_1, then from the second reflector at P_2 and so on, finally it is reflected by

the n'th reflector at P_n and is received at an observation point at P_{n+1}. Points $\{P_n\}$ are located in space at the terminus points of vectors $\{\vec{r}_n\}$ from a fixed origin O. The problem is to find the reflection points P_1, P_2, ..., P_n that satisfy Fermat's principle once the source point P_0, the observation point P_{n+1} and all the reflectors are specified. Fermat's principle requires that the total path length L of $\overline{P_0P_1P_2...P_{n+1}}$ be minimum. An equivalent statement is that the partial derivatives of L with respect to the movements of P_1, P_2, ..., P_{n+1} that are constrained to reflector surfaces must be zero. Using the symbol $\nabla_i = \frac{\partial}{\partial \vec{r}_i}$ for the gradient of L with respect to the coordinates of P_i, $\vec{r}_i$, the change of L is

$$dL = \nabla_0 L \cdot d\vec{r}_0 + \nabla_1 L \cdot d\vec{r}_1 + ... + \nabla_{n+1} L \cdot d\vec{r}_{n+1} \qquad (2\text{-}9)$$

We use the symbol $\delta\vec{r}_i$ for $d\vec{r}_i$ (i=1, ..., n) constrained to the surface of the i'th reflector, and δL for dL subject to any change of $\delta\vec{r}_i$ (i=1, ..., n); then Fermat's principle becomes

$$\delta L = \nabla_1 L \cdot \delta\vec{r}_1 + \nabla_2 L \cdot \delta\vec{r}_2 + ... + \nabla_n L \cdot \delta\vec{r}_n = 0 \qquad (2\text{-}10)$$

which is a general ray tracing equation for n reflectors and is equivalent to $\nabla_i L \cdot \delta\vec{r}_i = 0$ (i=1, ..., n) because any $\delta\vec{r}_i$ in (2-10) is an independent variable. Notice that $\vec{r}_0$ and $\vec{r}_{n+1}$ are left out in (2-10) because they are fixed as source and observation points when variation takes place to verify Fermat's principle. In order to prove Snell's law, the following explicit expression is first derived for the gradients in (2-10):

$$\begin{aligned} \nabla_i L &= \nabla_i \left(\sum_{j=1}^{n+1} |\vec{r}_j - \vec{r}_{j-1}| \right) \\ &= \nabla_i \left(|\vec{r}_i - \vec{r}_{i-1}| + |\vec{r}_{i+1} - \vec{r}_i| \right) \\ &= \hat{t}_i - \hat{t}_{i+1} \end{aligned} \qquad (2\text{-}11)$$

where $\hat{t}_i = \frac{\vec{r}_i - \vec{r}_{i-1}}{|\vec{r}_i - \vec{r}_{i-1}|}$ is the unit vector from P_{i-1} to P_i. This in (2-10) yields

$$(\hat{t}_i - \hat{t}_{i+1}) \cdot \delta\vec{r}_i = 0 \qquad \text{for i=1.....n} \tag{2-12}$$

which means that $(\hat{t}_i - \hat{t}_{i+1})$ has to be perpendicular to $\delta\vec{r}_i$ in order to satisfy Fermat's principle. Since $\delta\vec{r}_i$ is along any direction on the surface of the i'th reflector at point $\vec{r}_i$, $(\hat{t}_i - \hat{t}_{i+1})$ must be perpendicular to the surface of the i'th reflector at point $\vec{r}_i$. Therefore,

$$(\hat{t}_i - \hat{t}_{i+1}) \times \hat{n}_i = 0 \tag{2-13}$$

where $\hat{n}_i$ is the surface normal of the i'th reflector at point P_i. It is obvious that (2-13) is Snell's law because $\hat{t}_i$ and $\hat{t}_{i+1}$ are directions of the incident and reflected rays and $\hat{n}_i$ is the surface normal at the point of reflection. Hence, Snell's law is proved from Fermat's principle.

If instead of using classical Snell's-law-based ray tracing, one uses Fermat's principle of (2-10), the reflector design problem becomes an optimization problem. That is, a ray tracing problem in an n-reflector system can be stated as follows: find a ray that is represented by the vector ($\vec{r}_0$, $\vec{r}_1$, ..., $\vec{r}_{n+1}$) which minimizes the total path length L subject to the constraint that $\vec{r}_i$ (i=1, 2, ..., n) has to be on the surface of the i'th reflector. Note that we are specifying points not ray directions as in classical ray optics. (2-10) can be solved by numerical minimization of the optical path such as Newton's method to find the roots of $\nabla_i L \cdot \delta\vec{r}_i = 0$ (i=1, ..., n). The fact that (2-10) is solvable leads to functional relationships

$$\vec{r}_i = \vec{r}_i\,(\vec{r}_0, \vec{r}_{n+1}) \qquad \text{for i=1, ..., n} \tag{2-14}$$

except the cases for $\vec{r}_0$ and $\vec{r}_{n+1}$ being the object and the corresponding image point in a imaging reflector system, for example when $\vec{r}_0$ and $\vec{r}_{n+1}$ are two focal points of an elliptical reflector or when $\vec{r}_0$ is the focal point of a parabolic reflector and $\vec{r}_{n+1}$ is at ∞. Fermat's principle in the mathematical form of (2-10) is a powerful tool. In the next section, we will use this general mathematical formulation of Fermat's principle to show:

1) The equal-path-length law in a reflector system with parallel ray output from the aperture.

2) A method to solve for the shape of a reflector surface from the equal-path-length law and the known shapes of other reflectors in a multireflector system.

3) Field intensity calculation based on ray tracing.

2.3. Applications of Fermat's Principle

In the last section we showed that Fermat's principle, which is a classical GO result, is consistent with PO. We also derived the general mathematical formulation of GO based on Fermat's principle. In this section the general formulation of (2-10) is used to prove some of the most fundamental theorems used in GO-based reflector antenna synthesis/analysis.

The equal-path-length law in a reflector antenna system

The equal-path-length law is one of the most fundamental principles in reflector antenna design. It states that for a reflector system which consists of a feed and multiple reflectors, the total path length from the feed to the aperture (the plane that is perpendicular to the output rays) is the same for all rays if and only if the output rays from the final reflector (the main reflector) are parallel. The proof begins by assuming that one ray satisfies (2-10); this ray emerges from the feed location $\vec{r}_0$, and strikes the main reflector aperture at point $\vec{r}_{n+1}$; see Fig. 2-3. Once this ray (the *initial ray*) is found, an aperture plane is erected perpendicular to this ray. We use the symbol $\delta\vec{r}_{n+1}$ for any variation of $\vec{r}_{n+1}$ constrained to this aperture plane. Then the total variation of the path length becomes

$$\delta L = \nabla_1 L \cdot \delta\vec{r}_1 + \nabla_2 L \cdot \delta\vec{r}_2 + \ldots\ldots + \nabla_n L \cdot \delta\vec{r}_n + \nabla_{n+1} L \cdot \delta\vec{r}_{n+1} \,. \quad (2\text{-}15)$$

This relation is a generalization of (2-10). In (2-10) only $\vec{r}_1$, ..., $\vec{r}_n$ are allowed to change and $\vec{r}_{n+1}$ is fixed, but all n+1 points are free to move in (2-15). Of course, if a ray satisfies Fermat's principle, then the first n terms in (2-15) are zero as stated in (2-10). Therefore, for any set of points, $\vec{r}_1$, ..., $\vec{r}_n$ and $\vec{r}_{n+1}$, forming a ray originated at $\vec{r}_0$ that satisfies Fermat's principle (2-10), the total path length variation in (2-15) can be reduced to

$$\delta L = \nabla_{n+1} L \cdot \delta\vec{r}_{n+1} \quad (2\text{-}16)$$

In a manner similar to (2-11),

$$\nabla_{n+1} L = \hat{t}_{n+1} \tag{2-17}$$

This in (2-16) gives

$$\delta L = \hat{t}_{n+1} \cdot \delta \vec{r}_{n+1} \tag{2-18}$$

Parallel rays exiting the aperture plane, $\{\hat{t}_{n+1}\}$, are also perpendicular to this aperture plane since the initial ray is. Also since $\{\delta \vec{r}_{n+1}\}$ are confined to the aperture plane, then $\delta L=0$ by (2-18). In other words, when exiting rays are parallel, the total path length for all rays are identical (e.g. "equal path length"). Conversely, if the path length is constant for all rays, $\delta L=0$, then $\hat{t}_{n+1}$ of the ray that passes through any point $\vec{r}_{n+1}$ in the aperture must be perpendicular to $\delta \vec{r}_{n+1}$ according to (2-18); therefore, all output rays are parallel.

In the above discussion, we proved the equivalence between parallel output rays and equal path length. This equivalence can be expressed more generally in both PO and GO terms. In the PO sense, this equivalence is stated as: a uniform aperture phase distribution is the necessary condition for a plane wave output. In the GO sense it shows the underlying equivalence between length-measuring Fermat's principle and angle-measuring Snell's law, which applies not only to plane wave output, but also to a general wave front output, such as a spherical wave output. This equivalence theorem has direct usage in practice. For example, calculation of the path length error gives a estimate for the aperture phase error in a reflector antenna system. An important application of this theory appears in reflector antenna design which usually requires a uniform phase in the aperture plane. Path length error is often evaluated by the aperture output ray pointing error, which is equivalent and more accurate; this is easily seen in (2-18). This equivalence theorem will be repeatedly used in this dissertation.

Solving for the shape of one unknown reflector in a multireflector system

Fermat's principle can also be used in shaped reflector synthesis. It reduces the number of degrees of freedom in the reflector shape synthesis problem once the equal path length law restriction is imposed, and therefore, simplifies the reflector shape synthesis process. In general, the equal-path-length law is a necessary, not sufficient, condition for satisfaction of Fermat's principle; this is because Fermat's principle of (2-10) requires the path length variation to

be zero on each reflector, i.e. $\nabla_i L \cdot \delta\vec{r}_i = 0$ (i=1, ..., n) on each reflector where L is a function of independent variables $\vec{r}_1$, ..., $\vec{r}_n$. That is, the equal-path-length law only states that the total path length variation is zero, which does not guarantee that the variation on each reflector is zero, i.e. each term in (2-10) must be zero. However, the equal-path-length law can be used as a constraint in the reflector system design that eliminates one independent variable among $\vec{r}_1$, ..., $\vec{r}_n$; so to synthesize an n-reflector system is equivalent to determining the shapes of $n-1$ reflectors, and the remaining one is automatically determined.

The theorem for the determination of the shape of one reflector in an n-reflector system with n-1 shapes given is as follows: In an n-reflector system if there is a set of rays with equal path lengths that satisfy zero path length variation on $n-1$ reflectors, then zero path length variation is also satisfied on the remaining reflector. The proof of this theorem is rather obvious. Without loss of generality, we assume that the reflector to be determined is the first one. Returning to (2-15), we see that if $\nabla_i L \cdot \delta\vec{r}_i = 0$ for i=2, ..., n+1 and if $\delta L = 0$, then $\nabla_1 L \cdot \delta\vec{r}_1 = 0$, and thereby, proving the theorem.

This theorem has profound consequences for reflector shape synthesis. For example, in a spherical dual reflector system, the shape of the subreflector can be found by calculating the total path length from the feed to the aperture to correct for spherical aberration and Snell's law on the subreflector will be automatically satisfied. This method will be discussed in Chapter 3 for the spherical dual-reflector system synthesis performed by Holt [8]. In the synthesis of the new spherical tri-reflector system in Chapter 6, this theorem is used to reduce the number of parameters in the synthesis equation so that a partial differential equation becomes an ordinary differential equation.

Field intensity calculation

GO as the high frequency approximation of PO is often used to calculate ray directions, but it can also be extended to evaluate the field amplitude of electromagnetic radiation. In this section we discuss how the information obtained from ray tracing can be used to calculate the aperture field distribution of a reflector antenna system. The tool for this calculation is the *mapping function*

which is derived from the ray correspondence between the feed antenna field and the aperture field. This concept can be easily generalized to other situations such as to the calculation of the far field of antenna radiation. We will limit our discussion to field intensity calculation and will not include polarization. However, polarization effects can be included; in fact, the aperture cross polarization amplitude can be found using ray tracing.

Ray tracing establishes the correspondence between feed angles and points in the aperture of a reflector antenna system. In Fig. 2-3 we see that there is only one ray which starts at feed point $\vec{r}_0$ in the direction $\hat{t}_1$, reflects from the reflectors and then exits the aperture at point $\vec{r}_{n+1}$. This gives a functional relationship between $\hat{t}_1$ and $\vec{r}_{n+1}$ that is written as $\vec{r}_{n+1}(\hat{t}_1)$ and is called the ***mapping function.*** A ray cone at the feed and centered on the direction $\hat{t}_1$ will strike the aperture in a contour centered at $\vec{r}_{n+1}$. The area enclosed by this contour on the aperture is related to the size of the feed ray cone as follows:

$$dA = \left| \frac{\delta \vec{r}_{n+1}}{\delta \hat{t}_1} \right| d\Omega \tag{2-19}$$

where dA is the aperture differential area and $d\Omega$ is the differential solid angle surrounding the feed ray. $|\delta \vec{r}_{n+1}/\delta \hat{t}_1|$ in (2-19) is the Jacobian factor of the mapping function $\vec{r}_{n+1}(\hat{t}_1)$. If $\vec{r}_{n+1}$ in the aperture plane is described by cylindrical coordinates (ρ, ψ, z) with z=0 for the aperture plane, and $\hat{t}_1$ is described by spherical coordinates (r, θ_f, ϕ_f) with r=1 and centered at the feed point $\vec{r}_0$, then the Jacobian factor becomes

$$\left| \frac{\delta \vec{r}_{n+1}}{\delta \hat{t}_1} \right| = \rho \begin{vmatrix} \frac{\partial \rho}{\partial \theta_f} & \frac{\partial \psi}{\partial \theta_f} \\ \frac{\partial \rho}{\partial \phi_f} & \frac{\partial \psi}{\partial \phi_f} \end{vmatrix} \tag{2-20}$$

Therefore, (2-19) in these coordinates becomes

$$dA = \rho \cdot \begin{vmatrix} \frac{\partial \rho}{\partial \theta_f} & \frac{\partial \psi}{\partial \theta_f} \\ \frac{\partial \rho}{\partial \phi_f} & \frac{\partial \psi}{\partial \phi_f} \end{vmatrix} d\Omega_f \tag{2-21}$$

But since, in GO, power is confined within ray tubes, the power contained within the feed ray cone ($d\Omega$) is the same as the power striking the corresponding the aperture circular area (dA). This assumption of power conservation is based on the high frequency assumption of GO and is generally accepted in reflector antenna synthesis procedures [14]. The results are reasonably close to that from PO analysis. Based on the power conservation assumption, we have (in the coordinate system described above),

$$I(\rho, \psi)\, dA = U(\theta_f, \phi_f)\, d\Omega_f \qquad (2\text{-}22)$$

where I is the aperture radiation flux density (*aperture intensity*) and U is the feed radiation intensity. Substituting (2-21) into (2-22) we have

$$I(\rho, \psi) = U(\theta_f, \phi_f) \,/\, \{\, \rho \cdot \begin{vmatrix} \frac{\partial \rho}{\partial \theta_f} & \frac{\partial \psi}{\partial \theta_f} \\ \frac{\partial \rho}{\partial \phi_f} & \frac{\partial \psi}{\partial \phi_f} \end{vmatrix} \} \qquad (2\text{-}23)$$

which will be used repeatedly in this dissertation, for example, to establish the mapping relationship of (5-7). Equation (2-23) offers a method to analyze the aperture intensity distribution in a reflector antenna system, which can be used to optimize the aperture distribution by synthesizing the antenna system with desired mapping to generate low cross polarization, low side lobe levels and high beam efficiency [14].

2.4 Antenna Performance Parameters (Gain, HP, SLL, ϵ_{ap}, XPOL)

In this section we define and discuss basic parameters used to evaluate antenna performance; they are summarized in Table 2-1. The angular variation of the power intensity of a transmitting antenna is often quantified with $U(\theta, \phi)$, which is the radiated power per unit solid angle:

$$U(\theta, \phi) = \frac{dP_r(\Omega)}{d\Omega} \qquad (2\text{-}24)$$

where $P_r(\Omega)$ is the radiated power contained within a solid angle Ω. The

directivity of an antenna, $D(\theta, \phi)$, is a measure of how much the radiation is concentrated in specific directions, and is defined by

$$D(\theta, \phi) = \frac{U(\theta, \phi)}{U_{average}} \tag{2-25}$$

where $U_{average}$ is the average radiation intensity over 4π solid angle, or

$$U_{average} = \frac{P_0}{4\pi} \tag{2-26}$$

where P_0 is the total radiated power from the antenna. The gain of the antenna includes the effect of the loss on the antenna structure and relates to the directivity as follows

$$G(\theta, \phi) = e_r \, D(\theta, \phi) \tag{2-27}$$

where e_r is the radiation efficiency and includes loss effects in the feed network. In practical reflector antenna systems, $e_r \simeq 1$, therefore, $G(\theta, \phi) \simeq D(\theta, \phi)$. In this dissertation, we assume lossless conditions and then gain and directivity are identical.

The antenna gain as a function of direction (or gain pattern), $G(\theta, \phi)$, is the most important antenna performance parameter. The peak gain value, G_0, is often called just gain. The related angular variation normalized to unity maximum, $F(\theta, \phi)$, is called the *antenna pattern*, and then

$$G(\theta, \phi) = G_0 \, F(\theta, \phi) \, . \tag{2-28}$$

Smoothly varying antenna patterns are well represented by *principal plane pattern cuts*, $F(\theta, \phi=0^\circ)$ and $F(\theta, \phi=90^\circ)$. Several important parameters can be extracted from the antenna pattern, such as gain (G_0), side lobe level (SLL) and half power beamwidth (HP). Table 2-1 lists the definition of these parameters.

The Gain, G_0, is related to the physical aperture area of the antenna. With uniform phase excitation on the aperture, an antenna will be most directive when the aperture is uniformly illuminated; then the gain is [6]:

$$G_u = \frac{4\pi}{\lambda^2} A_p \tag{2-29}$$

where A_p is the physical area of the antenna aperture. G_u in (2-29) is an upper

bound for the achievable gain of an antenna with physical aperture area A_p. A practical antenna will have a lower gain; and this is represented through

$$G_0 = \epsilon_{ap}\, G_u \qquad (2\text{-}30)$$

where ϵ_{ap} is called *aperture efficiency*, and has value in (0, 1).

The vector nature of antenna radiation is represented with orthogonally polarized components and their associated patterns. For these orthogonal polarizations one is usually wanted and the other unwanted; these are called co- and cross-polarization, respectively. The associated gain patterns are $G(\theta, \phi)$ and $G_x(\theta, \phi)$. It is usually desired to keep the cross-polarization level as low as possible compared to the co-polarized radiation. This is quantified through a single parameter called *cross-polarization level*, XPOL, and is defined as the ratio of peak co-pol gain to the peak cross-pol gain; see Table 2-1.

The parameters listed in Table 2-1 are the most popular quantities used to characterize antennas for communication links and radar applications. However, these parameters are not sufficient to evaluate radiometer antennas for remote sensing and radio astronomy applications. In Chapter 3, a new parameter, beam efficiency, will be introduced, which is more appropriate to radiometer antennas. In addition to beam efficiency, we introduce another parameter, *residue beam efficiency ratio*, which directly specifies the temperature measurement accuracy of a radiometer antenna.

Table 2-1

Common Antenna Performance Parameters

Parameter	Definition	Calculation
$G(\theta, \phi)$	Gain pattern	$G(\theta, \phi) = \frac{4\pi}{P_0} \frac{dP_r(\Omega)}{d\Omega}$ P_0 = total radiated power P_r = radiated power contained in Ω
G_0	Peak gain of an antenna	$G_0 = \max[G(\theta, \phi)]$ $= G(0, 0)$
$F(\theta, \phi)$	Normalized antenna pattern	$F(\theta, \phi) = \frac{G(\theta, \phi)}{G_0}$
SLL	Side lobe level: the ratio of the maximum pattern gain value outside the main lobe to the peak gain	$SLL = \max[G(\theta, \phi)] \ / \ G_0$ $(\theta,\phi) \notin$ main lobe
HP	Half power beamwidth: the angular separation of points on the main lobe where the power pattern falls to half value	$HP = \theta_1 + \theta_2$ where $G(\theta_1, \phi) = G_0/2$ and $G(\theta_2, \phi + \pi) = G_0/2$
ϵ_{ap}	Aperture efficiency	$\epsilon_{ap} = G_0 \ / \ [\ \frac{4\pi}{\lambda^2} A_p\ ]$
XPOL	Cross polarization	$XPOL = G_0 \ / \ \max[G_x(\theta, \phi)]$

Chapter 3
BEAM EFFICIENCY AND TEMPERATURE SENSITIVITY

In Section 2.4 we discussed the commonly used pattern parameters of gain, half-power beamwidth, side lobe level and cross polarization. For remote sensing applications, the additional parameter of beam efficiency is needed to fully characterize system performance. In this chapter we discuss the importance of beam efficiency and its relationship to the temperature sensitivity of a remote sensing antenna. To overcome the difficulties common in beam efficiency calculations, we introduce a simplified model that is used to evaluate the temperature sensitivity of earth observing radiometers. We also propose methods to optimize the temperature sensitivity and estimate the overall noise performance of these antennas.

3.1 Difficulties in Beam Efficiency Calculation

Beam efficiency is the most important performance evaluation parameter for a radiometer antenna. It is defined as the fraction of the total radiated power that is contained in the main beam:

$$\eta_b = \frac{1}{P_0} \int\int_{\Omega_{main}} U(\theta, \phi)\, d\Omega \qquad (3\text{-}1)$$

where P_0 is the total radiated power and Ω_{main} is the solid angle for the main beam. Using the definition of gain in (2-27) and (2-25), this can also be expressed as

$$\eta_b = \frac{1}{4\pi} \int\int_{\Omega_{main}} G(\theta, \phi)\, d\Omega \qquad (3\text{-}2)$$

Beam efficiency is usually calculated by direct evaluation of (3-2). This approach, however, can introduce error because of the inaccuracies in the numerical evaluation of $G(\theta, \phi)$. For example, direct PO evaluation of $G(\theta, \phi)$ can yield as much as 2% error in the beam efficiency value calculated with (3-2) [19].

In Section 3.2 a new method will be introduced to overcome the inaccuracies in beam efficiency evaluation of (3-2). The new method uses an alternate form of (3-2), which is derived by using the normalized pattern as in (2-28):

$$\eta_b = \frac{G_0}{4\pi} \int\int_{\Omega_{main}} F(\theta, \phi)\, d\Omega \qquad (3\text{-}3)$$

The pattern $F(\theta, \phi)$ can be evaluated with high accuracy near the main beam axis [19] but a remaining source of error is the accuracy of G_0. We will exploit the accuracy of $F(\theta, \phi)$ to calculate the temperature sensitivity in Section 3.2.

Another problem associated with (3-2) is the definition of main beam. Several methods are in use to define the main beam. One straight forward method is to use the first null at the edges of the main beam to define the main beam extent. Another popular method is to use the solid angle of cone angle 2.5 times the half-power beamwidth. Both methods have disadvantages for radiometers. This point will be explored further in the following discussion for integrated pattern functions.

The concept of beam efficiency can be generalized to integrated pattern functions. In the beam efficiency definition of (3-1), the integral is performed over the solid angle of the main beam. A generalized form of pattern integral is the fraction of the total radiated power contained in any specified solid angle:

$$\eta(\Omega) = \int\int_{\Omega} U(\theta, \phi)\, d\Omega \,/P_0 = \frac{1}{4\pi} \int\int_{\Omega} G(\theta, \phi)\, d\Omega \qquad (3\text{-}4)$$

This fraction of power as a function of Ω, $\eta(\Omega)$, is called *integrated pattern function.*

This definition of integrated pattern function is very general and contains all antenna pattern information because Ω can change in both size and shape. For simplicity, the shape of Ω is taken to be conical, with its axis along the main beam axis and the size specified by spherical polar angle θ away from its axis. With this simplified definition, the integrated pattern function can be written as

$$\eta(\theta) = \frac{1}{4\pi} \int_0^{\theta} \sin\theta\, d\theta \int_0^{2\pi} G(\theta, \phi)\, d\Omega$$

$$= \frac{G_0}{4\pi} \int_0^{\theta} \sin\theta \, d\theta \int_0^{2\pi} F(\theta, \phi) \, d\Omega \qquad (3\text{-}5)$$

The integrated pattern function is illustrated with an example of a large gain reflector antenna. The reflector for the example is axisymmetric, with a 1000λ diameter and $F/D = 2.0$, and is fed with a Gaussian feed which has a taper of -17.5 dB at the reflector rim. Fig. 3-1 shows the integrated pattern function of the example prime focus paraboloidal antenna, and Fig. 3-2 shows the integrated pattern function of the same antenna with a distorted main reflector. The distortion is that the main reflector has wrong focal length which is 100λ longer than the vertex-to-feed distance. The gain of the distorted reflector is 10 dB lower than the undistorted reflector. In spite of this performance degradation, the distorted reflector has a beam efficiency value close to the undistorted reflector, because its main beam solid angle for the boundary of integration in (3-2) is much larger than the undistorted one. In practice, it is desirable to use the solid angle of the desired object in the beam efficiency integration; this definition is called *object extent beam efficiency.* The integrated pattern function offers a way to evaluate the object extent beam efficiency for objects with various angular extent, which is done by evaluating the integrated pattern function at the solid angle of the desired object.

It is difficult to obtain accurate values for integrated pattern functions because of the accuracy of G_0. Traditionally the integrated pattern function is used directly to estimate the temperature measurement accuracy of a radiometer antenna. In the following discussion, we first introduce the concept of antenna temperature, then explain the temperature distribution model for earth observation which leads to a method to overcome the error of integrated pattern functions in evaluating the temperature measurement accuracy.

3.2. Temperature Distribution Model for Earth Observation Antennas

A radiometer antenna receives noise power from its surrounding environment. The spectral power density of the noise received by the antenna is

characterized by *antenna noise temperature* (or just *antenna temperature*) [17]:

$$T_a = \frac{1}{4\pi} \int\int_{4\pi} T(\theta, \phi)\, G(\theta, \phi)\, d\Omega \qquad (3\text{-}6)$$

where $T(\theta, \phi)$ is the temperature distribution of the environment. Of course, the greatest contribution to the antenna temperature arises from the main beam near θ=0; thus, the object to be observed is usually located at θ=0 direction, and the antenna temperature measured by the radiometer is used to approximate the temperature of the object. However, since $G(\theta, \phi)$ is not zero outside the main beam, the antenna temperature is affected by the noise outside the observed object.

The earth observation problem is modeled by the following three temperature regions shown in Fig. 3-3: a pixel of solid angle Ω_p and temperature T, the remaining portion of the earth with uniform temperature $T+\delta T$ and solid angle $\Omega_e' = \Omega_e - \Omega_p$, and off-earth cosmic background of uniform temperature T_0 and solid angle $4\pi - \Omega_e$. Using this model, the antenna temperature of (3-6) becomes

$$T_a = \frac{T}{4\pi} \int\int_{\Omega_p} G(\theta, \phi)\, d\Omega + \frac{T+\delta T}{4\pi} \int\int_{\Omega_e'} G(\theta, \phi)\, d\Omega + \frac{T_0}{4\pi} \int\int_{4\pi-\Omega_e} G(\theta, \phi)\, d\Omega \qquad (3\text{-}7)$$

Using the integrated pattern function of (3-4), (3-7) can be written as

$$\begin{aligned} T_a &= T\eta(\Omega_p) + (T+\delta T)\eta(\Omega_e') + T_0\eta(4\pi - \Omega_e) \\ &= T\eta_p + (T+\delta T)\eta_r + T_0\eta_s \end{aligned} \qquad (3\text{-}8)$$

$\eta(\Omega_p)=\eta_p$ is called *pixel beam efficiency* because it refers to the fraction of the total radiated power contained in the solid angle of the desired pixel. $\eta(\Omega_e')=\eta_r$ is called the residue beam efficiency and refers to the fraction of the total radiated power toward the portion of the earth outside the pixel, which is the main source of measurement error. η_r is based on near main beam side lobes that can be evaluated by PO method. $\eta(4\pi - \Omega_e)=\eta_s$ is called spillover beam efficiency because it is caused by the radiated power from the antenna not striking the

earth. We want to measure the temperature of the pixel, T, using the antenna temperature, T_a, which is measured by the radiometer. Solving (3-8) for the pixel temperature gives:

$$T = [T_a - (T+\delta T)\eta_r - T_0\eta_s]/\eta_p \qquad (3\text{-}9)$$

The temperature measurement error of the radiometer depends on the error of each term in (3-9). In most remote sensing applications for beam scanning or imaging, the most important quantity is the smallest resolvable temperature difference between different pixels. The absolute temperature measurement accuracy is also important, but it has a much higher tolerance to error. It is analogous to an imaging system that has small error tolerance for contrast but large error tolerance for brightness. The temperature resolution that reflects such contrast is defined as follows:

$$R = \max(T_{a1} - T_{a2})|_{T_1 = T_2} \qquad (3\text{-}10)$$

where T_1 and T_2 are the real temperature values of pixels 1 and 2, and T_{a1} and T_{a2} are the antenna temperature values corresponding to these two pixels. Equation (3-10) refers to the maximum possible antenna temperature difference for two pixels on the earth with identical temperature values. This temperature difference is caused by the second and third terms in (3-8), which are caused by the near side lobe pointing towards the remainder of the earth and the spillover of the antenna beam outside the earth. Substituting (3-8) into (3-10), we obtain the following expressing for R:

$$R = \max\{\delta[(T + \delta T)\eta_r + T_0\eta_s]\} \qquad (3\text{-}11)$$

where the operator $\max\{\delta[\cdot]\}$ refers to the maximum variation of the quantity when the antenna scans across the earth's surface. To further simplify the temperature resolution model, we rewrite the variation in (3-11) as

$$\delta[(T+\delta T)\eta_r + T_0\eta_s] = T\ \delta\eta_r + \delta T\ \eta_r + \delta T\ \delta\eta_r + \delta(T_0\eta_s) \qquad (3\text{-}12)$$

The quantities used in (3-12) are summarized in Table 3-1 along with typical

values.

Table 3-1. Parameters Affecting Radiometer Antenna Temperature

Symbol	Parameter Definition	Typical Value
T	Temperature of the pixel	200K
δT	RMS temperature fluctuation of the earth	$\pm$ 50K
T_0	Cosmic background temperature	3K
η_p	Pixel beam efficiency	0.95
η_r	Residue beam efficiency	0.01
η_s	Spillover beam efficiency	0.05

The change of η_r is on the same order of magnitude as η_r itself when the antenna beam scans across the earth, because different portions of the side lobe region point toward the earth. Therefore, we assume $\delta\eta_r = \eta_r$, thus the term T $\delta\eta_r$ in (3-12) gives much higher contribution to the temperature variation than other terms. Therefore, the other terms in (3-12) can be ignored and the temperature resolution becomes

$$R = T\eta_r \qquad (3\text{-}13)$$

The physical meaning of (3-13) is that the pixel temperature, T, can be used as the representative temperature of the earth to estimate the contribution to the antenna temperature from the portion of the earth surface outside the pixel. Such contribution equals the minimum temperature difference resolvable by the antenna when it scans from one pixel to another. The term $\delta(T_0\eta_s)$ refers to the contribution from the background, and according to Table 3-1, is much smaller than T $\delta\eta_r$, because the cosmic background is much colder than the earth.

Using (3-13) as the sensitivity for the measurement of temperature difference between various pixels on the earth, the relative sensitivity of such measurements can be expressed as the ratio between the variation of the antenna temperature due to scan and the desired value of the antenna temperature ($T\eta_p$), that is

$$\epsilon = \frac{T\eta_r}{T\eta_p} \simeq \frac{\eta_r}{\eta_p} \qquad (3\text{-}14)$$

where ϵ is called *residue beam efficiency ratio.* The simplification of the temperature measurement sensitivity from (3-8) to (3-14) overcomes the difficulty of obtaining accurate values for η_p and η_r and relies only on the ratio of efficiencies, which can be evaluated by the normalized pattern function, $F(\theta, \phi)$, as follows

$$\epsilon = \frac{\eta_r}{\eta_p} = \frac{\frac{1}{4\pi}\int\int_{\Omega_e'} G(\theta, \phi)\, d\Omega}{\frac{1}{4\pi}\int\int_{\Omega_p} G(\theta, \phi)\, d\Omega} = \frac{\int\int_{\Omega_e'} F(\theta, \phi)\, d\Omega}{\int\int_{\Omega_p} F(\theta, \phi)\, d\Omega} \qquad (3\text{-}15)$$

The normalized pattern function can be evaluated accurately with PO in the region near main beam. Methods to extrapolate the integrated pattern function to calculate ϵ and to optimize the antenna temperature sensitivity using ϵ as the objective function are discussed in the following sections.

3.3 Calculation for Residue Beam Efficiency Ratio

The residue beam efficiency ratio of (3-14) is the relative temperature measurement error for earth observation antennas, and forms the primary performance evaluation parameter. To accomplish this, more approximation techniques are needed because the calculation for ϵ involves integration for $F(\theta, \phi)$ over solid angle Ω_e', which is much larger than the main beam for high gain antennas. For example, the requirement for Mission-to-the-Planet-Earth remote sensing antenna is approximately 800 pixels along the equator of the earth, which makes the cone angle of the earth approximately 800 times the antenna beamwidth. It is impossible in practice to PO evaluate a pattern up to such an angular extent.

In order to calculate ϵ, extrapolation for the integrated pattern function is required. The asymptotic approximation of pattern functions is used to perform this extrapolation. Our result shows that the integrated pattern function can be approximated by a linear function of $1/\sin\theta$ when θ is much greater than λ/D. The derivation and numerical results will be shown in the discussion that follows.

The pattern of antennas with a circular aperture (axisymmetric) can be expanded in terms of Bessel functions as [19]

$$G(\theta) = [\sum_{i=1}^{\infty} C_i J_i(z)/z]^2 \qquad (3\text{-}16)$$

where $z=2\pi (D/\lambda) \sin\theta$. When $z\rightarrow\infty$ (the same as $\theta \gg \lambda/D$),

$$J_i(z) \simeq \sqrt{\frac{2}{\pi z}} \left\{ \cos (z - \frac{1}{2} i\pi - \frac{\pi}{4}) \right\} \qquad (3\text{-}17)$$

therefore, (3-16) can be approximated by taking the most significant term as follows

$$G(\theta) \simeq [C_1 J_1(z)/z]^2 \simeq [C_1\sqrt{\frac{2}{\pi}} \cos(z - \frac{1}{2}\pi - \frac{\pi}{4})]^2 \cdot z^{-3} \qquad (3\text{-}18)$$

which shows that the level of side lobes decreases as z^{-3} when $z\rightarrow\infty$, but the period of side lobes, which is controlled by the factor $\cos(z - \frac{1}{2} i\pi - \frac{\pi}{4})$, remains unchanged. So integration of the pattern yields the following approximation

$$\eta(z\rightarrow\infty) = \frac{1}{4\pi} \int\int_{\Omega|_{z\rightarrow\infty}} G(\theta, \phi)\, d\Omega \simeq A/z + B \qquad (3\text{-}19)$$

where A and B are constants to be determined. We will discuss the method to determine A and B at the end of this section. Constant B is the asymptotic limit of the integrated pattern function, which can be used to determine the residue beam efficiency ratio. Since the earth has much greater angular extent than the pixel, the following approximation can be used

$$\eta(\Omega_e) \simeq \eta(\Omega|_{z\rightarrow\infty}) = B \qquad (3\text{-}20)$$

Thus, the residue beam efficiency can be calculated from B as follows:

$$\eta_r = \eta(\Omega_e - \Omega_p) = \eta(\Omega_e) - \eta(\Omega_p) = B - \eta_p \qquad (3\text{-}21)$$

This in (3-14) yields

$$\epsilon = \frac{B}{\eta_p} - 1 \qquad (3\text{-}22)$$

In practice, PO is first performed and (3-5) is used to evaluate the integrated pattern function in an angular region $\sim 20\lambda/D$ in extent. Then the portion of this integrated pattern function with large z values is least-squared fitted to $A/z + B$ to determine constants A and B, and the resultant B value is used in (3-22) to calculate the residue beam efficiency ratio.

Numerical verification for our method to calculate residue beam efficiency ratio is performed using a prime focus paraboloidal reflector system. The pattern of the example antenna is shown in Fig. 3-4, and is plotted as a function of $1/z$. The plot is very close to a straight line, which verifies that the integrated pattern function indeed approaches its asymptotic limit as $A/z + B$.

3.4. Optimization for Temperature Sensitivity

Residue beam efficiency ratio is the relative temperature resolution of a radiometer antenna, and, therefore, should be optimized within the design constraints such as the maximum physical aperture size and angular extent of the object to be observed. To simplify this optimization problem, we are concerned about only three parameters in the design process and assume a circular aperture and Gaussian aperture illumination. These parameters are: object angular extent (θ), aperture edge taper (C) and aperture diameter (D). Based on the three parameter assumption, the optimization problem becomes one dimensional, and can be expressed as follows:

$$\min \epsilon(C, \theta, D)$$

constraint: θ = object angular extent = constant

D = aperture diameter = constant (3-23)

To illustrate the relationship between aperture edge taper and residue beam efficiency ratio, we plot the integrated pattern functions and residue beam efficiency ratios with various taper values in Figures 3-5 and 3-6, respectively. The curves in Fig. 3-6 can be expressed as

$$\epsilon_i(\theta) = \epsilon(C_i, \theta, D)|_{D = \text{constant}} \quad \text{with i=1, 2, 3, 4} \qquad (3\text{-}24)$$

It can be shown from Fig. 3-6 that the value of taper for the smallest ϵ increases with the object angular extent. This is because when the object angular extent

is small, high gain is needed to concentrate the radiation onto the object, but when the object angular extent is large, high edge taper is needed to reduce the far-out side lobe level.

With a fixed aperture diameter, optimization can be performed to obtain the smallest ϵ and the corresponding taper for each value of object angular extent. First, the curves of residue beam efficiency ratio as functions of object angular extent were obtained for various taper values in the same fashion as (3-24), but with $i = 1$ to 240 as in the example of Fig. 3-7. Typically, values of C_i are chosen between 10 dB and 40 dB. Then, for each θ, the minimum ϵ among the values of 240 curves was obtained, which gives

$$i_{op}(\theta) = \underset{i}{\text{argmin}}[\epsilon_i(\theta)] \qquad (3\text{-}25)$$

In order to find an accurate minimum, a parabolic interpolation was performed among three pairs of $(C_i, \epsilon_i(\theta))$ with $i = i_{op-1}$, i_{op} and i_{op+1}, to find $C_{op}(\theta)$ and $\epsilon_{op}(\theta)$. The functions $C_{op}(\theta)$ and $\epsilon_{op}(\theta)$ resulting from this optimization process are plotted in Fig. 3-7.

The optimization above assumes a fixed aperture diameter. However, the result can be generalized to high gain reflector antennas with arbitrary D. This is accomplished by scaling the abscissa of Fig. 3-7 with factor D/λ, because for high gain antennas with different aperture diameter, the patterns scaled by D/λ are the same, and so does the integrated pattern function and residue beam efficiency ratio. The scaling with D/λ generalizes the curves in Fig. 3-7 to all circular aperture antennas.

Fig. 3-7 can be used as a design tool for radiometer antennas. There are two situations in designing a radiometer antenna:

(1) Knowing θ and D, find the optimal C to minimize ϵ

(2) Knowing θ and the tolerance for ϵ, find the optimal C to minimize D

In the first situation, $D/\lambda \sin\theta$ can be calculated and used as the abscissa, then the smallest ϵ and the corresponding optimum edge taper can be found directly from the two curves of Fig. 3-7. In the second situation, the abscissa can be determined using the curve for optimum ϵ and the given value for ϵ. Then D is calculated with this abscissa and the given value for θ; meanwhile the optimum

taper value is read from the curve for optimum taper and the value of this abscissa. The design accomplished in the second situation offers the smallest aperture size with the desired temperature error tolerance.

To conclude this chapter, we point out that residue beam efficiency ratio is the most important parameter in the evaluation for earth observation radiometer antennas. It directly relates the antenna pattern to the relative temperature measurement error, and can be calculated with higher accuracy than beam efficiency. Therefore, in a design process, it should be the primary parameter.

Chapter 4
PRINCIPLES OF SPHERICAL MAIN REFLECTOR ANTENNAS

4.1. Introduction to Spherical Main Reflector Antennas

In many applications it is often required to scan the main beam of an antenna without rotating the whole antenna structure. For satellite communication ground stations, tracking several satellites with the same antenna can be much more cost-effective than building one antenna for each satellite. This requires the antenna to produce several simultaneous main beams, which is referred to as a multibeam application. Multibeam antennas are also desirable for space-borne satellites. In remote sensing such as earth observation from geostationary orbit, it is required to scan the antenna main beam through the whole observed region. However, mechanically slewing an entire large antenna structure to scan the main beam is usually prohibited in such applications because of mechanical difficulties, reliability, and vibrations induced on the platform.

Traditionally, scanning the main beam without rotating the main reflector is achieved by displacing the feed in the focal plane of a paraboloidal main reflector. This scanning approach can cause significant GO aberration and pattern degradation [2]. Improvements on this scheme include the use of a phased array feed in the focal field to correct for the GO aberration [2]. The disadvantage of a phased array feed is the electrical complexity introduced by the phasing network and the noise increase due to multiple feeds and the phasing network.

On the contrary, spherical main reflector antennas can scan at relatively low cost with constant performance during scan, if proper suboptics systems are used to correct for the spherical aberration. The geometry of the scanning scheme of a spherical main reflector is illustrated in Fig. 4-1. For simplicity of illustration, a single feed is used to illuminate a portion of the spherical reflector. Scan is accomplished by rotating the feed about the center of the sphere, which moves the illumination to a different portion of the main reflector and, since the main reflector is spherical, this feed rotation is equivalent to rotating the whole antenna system, including the main reflector and the feed; therefore, electrical

performance is unchanged during scan.

4.2. Phase Error in Prime Focus Spherical Reflector Systems

The configuration shown in Fig. 4-1 is called a prime focus spherical reflector system because only a single feed is used and is located at the approximate focal point of the spherical reflector. Due to spherical aberration, the focal point is not a well defined point; but instead, power is distributed in a caustic region around the point. The aberration depends mostly on the F/D′ ratio of the spherical reflector, where D′ is the diameter of the illuminated portion of the reflector and F is the focal length.

As discussed in Chapter 2, aberration can be measured by the path length error from the feed to the aperture plane. Since a prime focus paraboloidal reflector has zero path length error, the paraboloid can be used as the reference to calculate the path length error of a spherical reflector with the same focal length. For simplicity we present results in two dimensions with no loss in generality because of the rotational symmetry. The shape of an axisymmetric paraboloid with a generator parabola given by

$$z = \frac{x^2}{4F} - F \tag{4-1}$$

where F is the focal length and the focal point is located at x=0 and z=0. The spherical reflector is represented by

$$(z-F)^2+x^2=(2F)^2 \tag{4-2}$$

where the focal point is located at x=0 and z=0. Expanding (4-2) in a Taylor series yields

$$z \simeq -F + \frac{x^2}{4F} + \frac{x^4}{64F^3} \tag{4-3}$$

The difference in shape between the sphere in (4-3) and the paraboloid in (4-2) is $x^4/(64F^3)$. The path length of a ray emerging from the feed and being reflected by the spherical reflector is $2x^4/(64F^3)$ shorter than the same ray reflected by the paraboloid, including both the path length difference before and after reflection. Thus, the path length error for a spherical reflector is

$$\Delta L(x) \simeq x^4/(32F^3) \qquad (4\text{-}4)$$

The maximum path length error occurs on the edge of the spherical reflector where x=D′/2. Therefore, the maximum path length error is

$$\Delta L \simeq D'^4/(2^9F^3) \qquad (4\text{-}5)$$

which shows that the aberration measured by path length error grows rapidly as D′ increases; we call this the D'^4 rule. Equation (4-5) can be used to calculate an upper bound on D′ or lower bound on F/D′ during the design of spherical reflector antennas.

In a design situation it is convenient to specify the maximum phase error in the aperture and then calculate the maximum D′ or minimum F using (4-5). The maximum phase error from (4-5) is

$$\Delta\phi \simeq \frac{2\pi}{\lambda} D'^4/(2^9 F^3) \qquad (4\text{-}6)$$

Typically, $\Delta\phi$ is required to be less than $2\pi/32$, then the following design criteria must be satisfied:

$$\frac{D'^4}{F^3} \leq 2^4 \lambda \qquad (4\text{-}7)$$

For example, in earth remote sensing systems requiring a 25-m diameter aperture and operating at 30 GHz ($\lambda = 0.01$ m), the minimum focal length is 134.7 m according to (4-7), which is impractical to achieve in space applications. Moreover, the large F/D′ value will cause unacceptably low aperture efficiency as discussed in the Section 4.3. Therefore, prime-focus spherical reflectors are rarely used in high gain reflector antenna designs. However, they can be used in low gain systems for low cost.

4.3. Aperture Efficiency Analysis for Spherical Main Reflector Systems

In addition to spherical aberration, spherical reflectors also suffer from poor aperture efficiency. Poor aperture efficiency is primarily caused by the motion of the illuminated area on the spherical main reflector during scan. In the prime focus spherical reflector antenna shown in Fig. 4-1, the center of the illuminated portion is located at x=R sin θ, where R is the radius of the sphere and θ is the scan angle. The illuminated portion on the spherical reflector moves

during scan; therefore, oversizing the main reflector is necessary in order to keep the illuminated portion within the reflector, which reduces the aperture efficiency.

The evaluation of aperture efficiency in spherical main reflector systems is straight forward. Suppose that the angular extent of the illuminated portion of the main reflector as seen from the spherical center is ξ, and the angular scan range is $\Delta\theta$, then the angular extent of the whole spherical reflector must be $\xi+\Delta\theta$ in order to avoid spillover. The ratio between the illuminated area and the area of the whole main reflector is called aperture utilization, ϵ_u. Since the reflector is spherical, ϵ_u can be calculated as follows

$$\epsilon_u = \frac{A_i}{A_p} = \frac{R^2\,\Omega_i}{R^2\,\Omega_p} \simeq \left(\frac{\xi}{\xi+\Delta\theta}\right)^2 \qquad (4\text{-}8)$$

where A_i and A_p are the areas of the illuminated portion and physical reflector, respectively; Ω_i and Ω_p are the corresponding solid angles as seen from the spherical center. Aperture efficiency is further reduced by the taper of the illumination within the illuminated portion. According to Table 2-1, the overall aperture efficiency will be

$$\epsilon_{ap} = \epsilon_u\, G/\,[\,\frac{4\pi}{\lambda^2}\, A_i] \qquad (4\text{-}9)$$

Since ϵ_u is related to the oversizing of spherical reflectors, we confine our attention to ϵ_u in this chapter.

The angular extent of the illuminated portion, ξ, is related to F/D′ of the antenna as follows:

$$F/D' = R/(2D') = \frac{1}{4\,\sin(\xi/2)} \qquad (4\text{-}10)$$

In normal design situations with $F/D' \geq 1$, (4-10) can be approximated by

$$\xi \simeq \frac{1}{2}\,(F/D')^{-1} \qquad (4\text{-}11)$$

This, in (4-8), yields

$$\epsilon_u \simeq [1 + 2\,\Delta\theta\cdot(F/D')]^{-2} \qquad (4\text{-}12)$$

which reveals that increasing F/D′ reduces the aperture utilization. This is in conflict with the phase error requirement of (4-7), which requires a large F/D′ for

low phase error. For example, the 25-m diameter class earth observation antenna requires F/D′=5.4 according to (4-7), and the angular scan region has $\Delta\theta$=10° for $\pm 5°$ of scan; therefore, the aperture utilization is only 12% according to (4-12), which is unacceptable.

In designing a practical reflector antenna, the phase error must be below tolerance and the aperture efficiency is usually above 40%. In order to implement a spherical reflector that meets these goals, the F/D′ must be reduced to improve the aperture utilization while maintaining the phase error within the tolerance. This requires correction for spherical aberration.

4.4. Methods to Correct for Spherical Aberration

Methods to correct for spherical aberration can greatly reduce the F/D′ value of high gain spherical main reflector systems while maintaining the phase error below tolerance, and therefore, improve the aperture efficiency. Of course, these methods also reduce the aperture phase error and offer significant improvement in antenna pattern. In reflector antenna design the aperture amplitude distribution is also important. So methods to correct for the spherical aberration must take into consideration both phase error and feed-to-aperture amplitude mapping.

The first method to correct for the spherical aberration was proposed by Holt [8] in 1964. His method employed a subreflector in a Gregorian configuration to correct for the path-length error from the feed to the aperture. As mentioned in Chapter 2, for n-reflector systems, once the shapes of $n-1$ reflectors are known, the remaining reflector shape can be solved by equal path length law. In Holt's system there are only two reflectors with the main reflector being spherical; therefore, the subreflector can be solved by the equal-path-length law. There are two parameters to determine the shape of such a subreflector, one is the feed location and the other is the vertex location of the subreflector along the axis of the main reflector.

By employing the Gregorian subreflector the aperture phase error can be reduced to zero in theory. However, the feed-to-aperture mapping is not taken into consideration. Consequently, this dual-reflector system does not control the

aperture amplitude distribution. Indeed, the aperture amplitude distribution has an inverted taper, i.e. higher illumination on the edge of the aperture than at the middle of the aperture. The inverted aperture taper leads to significant side lobe level which makes the dual-reflector system unsuitable for remote sensing applications.

More degrees of freedom are needed to include the feed-to-aperture mapping in the subreflector shape synthesis; this requires another subreflector. By enforcing the equal-path-length law, the shape of one subreflector can be solved; by restricting the feed-to-aperture amplitude mapping, the shape of the second subreflector can be determined. Kildal [12] and Watanabe et al. [13] performed a synthesis on spherical main reflector systems with dual subreflectors. Similar concepts were developed by Galindo-Israel et. al. for dual-shaped reflector systems with high aperture efficiency. Our generalization of Galindo-Israel's concept led to the new approach for spherical tri-reflector systems discussed in Chapter 5.

There are two approaches to synthesize dual subreflector systems: a partial differential equation approach and an optimization approach. Kildal et al. reported on both the analysis [11] and the synthesis [12] of the proposed Arecibo Observatory antenna system which consists of two subreflectors. Kildal's synthesis approach includes an approximate numerical solution for a set of partial differential equations derived from kinematic and dynamic ray tracing [12].

Watanabe et al. [13] developed a synthesis method for a spherical tri-reflector system and verified the technique by building a multibeam earth station antenna. Their method represents the subreflector surface shapes by functional expansions. Each basis function in the expansion series satisfies the equal-path-length condition. The coefficients in the series expansion were optimized to achieve the desired aperture distribution. Both the approaches of Kildal et al. and Watanabe et al. solve the problems of high side lobes and high cross polarization.

All these traditional spherical main reflector system design approaches have an aperture utilization factor ϵ_u that is less than unity, which leads to low

aperture efficiency ϵ_{ap}. This problem is solved by the new approach discussed in Chapter 6. Also, spherical tri-reflector systems require motion of the whole suboptics assembly that consists of a feed and two subreflectors; the motion is simplified by the method proposed in Chapter 6.

Chapter 5
THE PROPOSED SPHERICAL TRI-REFLECTOR ANTENNA

In the previous chapter traditional spherical main reflector systems are discussed. They all have poor aperture efficiency because the illuminated portion of the spherical main reflector moves during scan. In this chapter a new spherical tri-reflector system design approach is introduced. It avoids the poor aperture efficiency problem by fixing the illuminated portion on the main reflector during scan. Therefore, it can achieve the same aperture efficiency as a prime focus paraboloid, and moreover, it provides the same wide angle scan with constant electrical performance as for traditional spherical tri-reflector systems.

5.1. Overview of the Proposed New Approach

The new approach uses a spherical tri-reflector configuration that scans without gain loss and has perfect aperture utilization (i.e. $\epsilon_u \simeq 1$), while providing an aperture illumination that is controlled by the feed pattern. The configuration consists of an offset spherical main reflector, a subreflector, and a tertiary reflector as shown in Fig. 5-3. The key to our approach is the synthesis of axially symmetric suboptics reflector shapes that perform both a mapping of an isotropic feed pattern to a uniform aperture plane distribution and the correction for spherical aberration. This synthesis procedure is an extension of Galindo-Israel's method of solving partial differential equations exactly to obtain reflector surface shapes for dual reflector systems [14].

The mapping between an isotropic feed and a uniform aperture offers the following two major advantages.

1) Scan can be accomplished by rotating the suboptics assembly (including the feed, the tertiary and the subreflector) along the R/2 spherical surface about the center of the main spherical reflector, while tilting the feed relative to the suboptics assembly to maintain illumination over the same part of the main reflector. (See Fig 5-3 and further explanation in Section 5.2.) This unique feature of a constant illumination of the entire main reflector eliminates the need for an oversized main reflector which is common among scanning spherical

reflector systems. The tilting feed method is possible only with the isotropic-to-uniform mapping, as will be explained.

2) The aperture distribution is controlled by the feed pattern. The first step in the design process is to use an isotropic feed to synthesize the subreflector shapes. Then the isotropic feed is replaced by a real feed with the desired radiation pattern. Still, a perfect one-to-one correspondence exists between the feed pattern and the aperture distribution. For example, if the feed has a Gaussian pattern, the aperture distribution will be Gaussian as well. This leads to very low side lobe and cross polarization levels.

Analysis of the new configuration has shown excellent performance during scan; see Chapter 7. The details of this new method are discussed in the following two sections which begin with the synthesis of an axially symmetric system followed by an offset system based on an axially symmetric parent system.

5.2. Synthesis for the Axially Symmetric Spherical Reflector System

The new design approach is best understood by examining its evolution from an axially symmetric spherical tri-reflector system, which has correction for spherical aberration and an exact power mapping from an isotropic feed pattern to a uniform aperture amplitude distribution. This axially symmetric configuration is the *parent configuration* for the new design to be developed in the next section. The shapes of the subreflector and the tertiary are derived from an ordinary differential equation. This is a generalization of Galindo-Israel's two-dimensional partial differential method [14].

Geometry for the Synthesis Problem

A profile view of the geometry used in the new synthesis method is shown in Fig. 5-1. *Parent reflectors*, from which the final reflectors are derived, are generated by rotating the profile in Fig. 5-1 360° about the z' axis. (Primed coordinates are introduced here and will be fixed relative to reflector optics that

move to achieve beam scanning.) This forms an axisymmetric system that can be synthesized in two dimensions (2D), which is a significant simplification of the problem.

We now explain the behavior of the system of Fig. 5-1 using geometrical optics (GO) principles. The ray $P'_fP'_3P'_2P'_1P'_0$ originating from the feed located at P'_f $(0, z'_f)$ is reflected at P'_3 (x'_3, z'_3) on the tertiary, P'_2 (x'_2, z'_2) on the subreflector, and P'_1 (x'_1, z'_1) on the main reflector; finally, it leaves P'_3 parallel to the z' axis striking the aperture at P'_0 $(x'_1, 0)$. The *feed angle*, θ', is the angle of the ray $P'_fP'_3$ (the *feed ray*) off the feed axis ($-z'$ axis). The length of $P'_fP'_3$ is r'. Therefore, P'_3 can be described in polar coordinates (θ', r'), which are related to the corresponding rectangular coordinates (x'_3, z'_3) as follows:

$$\begin{aligned} x'_3 &= r' \sin \theta' \\ z'_3 &= -r' \cos \theta' + z'_0 \end{aligned} \tag{5-1}$$

The ray reflection points on the main reflector and the subreflector, P'_1 (x'_1, z'_1) and P'_2 (x'_2, z'_2), respectively, are uniquely related to the feed ray $P'_fP'_3$ by ray tracing. In other words, (x'_1, z'_1) and (x'_2, z'_2) are functions of (θ', r'). Moreover, r' is a function of θ' (written as $r'(\theta')$) through the tertiary shape function. The function $r'(\theta')$ can be solved by numerical methods for ordinary differential equations (ODE) if $\frac{dr'}{d\theta'}$ can be calculated at each point (θ', r'). Thus, after solution of the ODE all surface shapes are known as sets of points $P'_2(x'_2, z'_2)$ and $P'_3(x'_3, z'_3)$ as functions of the angle θ'.

Three Steps to Establish the ODE

There are three steps in the derivation of the ODE required to perform the synthesis of the suboptics shapes. These steps are detailed below. They enforce the conditions of parallel rays exiting the main spherical reflector, of satisfaction of Snell's law of reflection on all reflectors, and of a mapping of an isotropic feed pattern into a uniform aperture distribution.

Step 1: Determining the feed-to-aperture mapping

The first step is to determine the feed-to-aperture mapping by evaluating the aperture point P'_0 $(x'_1, 0)$ for each θ'. The mapping between the feed

pattern and the aperture power distribution leads to a functional relationship between θ' and x'_1, which can be uniquely solved in 2D (it is then immediately applicable to 3D axially symmetric systems) [14]. (In 3D non-axisymmetric systems, an exact mapping from a given feed pattern to the desired aperture power distribution exists [14], but there is no unique functional relationship between each feed output ray direction and its aperture output location [12, 13, 14].) The function $x'_1(\theta')$ is obtained by solving the following power conservation relation between a feed ray cone and its corresponding aperture ray tube for the 3D axisymmetric system [6; Section 8.6]:

$$S_{ap}(x'_1)\, x'_1\, dx'_1\, d\phi' = U_f(\theta')\, \sin\theta'\, d\theta'\, d\phi' \tag{5-2}$$

where S_{ap} is the aperture power intensity distribution in W/m^2 and U_f is the feed radiation intensity in W/steradian. Canceling $d\phi'$ from both sides of (5-2) gives the following result:

$$S_{ap}\, x'_1\, dx'_1 = U_f \sin\theta'\, d\theta' \tag{5-3}$$

The case of an isotropic feed pattern and a uniform aperture distribution results in taking S_{ap} and U_f to be constants in (5-3); then S_{ap} and U_f are related to each other through the total power conservation as follows:

$$\int_0^{\pm D/2} S_{ap}\, x'_1\, dx'_1 = \int_0^{\theta'_m} U_f \sin\theta'\, d\theta' \tag{5-4}$$

where D is the diameter of the axially symmetric parent main reflector. The + and − signs on D/2 in the limits of integration correspond to the *single-caustic* and *dual-caustic* configurations, respectively, which are discussed at the end of this section. The ray corresponding to the feed angle θ'_m determines the edge of each of the three parent reflectors as shown in Fig. 5-1; θ'_m sets the *synthesis limit* for the feed angle. The feed pattern is isotropic interior to θ'_m and is zero for feed angles θ' larger than θ'_m; i.e. the feed has a sectoral pattern. Equation (5-4) determines U_f/S_{ap}. For convenience we define a *mapping normalization factor* $q=\frac{1}{2}(U_f/S_{ap})R^{-2}$, where R is the radius of curvature of the main reflector. Then (5-3) can be rewritten as

$$x'_1\, dx'_1 = q\, R^2 \sin\theta'\, d\theta' \tag{5-5}$$

Integrating both sides yields

$$x'^2_1 = C - R^2\, q \cos\theta' \tag{5-6}$$

The constant of integration, C, is determined by evaluating (5-6) for the vertex ray; this ray leaves the feed along the $-z'$ axis ($\theta'=0$) and arrives in the aperture along the z' axis ($x'_1=0$). Using $x'_1=0$ and $\theta'=0$ in (5-6) gives $C= q R^2$. This in (5-6) gives

$$x'_1 = \pm R \sqrt{q\,(1-\cos\theta')} \tag{5-7}$$

The + (−) sign correspond to the *dual-caustic* (*single-caustic*) solutions discussed at the end of this section. Note that evaluation of (5-7) for the edge ray ($\theta'=\theta'_m$ and $x'_1=\pm D/2$) gives $D/2=R\sqrt{q\,(1-\cos\theta'_m)}$, which satisfies the total power conservation relation of (5-4); this relation shows how the parent main reflector diameter D depends on q.

Since the main reflector is of spherical shape, once x'_1 is determined z'_1 is readily obtained by the spherical surface relationship between x'_1 and z'_1 as follows:

$$z'_1 = -\sqrt{R^2 - x'^2_1} \tag{5-8}$$

To summarize, the first step establishes the functional relationship, (5-7), between the aperture point P'_0 and the feed angle θ' which satisfies the isotropic-to-uniform mapping. The ray exiting the feed at angle θ' eventually strikes the aperture at the point $P'_0\,(x'_1, 0)$, where x'_1 is found from θ' by (5-7). Once the aperture point P'_0 is found, the main reflector ray reflection point is found to be $P'_1\,(x'_1, z'_1)$, where z'_1 is found from x'_1 using (5-8).

Step 2: Correcting for Spherical Aberration

The second step is to correct for spherical aberration. This is accomplished by shaping the subreflector, i.e. by evaluating $P'_2\,(x'_2, z'_2)$ based on the given $P'_1\,(x'_1, z'_1)$ and $P'_3\,(x'_3, z'_3)$. The spherical surface normal at P'_1 is first obtained. Knowing that the main reflector aperture output ray must be parallel to the z'-axis and applying Snell's law determines the ray that goes through P'_2 and P'_1. The ray $P'_2P'_1$ gives the following linear relationship between x'_2 and z'_2 (see Appendix 5A for details):

$$x'_2 = \left[\, 1 + \frac{2\,z'_1}{2\,z'^2_1 - R^2}\,(z'_2 - z'_1)\,\right] x'_1 \tag{5-9}$$

This relation is based on the fact that the point P'_2 (x'_2, z'_2) lies along the ray $P'_2P'_1$. The location of the subreflector ray reflection point P'_2 along this ray path is determined by the constant total path length condition for the ray $P'_0P'_1P'_2P'_3P'_f$:

$$L = -z'_1+\sqrt{(z'_1-z'_2)^2+(x'_1-x'_2)^2}+\sqrt{(z'_2-z'_3)^2+(x'_2-x'_3)^2}+\sqrt{(z'_3-z'_f)^2+x'^2_3} \tag{5-10}$$

where the total path length L is a design parameter. This constant path length condition guarantees the correction of spherical aberration. Substituting (5-9) into (5-10) gives a single equation in terms of z'_2 that can be solved explicitly in terms of the given values for P'_0, P'_1, P'_3 and L. At this point one can calculate the reflection points (x'_1, z'_1), (x'_2, z'_2) and (x'_3, z'_3) for an arbitrary ray that hits the tertiary at (assumed) point (r', θ') which is equivalent to (x'_3, z'_3) from (5-7) and (5-8) which yield (x'_1, z'_1), then (5-9) and (5-10) yield (x'_2, z'_2).

Step 3: Forming the ODE at the Tertiary

The third step establishes the required ODE based on the information from the previous steps which, in turn, is used to calculate the surface derivative on the tertiary reflector. The surface derivative is essentially equivalent to the surface normal which can be found from Snell's law. Snell's law requires that the surface normal at point P'_3 on the tertiary bisects the angle between the feed-to-tertiary ray $P'_fP'_3$ and the tertiary-to-subreflector ray $P'_3P'_2$. The feed-to-tertiary ray is determined by the end points P'_f $(0, z'_f)$ and P'_3 (x'_3, z'_3). The tertiary-to-subreflector ray is determined by the end points P'_3 (x'_3, z'_3) and P'_2 (x'_2, z'_2). Minimization of the ray path length $P'_fP'_3P'_2$ will satisfy Snell's law and, as shown in Appendix 5B, yields the following surface derivative relation:

$$\frac{dr'}{d\theta'} = \frac{-r'\,[(z'_3-z'_2)\sin\theta'+(x'_3-x'_2)\cos\theta']}{\sqrt{(z'_3-z'_2)^2+(x'_3-x'_2)^2}+[-(z'_3-z'_2)\cos\theta'+(x'_3-x'_2)\sin\theta']} \tag{5-11}$$

Reflector Shape Synthesis: Solving the ODE

Note that (5-11) is an ODE because the dependent variable in the

derivative, r′, also appears in the right hand side (RHS), and the RHS can be evaluated using steps 1 and 2 once (r′, θ') are known. Synthesis is performed by numerically solving the ODE (5-11) subject to a set of initial given conditions (initial value ODE problem).

The initial values are those associated with the vertex ray. That is, the initial values are the coordinates of the vertex of each reflector. The radius R of the main reflector is chosen so that the main reflector vertex is at (x'_1=0, z'_1=−R). The subreflector vertex is located at (x'_2=0, z'_2=z'_{20}); the tertiary vertex is at (x'_3=0, z'_3=z'_{30}); the feed is at (0, z'_f). In addition to these initial values, q in (5-7) is an assumed value that is usually taken to be unity. The synthesis limit θ'_m is another design parameter which when combined with q value will determine the main reflector aperture diameter. Although the total path length L in (5-10) is also a design parameter, it depends on the other initial given values. L is constant for all rays and is equal to that for the vertex ray from (0, z'_f) to (0, z'_{30}) to (0, z'_{20}) to (0, −R) to O which is given by

$$L = |z'_{30} - z'_f| + |z'_{20} - z'_{30}| + |-R - z'_{20}| + R \qquad (5\text{-}12)$$

which relates L to the initial conditions. From this vertex ray with θ'=0 and $r' = |z'_{30} - z'_f|$, the 8th-order Runge-Kutta method is used to solve the ODE. The Runge-Kutta method is analogous to the following procedure: for each iteration, θ' is incremented by $\Delta\theta'$ and $\frac{dr'}{d\theta'}$ is calculated from the three steps discussed above; then r′ is incremented to the next value as $r' + \frac{dr'}{d\theta'}\Delta\theta'$. The Runge-Kutta iteration is performed up to the maximum feed angle when $\theta' = \theta'_m$.

The choice of the sign in (5-7) yields different solutions. The two basic configurations corresponding to + and − are the *dual-caustic* and *single-caustic* systems, respectively. The *dual-caustic* system shown in Fig. 5-1 has caustics between the tertiary and the subreflector, and between the subreflector and the main reflector. The *single-caustic* system shown in Fig 5-2 has only one caustic between the subreflector and the main reflector. In the dual-caustic system, the tertiary blocks the parent main reflector aperture. Also, the performance of the dual-caustic configuration is limited at lower frequencies because of the extra caustic due to the cusp diffraction [11]. This is not a problem with the single-caustic design and, therefore, it is usually the preferred configuration. However, in the single-caustic system the feed must be located along the z′ axis between

the spherical reflector focal point and the subreflector to avoid blockage; see Fig. 5-2. In the dual-caustic system the feed can be placed anywhere along the z' axis facing the tertiary. Thus, the dual-caustic system is worth consideration when feed location control is important.

5.3. Design of a New Offset Spherical Main Reflector System

The synthesis procedure described in Section 5.2 gives the shapes of the parent axially symmetric reflectors. A multistage evolution is then performed to determine the reflector perimeters in the *final system* (which can be constructed). In this section the scan principles are discussed first, followed by an explanation of the perimeter determination process. Finally, comments on system design are presented.

The configuration shown in Fig. 5-3 is used in this section to illustrate main beam scanning. The axially symmetric configuration derived from the synthesis procedure of Section 5.2 for the single caustic system of Fig. 5-2 provides a family of parent reflector shapes. Of course, the axisymmetric parent reflector configuration is not practical because of the total blockage. The offset *intermediate reflector system* with rectangular perimeters is formed from the axially symmetric parent system to avoid the blockage. During scan the intermediate reflector system together with the z' axis shown in Fig. 5-3 are treated as a *rigid system*; that is, all three reflectors, the feed and the z' axis moves as a unit.

In the synthesis process of Section 5.2 a sectoral feed pattern with cone angle θ'_m was used to achieve uniform illumination on the parent main reflector. The feed for the intermediate reflector system (*intermediate feed*) is similar but has a sectoral pattern with a narrower cone angle. The intermediate feed has cone angle θ_m with $\theta_m < \theta'_m$. The choice of θ_m is discussed in the comments on system design at the end of this section. In the design for the final reflector system, the intermediate feed serves to specify the spillover limit; i.e. for the real feed (e.g. a Gaussian feed) used in the final system, the spillover is the portion of its pattern that is beyond the beam cone of the intermediate feed.

Scan Principles

Scan is described in a spherical coordinate system (*scan coordinate system*) with a fixed z axis passing through the center of the illuminated portion of the main reflector, V, and the main reflector center of curvature, O, as shown in Fig. 5-3. The z' axis points in the direction (θ, ϕ) which is parallel to the output beam direction. Angle θ is between the z' and the z axes, and angle ϕ measures the rotation of the z' axis about the z axis; see Fig. 5-3e.

θ scan is best visualized as a two step process. First, the entire intermediate system (including the z' axis, the intermediate main reflector and suboptics assembly) is rotated about the spherical center O by angle θ. Of course, this rotation steers the main beam which is parallel to the z' axis. Although the intermediate main reflector rotates with the intermediate system, the final main reflector can be fixed because it is spherical. If no other changes were made, the final main reflector would have to be oversized to accommodate the changing illuminated region. In order to avoid oversizing the main reflector, we use the tilting feed method described in the next step to fix the main reflector illumination center in space.

In the second step, the feed is tilted relative to the z' axis within the intermediate system in order to keep the main reflector illumination center V fixed in the scan coordinates, see Fig. 5-3 b and d. In the first step (without the feed tilt), the illumination center moves with the intermediate main reflector. In the second step, the feed tilt moves the illumination center V relative to the intermediate main reflector. The relative motion between V and the intermediate main reflector cancels the movement caused by the motion of the intermediate main reflector so that V is stationary in the scan coordinate. Note that this step is possible because of the isotropic-to-uniform mapping; i.e. the feed pattern can be scanned with no resulting change in aperture taper.

We now determine the amount of the feed tilt angle required to fix the main reflector illumination center V. The angle of feed tilt θ'_f is the angle between the feed axis and the $-z'$ axis. The ray emanating from the feed along its axis is called the principal ray. The principal ray is reflected by the tertiary and the subreflector striking the main reflector at V, which is x'_V away from the z' axis as shown in Fig. 5-3f; and x'_V is related to the scan direction θ by

$$x'_V = R \sin\theta \tag{5-13}$$

The mapping function (5-7) evaluated under the condition $x'_1 = v'_V$, $\theta' = \theta'_f$ gives

$$(x'_V)^2 = [\, R \sqrt{q\,(1-\cos\theta'_f)}\,]^2 \tag{5-14}$$

Substituting (5-13) into (5-14) gives θ'_f in terms of the scan angle θ as follows:

$$\theta'_f = \arccos(\, 1 - \tfrac{1}{q} \sin^2\theta\,) \tag{5-15}$$

The intermediate configuration is shown for different θ-scan angles in Fig. 5-3 a and c. The ϕ scan is accomplished by rotating the intermediate system about the z axis. This rotation steers the z′ axis and the output beam direction in a conical fashion. Fig. 5-3 c and d illustrate cases with $\phi=0$ and $\phi>0$ beam directions, respectively. Since the z axis passes through the main reflector illumination center V, V does not move during ϕ scan. This permits the illuminated portion of the spherical main reflector to remain fixed during ϕ scan.

Determination of Reflector Perimeters – The Final Configuration

The parent reflectors derived from the synthesis process in Section 5.2 were visualized as having rectangular perimeters. The final subreflector and tertiary reflector are derived from the intermediate subreflector and intermediate tertiary reflector by trimming the edges to reduce their sizes. The final main reflector is derived according to the requirement that it has to cover the illuminated potion of the main sphere at all scan angles. In this section, methods to obtain the edge perimeter for each of the final reflectors are discussed.

The intermediate feed (sectoral feed with beam cone angle θ_m) is used for perimeter determination. The illuminated portions of the intermediate subreflector and tertiary change during θ scan due to the feed tilt. For each scan angle θ the axis of the intermediate feed is tilted relative to the z′ axis according to (5-15). The illumination edge contours on the intermediate tertiary and subreflector are obtained by tracing the cone of edge rays from the intermediate feed. The perimeters of the final subreflector and tertiary reflector are obtained by sampling these illumination edge contours at several different θ angles over the desired θ-scan range; the resulting illumination edge contours, which do not coincide, are used to select a final reflector perimeter which just accommodates those contours.

The entire suboptics assembly in the final system is rotated about the z axis during ϕ scan as shown in Fig. 5-3e, with no relative motion within the suboptics assembly (including the feed). Therefore, the final subreflector and the tertiary need not be oversized to accommodate ϕ scan, and their perimeters can be determined from θ scan alone. This feature reduces the subreflector and tertiary reflector sizes of the final design, because both reflectors are elongated only in one dimension.

The determination for the perimeter of the final main reflector is different from that for the final subreflector and tertiary reflector because the final main reflector does not move during scan while the intermediate main reflector does. The final main reflector can remain stationary because of the spherical symmetry; rotating the main reflector alone about the center O does not have any effect on the performance of the antenna system.

The final main reflector must have a perimeter such that the edge rays strike it at all scan angles. Although the center of the main reflector illumination does not change, the illumination distribution changes slightly during the scan. This is because the mapping in (5-7) is nonlinear, which leads to an elliptical aperture edge ray contour from a feed with a circularly symmetric edge ray cone. Since a sectoral feed is used, we define the *aperture ellipse* as the aperture illumination edge contour caused by the edge ray cone of the sectoral feed. The ratio between the two axes of the aperture ellipse is controlled by the mapping normalization factor, q.

The two axes of the aperture ellipse are along the $\hat{\theta}$ and the $\hat{\phi}$ directions associated with the θ and ϕ angles in the scan coordinate system shown in Fig. 5-3e. A prudent choice for q is one that makes the minor axis of the aperture ellipse along $\hat{\theta}$. As the θ-scan angle increases the minor axis along $\hat{\theta}$ decreases as seen in (5-7). When this aperture ellipse is projected onto the main reflector surface, an ellipse on the main reflector surface (the *surface ellipse*) is created. The surface ellipse specifies the main reflector surface illuminated area. The minor axis of the aperture ellipse along $\hat{\theta}$ has to be multiplied by sec θ to obtain the length of one axis of the surface ellipse. The sec θ factor arises from the aperture-to-surface projection. The other axis of the surface ellipse has the same

length as the major axis of the aperture ellipse along $\hat{\phi}$. Since the minor axis is expanded by the sec θ factor, the surface ellipse is closer to a circle than the aperture ellipse.

The fact that the surface ellipse is very close to circular is demonstrated by our test cases discussed in Chapter 7. For example, in our single-caustic test case with 10° θ scan the surface ellipse has two axes of 9.9 m and 9.8 m. A circular main reflector illumination is important to ϕ scan, because the illumination rotates relative to the fixed final main reflector during ϕ scan. In general, oversizing the final main reflector is necessary to accommodate the illumination rotation. However, the design which yields an approximately circular surface illumination makes the oversizing unnecessary.

Although oversizing the final main reflector can be made unnecessary during ϕ scan, the size of the illuminated area on the main reflector will change when θ scan is performed. This is because we chose an isotropic feed to uniform aperture mapping rather than to uniform main reflector surface power distribution mapping. For the same sectoral feed the area A of the aperture ellipse remains constant independent of the θ-scan angle. When the aperture ellipse area A is projected onto the main reflector surface, the area of the surface ellipse is A sec θ , which increases with θ. So the surface area of the final main reflector has to be determined according to the maximum θ-scan angle. By doing so, the main reflector is fully illuminated at the maximum θ-scan angle, and partially illuminated at smaller θ-scan angles. This is an automatic gain control process which guarantees constant gain throughout the scan region.

Final Comment on the Design Technique

The cone angle θ_{m} for the intermediate feed determines the final reflector perimeters. The illuminated area moves across the intermediate reflectors during θ scan; this requires extra area on each intermediate reflector. Smaller θ_{m} will result in smaller illuminated areas on the intermediate reflectors, which leads to smaller final reflector sizes and larger F/D, but a greater θ-scan range. Therefore, the choice of θ_{m} involves a tradeoff. We use the following formula to

estimate θ_m:

$$2\,\theta_m = \theta'_m - \theta'_{fm} \tag{5-16}$$

where θ'_m is the synthesis limit used in Section 4 and θ'_{fm} is the feed tilt angle at the maximum θ-scan angle. θ'_{fm} follows from (5-15) as

$$\theta'_{fm} = \arccos(1 - \frac{1}{q}\sin^2\theta_{max}) \tag{5-17}$$

where θ_{max} is the maximum θ-scan angle which is a design parameter.

5.4. Appendices

Appendix A: Derivation of Equation (5-9)

Consider a spherical reflector illuminated by a plane wave parallel to the z'-axis as shown in Fig. 5-4. The incident ray strikes the reflector at point (x'_1, z'_1) is reflected as ray $P'_1P'_2$. The surface normal of the spherical reflector at point (x'_1, z'_1) is along the spherical radius from the center of the sphere O. From Snell's law the angles α and β in Fig. 5-4 are equal. Also, $\alpha=\gamma$ because the incident ray is parallel to z'-axis. On the other hand $\xi=\beta+\gamma$ because of the trigonometrical relationship shown in Fig. 5-4. Therefore, we conclude that

$$\xi = 2\gamma \tag{5-18}$$

From the geometry in Fig. 5-4 we also have

$$\tan\gamma = -\frac{x'_1}{z'_1} \tag{5-19}$$

Substituting (5-18) into (5-19) leads to

$$\tan\xi = \frac{2\tan\gamma}{1-\tan^2\gamma} = -\frac{2\,x'_1\,z'_1}{z'^2_1 - x'^2_1} \tag{5-20}$$

Since tan ξ is the same as the slope of ray $P'_1P'_2$, it can be used to obtain the linear equation for ray $P'_1P'_2$. Knowing that ray $P'_1P'_2$ goes through (x'_1, z'_1), every point (x, z) on ray $P'_1P'_2$ can be expressed as,

$$\frac{x'_1 - x}{z - z'_1} = \tan\xi \tag{5-21}$$

Substituting (5-20) into (5-21) gives the following linear equation for every point (x, z) on ray $P'_1P'_2$

$$x'_1 - x = -\frac{2\,x'_1\,z'_1}{z'^2_1 - x'^2_1}(z - z'_1) \tag{5-22}$$

Evaluating this for the point where ray $P'_1P'_2$ strikes the subreflector, (x'_2, z'_2), yields

$$x'_1 - x'_2 = -\frac{2\,x'_1\,z'_1}{z'^{\,2}_1 - x'^{\,2}_1}\,(z'_2 - z'_1) \tag{5-23}$$

Recall $x'^{\,2}_1 + z'^{\,2}_1 = R^2$, so that (5-23) can be rewritten as

$$x'_1 - x'_2 = -\frac{2\,x'_1\,z'_1}{2\,z'^{\,2}_1 - R^2}\,(z'_2 - z'_1) \tag{5-24}$$

which is (5-9).

Appendix B: Derivation of Equation (5-11)

The surface derivative on the tertiary is derived from ray $P'_fP'_3P'_2$ which starts at the feed location $(0, z'_f)$ is reflected from the tertiary at (x'_3, z'_3), and ends at the subreflector point (x'_2, z'_2). This part of the ray has a path length l which is evaluated from

$$l(x'_3, z'_3) = \sqrt{(x'_3 - 0)^2 + (z'_3 - z'_f)^2} + \sqrt{(x'_2 - x'_3)^2 + (z'_2 - z'_3)^2} \tag{5-25}$$

where (x'_3, z'_3) are the only variables since points $(0, z'_f)$ and (x'_2, z'_2) are fixed. Since (x'_3, z'_3) is a function of (r', θ') according to (5-8), l can be expressed as a function of (r', θ') with the partial derivative relations shown in (5-26)

$$\begin{aligned} \frac{\partial l}{\partial \theta'} &= \frac{\partial l}{\partial x'_3}\,\frac{\partial x'_3}{\partial \theta'} + \frac{\partial l}{\partial z'_3}\,\frac{\partial z'_3}{\partial \theta'} \\ \frac{\partial l}{\partial r'} &= \frac{\partial l}{\partial x'_3}\,\frac{\partial x'_3}{\partial r'} + \frac{\partial l}{\partial z'_3}\,\frac{\partial z'_3}{\partial r'} \end{aligned} \tag{5-26}$$

where the partial derivatives are easily evaluated from (5-8) as

$$\frac{\partial x'_3}{\partial \theta'} = r' \cos\theta'$$

$$\frac{\partial z'_3}{\partial \theta'} = r' \sin\theta'$$

$$\frac{\partial x'_3}{\partial r'} = \sin\theta'$$

$$\frac{\partial z'_3}{\partial r'} = -\cos\theta' \qquad (5\text{-}27)$$

where $\frac{dr'}{d\theta'}$ is the surface derivative of the tertiary at (x'_3, z'_3). Substituting (5-27) into (5-26) yields

$$\frac{\partial l}{\partial \theta'} = \frac{\partial l}{\partial x'_3} r'\cos\theta' + \frac{\partial l}{\partial z'_3} r'\sin\theta'$$

$$\frac{\partial l}{\partial r'} = \frac{\partial l}{\partial x'_3} \sin\theta' - \frac{\partial l}{\partial z'_3} \cos\theta' \qquad (5\text{-}28)$$

The remaining partial derivatives in (5-28) are derived from (5-25) as

$$\frac{\partial l}{\partial x'_3} = \frac{(x'_3 - 0)}{\sqrt{(x'_3 - 0)^2 + (z'_3 - z'_f)^2}} + \frac{(x'_3 - x'_2)}{\sqrt{(x'_3 - x'_2)^2 + (z'_3 - z'_2)^2}}$$

$$\frac{\partial l}{\partial z'_3} = \frac{(z'_3 - z'_f)}{\sqrt{(x'_3 - 0)^2 + (z'_3 - z'_f)^2}} + \frac{(z'_3 - z'_2)}{\sqrt{(x'_3 - x'_2)^2 + (z'_3 - z'_2)^2}} \qquad (5\text{-}29)$$

Substituting the remaining partial derivatives in (5-28) according to (5-29), and using the geometrical relationship $r' = \sqrt{(x'_3 - 0)^2 + (z'_3 - z'_f)^2}$, we have

$$\frac{\partial l}{\partial \theta'} = \left(\frac{x'_3}{r'} + \frac{(x'_3 - x'_2)}{\sqrt{(x'_3 - x'_2)^2 + (z'_3 - z'_2)^2}} \right) r'\cos\theta'$$

$$+ \left(\frac{(z'_3 - z'_f)}{r'} + \frac{(z'_3 - z'_2)}{\sqrt{(x'_3 - x'_2)^2 + (z'_3 - z'_2)^2}} \right) r'\sin\theta'$$

$$\frac{\partial l}{\partial r'} = \left(\frac{x'_3}{r'} + \frac{(x'_3 - x'_2)}{\sqrt{(x'_3 - x'_2)^2 + (z'_3 - z'_2)^2}} \right) \sin\theta'$$

$$- \left(\frac{(z'_3 - z'_f)}{r'} + \frac{(z'_3 - z'_2)}{\sqrt{(x'_3 - x'_2)^2 + (z'_3 - z'_2)^2}} \right) \cos\theta' \qquad (5\text{-}30)$$

The geometrical relationship (5-8) can be rewritten as $\frac{x'_3}{r'}=\sin\theta'$ and

$\frac{(z'_3-z'_f)}{r'}=-\cos\theta'$. So (5-30) can be further simplified to

$$\frac{\partial l}{\partial \theta'}=\left(\frac{(x'_3-x'_2)}{\sqrt{(x'_3-x'_2)^2+(z'_3-z'_2)^2}}\right)r'\cos\theta'+\left(\frac{(z'_3-z'_2)}{\sqrt{(x'_3-x'_2)^2+(z'_3-z'_2)^2}}\right)r'\sin\theta'$$

$$\frac{\partial l}{\partial r'}=$$

$$\left(\sin\theta'+\frac{(x'_3-x'_2)}{\sqrt{(x'_3-x'_2)^2+(z'_3-z'_2)^2}}\right)\sin\theta'+\left(\cos\theta'-\frac{(z'_3-z'_2)}{\sqrt{(x'_3-x'_2)^2+(z'_3-z'_2)^2}}\right)\cos\theta' \tag{5-31}$$

Furthermore, Snell's law on the tertiary requires that $\frac{dl}{d\theta'}=\frac{\partial l}{\partial \theta'}+\frac{\partial l}{\partial r'}\frac{dr'}{d\theta'}=0$, which is equivalent to

$$\frac{dr'}{d\theta'}=-\frac{\frac{\partial l}{\partial \theta'}}{\frac{\partial l}{\partial r'}} \tag{5-32}$$

Substituting (5-31) into (5-32), (5-11) can be obtained.

Chapter 6
THE IMPROVED SPHERICAL TRI-REFLECTOR SYSTEM WITH A FLAT MIRROR

The low aperture efficiency problem common in spherical tri-reflector systems was overcome by the tri-reflector design as described in the previous chapter. In order to further simplify the mechanical motion, and therefore, improve the economy of such systems, studies were made on techniques to reduce the degrees of motion. In a typical configuration, the moving subreflector and tertiary should be as small as possible and the feed should remain fixed. Watanabe et al. [16] proposed a beam waveguide configuration which permits a fixed feed. The beam waveguide portion consists of two prime focus parabolic reflectors which creates the image of the real feed. The beam waveguide moves in such a way that the image of the real feed moves as required for scan. This, of course, reduces the complexity of the feed; however, the massive beam waveguide must move in addition to the subreflector and tertiary.

In order to reduce the mass of moving parts in the antenna system, we investigated various optical configurations which form movable images of the suboptics assembly. As a result, we found that with proper placement of a plane mirror, an image of the entire suboptics assembly is created without blockage. Scan can then be achieved by rotating the mirror creating a rotating image of the suboptics assembly. The system designed for the test case in the next chapter scans $\pm 5^{\circ}$ in both orthogonal directions. Since the mirror creates the image of the entire suboptics assembly, not only is the feed fixed, but the subreflector and the tertiary are all fixed.

6.1. Fixing the Suboptics Assembly by Mirror Imaging

The configuration that permits the suboptics assembly to remained fixed uses a mirror as illustrated in Fig. 6-1, which shows a dual-caustic spherical tri-reflector system [1] in Fig. 6-1a and the version with a mirror in Fig. 6-1b. The mirror creates the image of the suboptics assembly as shown in Fig. 6-1c, and behaves effectively the same as the real suboptics assembly in Fig. 6-1a during

scan. This is because, according to geometrical optics (GO) principles, a mirror creates an image without aberration. Physical optics (PO) shows that diffraction loss is present because of the finite size of the mirror. However, in the designs we have encountered (mirror diameter $\simeq 70\lambda$), diffraction loss is negligible.

The suboptics in Fig. 6-1 is synthesized by the method discussed in Chapter 5, and such suboptics forms a dual-caustic configuration. The suboptics assembly in Fig. 6-1a is placed in such a way that the output main beam is parallel to the z axis. The spherical coordinate system with z axis as its axis is the *antenna coordinate*. In Fig. 6-1b the real suboptics assembly is identical to that in Fig. 6-1a. The plane containing the mirror in Fig. 6-1b passes though the center, O, of the spherical main reflector. Thus, the image of the suboptics assembly in Fig. 6-1c creates an output main beam that is parallel to the z′ axis and forms an angle θ from z axis. Scan is achieved by rotating the mirror about O, and therefore, rotating the virtual suboptics and the main beam.

Two angles are required to determine the rotation of the mirror about the spherical center. One is the angle between the mirror plane and the z axis (α), and the other is the azimuthal angle of the mirror surface normal (ϕ); see Fig. 6-2 for the geometry. The mirror creates the image of the z axis; this virtual axis is called z′ and is parallel to the output main beam from the spherical main reflector. Therefore, the angle θ between the virtual axis (z′) and the z axis (θ-scan angle) is 2α. On the other hand, it is obvious from Fig. 6-2 that the azimuthal angle of the mirror surface normal ($\hat{n}$) is the same azimuthal angle as for the virtual z′ axis (ϕ-scan angle). These geometrical relationships are summarized as follows:

$$\begin{cases} 2\,\alpha_{\text{mirror}} = \theta \\ \\ \phi_{\text{mirror}} = \phi \end{cases} \tag{6-1}$$

This simple equation specifies the mechanical rotation of the mirror required for scan of the main output beam.

6.2. Improving the Aperture Efficiency by Tilting the Feed in Azimuth

The movement of the mirror described in the last section scans the main

beam; however, it also introduces movement of the main reflector illuminated area, assuming the feed remains fixed during scan. This, of course, reduces the aperture efficiency. In fact, the motion of the main reflector illuminated area can be so severe (especially during ϕ-scan) that the aperture utilization becomes unacceptable (<30%) for $\pm 5^\circ$ circular scan coverage.

The problem of poor aperture utilization can be alleviated to large extent by implementing the feed tilt method as described in the last chapter. By tilting the feed in both azimuth and elevation, the main reflector illuminated area can be totally fixed during scan, and therefore, the aperture efficiency can be as high as 70% (see the next chapter). In practice, it is much easier to tilt the feed only in azimuth than in both angles. Azimuth feed tilt greatly reduces the motion of the aperture illuminated area, although it allows the aperture illumination to move during θ-scan. The aperture efficiency for azimuth only feed tilt (about 50% as seen in the next chapter) is less than the 70% aperture efficiency obtained when the feed is tilted in both azimuth and elevation. However, it is a great improvement from the fixed feed case. For most practical applications, the azimuth-only feed tilt method is the most advantageous considering the trade-off between aperture efficiency and feed system complicity.

Detailed aperture utilization analysis is necessary to show the effectiveness of feed tilting method and to obtain the proper feed tilting angle as a function of scan angle. The key to the aperture utilization analysis is to study the motion of the center of the aperture illuminated area, which is marked C′ in Fig. 6-2. The mirror image of C′ is C, which is the center of "illumination" for the virtual main reflector. C does not move when the mirror is rotated to scan, it only moves when the feed tilts. Point C is found from the mapping equations (5-7) and (5-8) for the feed ray that is along the axis of the feed. C′ is the mirror image of C, and is found by (6-2)

$$\vec{r}'_c = \vec{r}_c - 2\,(\hat{n}\cdot\vec{r}_c)\,\hat{n} \qquad (6\text{-}2)$$

where $\hat{n}$ is the surface normal of the mirror. A mirror coordinate system is established with x_m axis along $\hat{n}$, and y_m axis in the plane of x and y; see Fig. 6-2. The coordinate transformation between the antenna coordinates (x, y, z) and the mirror coordinates can be written as

$$\begin{bmatrix} x \\ y \\ z \end{bmatrix} = \begin{bmatrix} \cos\alpha\cos\phi & -\sin\phi & \sin\alpha\cos\phi \\ \cos\alpha\sin\phi & \cos\phi & \sin\alpha\sin\phi \\ -\sin\alpha & & \cos\alpha \end{bmatrix} \begin{bmatrix} x' \\ y' \\ z' \end{bmatrix} = \mathrm{T} \begin{bmatrix} x' \\ y' \\ z' \end{bmatrix} \qquad (6\text{-}3)$$

This coordinate rotation matrix, T, with $\hat{n}=\hat{x}_m$ permits (6-2) to be written as (in the antenna coordinates)

$$\begin{bmatrix} x'_c \\ y'_c \\ z'_c \end{bmatrix} = \mathrm{T} \begin{bmatrix} -1 & 0 & 0 \\ 0 & 1 & 0 \\ 0 & 0 & 1 \end{bmatrix} \mathrm{T}^t \begin{bmatrix} x_c \\ y_c \\ z_c \end{bmatrix} = \mathrm{R} \begin{bmatrix} x_c \\ y_c \\ z_c \end{bmatrix} \qquad (6\text{-}4)$$

where T^t is the transpose of T. The general mirror reflection matrix, which gives the mirror image of any vector, is formed by multiplying out the three matrices in (6-4) giving

$$\mathrm{R} = \begin{bmatrix} -\cos\theta\cos^2\phi+\sin^2\phi & -(\cos\theta+1)\frac{\sin 2\phi}{2} & \sin\theta\cos\phi \\ -(\cos\theta+1)\frac{\sin 2\phi}{2} & -\cos\theta\sin^2\phi+\cos^2\phi & \sin\theta\sin\phi \\ \sin\theta\cos\phi & \sin\theta\sin\phi & 1 \end{bmatrix} \qquad (6\text{-}5)$$

where θ and ϕ are scan angles in antenna coordinates and (6-1) is used to replace α with θ.

For simplicity, we first consider a fixed feed which causes the "illumination" center of the virtual main reflector, C, to lie in the xz-plane (ϕ_c=0); the direction to C, $\vec{r}_c$, forms angle θ_c from the $-z$ axis. Therefore, point C′ on the sphere is expressed in antenna coordinates as

$$\hat{r}'_c = R\,\vec{r}_c = \begin{bmatrix} (\cos\theta\,\cos^2\phi - \sin^2\phi)\sin\theta_c - \sin\theta\,\cos\phi\,\cos\theta_c \\ (\cos\theta+1)\dfrac{\sin 2\phi}{2}\,\sin\theta_c - \sin\theta\,\sin\phi\,\cos\theta_c \\ -\sin\theta\,\cos\phi\,\sin\theta_c - \cos\theta_c \end{bmatrix} \qquad (6\text{-}6)$$

where the angle between $\hat{r}'_c$ and $-z$ axis is θ'_c, and the azimuth angle of $\hat{r}'_c$ in the xy plane is ϕ'_c; they are found by coordinates of $\hat{r}'_c$ in (6-6) as

$$\tan\theta'_c = -\frac{x'_c}{z'_c} = \frac{(\cos\theta\,\cos^2\phi - \sin^2\phi)\,\sin\theta_c - \sin\theta\,\cos\phi\,\cos\theta_c}{\sin\theta\,\cos\phi\,\sin\theta_c + \cos\theta_c} \qquad (6\text{-}7)$$

and

$$\tan\phi'_c = \frac{x'_c}{y'_c} = \frac{(\cos\theta+1)\dfrac{\sin 2\phi}{2}\,\sin\theta_c - \sin\theta\,\sin\phi\,\cos\theta_c}{(\cos\theta\,\cos^2\phi - \sin^2\phi)\,\sin\theta_c - \sin\theta\,\cos\phi\,\cos\theta_c} \qquad (6\text{-}8)$$

The functional relationship between ϕ'_c and ϕ given in (6-8) is of particular interest, and is plotted as the $\phi_c = 0^\circ$ curve in Fig. 6-3 (0° feed tilt). This curve shows that the change of ϕ'_c is more than double the change of ϕ. This means that the azimuth angle of the main reflector illumination center C' is very sensitive to ϕ scan, due to mirror rotation during ϕ-scan. Furthermore, as explained in the following discussion, a large dynamic ϕ-scan range is required to cover a normal circular scan region; e.g. $\pm 5^\circ$ scan requires $\pm 28^\circ$ ϕ-scan range for our test case in the next chapter.

The large ϕ-scan range requirement is a disadvantage of this system. This requirement is explained in Fig. 6-4. The z_s axis in Fig. 6-4 is directed toward the center of the scan region and forms an angle θ_0 from the z axis. The angle θ_0 is non zero because of the offsetting for the antenna system explained in Chapter

5. However, the offsetting only occurs in the xz plane. We establish a scan coordinate system with x_s axis in the xy plane and y_s axis the same as y axis. The coordinate transformation between scan coordinates and antenna coordinates is

$$\begin{bmatrix} x \\ y \\ z \end{bmatrix} = \begin{bmatrix} \cos\theta_0 & 0 & \sin\theta_0 \\ 0 & 1 & 0 \\ -\sin\theta_0 & 0 & \cos\theta_0 \end{bmatrix} \begin{bmatrix} x_s \\ y_s \\ z_s \end{bmatrix} \tag{6-9}$$

For a main beam direction (z′ direction) with scan angles θ_s from z_s axis and azimuthal angle ϕ_s in the scan coordinates, the (θ, ϕ) angles in the antenna coordinates can be found from (6-9) as

$$\begin{bmatrix} \sin\theta\cos\phi \\ \sin\theta\sin\phi \\ \cos\theta \end{bmatrix} = \begin{bmatrix} \cos\theta_0 \sin\theta_s \cos\phi_s + \sin\theta_0 \cos\theta_s \\ \sin\theta_s \sin\phi_s \\ -\sin\theta_0 \sin\theta_s \cos\phi_s + \cos\theta_0 \cos\theta_s \end{bmatrix} \tag{6-10}$$

The azimuthal angle ϕ in antenna coordinates is, therefore,

$$\tan\phi = \frac{\sin\theta_s \sin\phi_s}{\cos\theta_0 \sin\theta_s \cos\phi_s + \sin\theta_0 \cos\theta_s} \tag{6-11}$$

Since we are interested in the maximum (mirror rotation) ϕ angle required to perform scan, the change of ϕ along the boundary of the scan region is of particular interest. This boundary for our test case (see the next chapter) is

θ_s=5° and ϕ_s=0° ~ 360°. The corresponding values of ϕ as a function of ϕ_s along the boundary are plotted in Fig. 6-5, which shows that a maximum of $\pm 28°$ is required for the dynamic ϕ range.

In the above discussion we first showed that the location of the main reflector illumination is very sensitive to ϕ scan, and then showed that a large ϕ-scan range is required to perform a circular scan coverage. These two points make it necessary to tilt the feed to reduce the motion of the main reflector illuminated area.

The azimuthal feed tilt method can be explained using Fig. 6-6. Since the antenna system was synthesized according to a parent reflector system that is axisymmetric about the z axis, the azimuthal feed tilt about the z axis, given by the angle ϕ_f, is equivalent to rotating the whole antenna about the z axis by an angle ϕ_f. Therefore, (6-8) becomes

$$\tan(\phi'_c - \phi_f) = \frac{(\cos\theta+1)\dfrac{\sin 2(\phi-\phi_f)}{2}\sin\theta_c - \sin\theta\,\sin(\phi-\phi_f)\,\cos\theta_c}{(\cos\theta\,\cos^2(\phi-\phi_f) - \sin^2(\phi-\phi_f))\,\sin\theta_c - \sin\theta\,\cos(\phi-\phi_f)\,\cos\theta_c} \tag{6-12}$$

The values of ϕ'_c as functions of ϕ in (6-12) with various feed tilt angle ϕ_f are plotted in Fig. 6-3. The intersections between constant ϕ_f curves and the horizontal axis of Fig. 6-3 correspond to conditions for ϕ'_c=0 (no azimuthal motion for the main reflector illuminated area). While the antenna is scanning, (6-12) can be solved in real time for the ϕ'_c=0 condition to obtain the correct feed tilt angle ϕ_f for each ϕ-scan angle.

6.3. Choosing Mirror Motion Axes to Reduce the Mirror Size

The mirror is the major moving part in the reflector system; therefore, minimizing the size of the mirror is very important. The size of the mirror is determined by the illuminated area in the plane of the mirror and the relative motion between this illuminated area and the mirror. The mirror must cover the directly the illuminated area in the plane of the mirror at all scan angles (in GO sense). Moreover, the mirror must be oversized in order to reduce diffraction loss. In order to reduce the size of the mirror, the relative motion between the mirror and its illuminated area must be minimized; i.e. the mirror motion must follow the motion of the illuminated area in the mirror plane during scan.

The mirror motion during scan can be achieved by one degree of linear translation and rotation about two axis; see Fig. 6-6. In theory, the direction of the translational axis t has many possible values, so does the location of the rotational axes y'_m and z'_m. Once all the axes are chosen, the amount of translation and rotation is determined from scan angles by a coordinate transformation from antenna coordinates to mirror coordinates. In order to reduce the relative motion between the mirror and its illuminated area, the t axis is best chosen to be along the ray from the subreflector illumination center to the virtual main reflector illumination center at zero ϕ-scan angle.

Naturally, the z'_m axis is chosen on the surface of the mirror. This, however, introduces a relative motion between the mirror and its illuminated area during ϕ scan because of the feed azimuth tilt. To alleviate this problem,

the rotational axis z'_m is chosen to be above the plane of the mirror; see Fig. 6-6. Since the rotational axis is off the mirror, the mirror translates during the rotation to follow the motion of illuminated area.

The choices for z'_m axis can be performed numerically by analyzing the coordinate data for the illumination center on the mirror at different scan angles. The graphical display of such data shows that the mirror area can be reduce by 50% by properly choosing the z'_m axis.

Chapter 7
PO ANALYSIS RESULTS

Physical optics analysis was performed to evaluate the performance of the proposed spherical main reflector scanning system. The analysis includes three stages. First, the spherical tri-reflector system without the mirror was analyzed to verify the synthesis method discussed in Ch. 5 and to verify that its performance remains constant during θ-scan. In the second analysis phase PO is performed on the spherical tri-reflector system with a mirror. The performance degradation due to the mirror was studied. In the third phase of investigation the effects of mechanical distortion were studied and the results showed that the proposed spherical tri-reflector system with a mirror has high tolerance to deterministic mechanical distortions.

7.1. PO Analysis of the Spherical Tri-Reflector System without Mirror

The spherical tri-reflector configuration used for PO analysis verification was the single-caustic system of Fig 5-2a with dimensions listed in Table 7-1. The choice for this geometry is motivated by NASA's test program to verify the 25-m diameter class space antenna concept. The test bed, which is called the Bush model, requires a $D = 10$ m diameter main reflector with focal length $F \simeq 12.7$ m. The proposed configuration in Table 7-1 closely fits that requirement. The parameters of the proposed configuration were selected for smallest subreflector size by inspecting the graphics simulation of the configuration on a computer screen. The parameters modified during such optimization are the subreflector location, the tertiary location, the feed location and the mapping normalization factor $q = 1$ used in the synthesis (see Ch. 5).

The GRASP7 code [15] was used for the PO analysis. It is a state-of-the-art commercial code mainly designed for dual-reflector antenna analysis. Multiple steps were required to analyze multireflector systems using GRASP7. First, the feed-tertiary-subreflector system was treated as a dual reflector system and PO analysis was performed, yielding the current distribution on the subreflector. This current distribution is saved in a data file, and then used in

PO analysis to calculate the current distribution on the main reflector. Finally, GRASP7 PO integration is used in the main reflector to obtain the far field pattern.

The GRASP7 PO analysis results are summarized in Table 7-1. Pattern data from GRASP7 are shown in Fig. 7-1 for three θ-scan angles. Note from Fig. 7-1 that the feed tilt motion required to accomplish the main beam scan does not change the critical performance parameter values such as gain and side lobe level. Cross polarization does increase with θ-scan angle; however, it is within the tolerance (< -35 dB).

These results verify the synthesis method discussed in Ch. 5. They also show that the θ-scan method maintains constant gain while offering aperture efficiency ($\epsilon_{ap} = 70\%$) as high as that from a prime focus unscanned paraboloidal reflector.

7.2. PO Analysis for Spherical Tri-Reflector System with Mirror

The test configuration of spherical tri-reflector system with mirror was shown in Fig. 6-1. It is based on a dual-caustic spherical tri-reflector system synthesized by the method explained in Ch. 5. The dimensions of this test configuration are those of the NASA test bed, and are listed in Table 7-2.

The PO analysis for this test system involves three steps. In the first step, the feed-tertiary-subreflector is treated as a dual reflector system for GRASP7 PO analysis. The resultant subreflector current distribution was saved. Then the subreflector-mirror was treated as a dual reflector system; the subreflector current was used to calculate the mirror current. In the last step, the mirror-main reflector was treated as a dual reflector system; the mirror current is used to calculate the main reflector current and then, the far field pattern.

The resultant pattern is shown in Fig. 7-2 for the spherical tri-reflector system with mirror. Fig. 7-3 shows the pattern for the parent spherical tri-reflector system without a mirror. The patterns in Fig. 7-2 are approximately the mirror image of those in Fig. 7-3. Therefore, the mirror did not cause significant performance degradation. The performance parameters extracted

from Fig. 7-2 are listed in Table 7-2. The cross polarization level in Fig. 7-2 and Fig. 7-3 is higher than the one in Fig. 7-1. This is because the configuration is highly offset in order to place the mirror without blockage; high offset introduces high cross polarization. This is a disadvantage of the spherical-tri-reflector-with-mirror system.

7.3. Mechanical Error Sensitivity Analysis

The sensitivity of the antenna performance to mechanical distortion is important in space applications. The mechanical error is caused by manufacturing imperfections, thermal expansion and zero gravity in space. Such errors are deterministic, i.e. the overall reflector surface shape or reflector location is changed, but the surface is kept smooth and monotonic. Our mechanical error sensitivity study uses PO analysis on the spherical tri-reflector with mirror system mentioned in Table 7-2. Errors are introduced by displacing each reflector sequentially.

The error sensitivity analysis includes three steps. First, the feed was translated in x and z directions of the antenna coordinates (see Fig. 6-4 for coordinate definition), and PO analysis was performed as discussed in Section 7.2. Then, the tertiary was displaced and the same PO analysis was performed. Finally, the subreflector was dislocated and then the same PO analysis was performed. The main reflector and mirror dislocation was not analyzed because it was equivalent to the overall dislocation for feed-tertiary-subreflector.

The results in Table 7-3 show that the proposed spherical tri-reflector system is tolerant to mechanical distortion. For 0.5λ (or 1 cm at 15 GHz) displacement of the feed, tertiary and subreflector individually, the performance degradation is negligible. This demonstrates that our antenna design is practical for space applications.

Table 7-1

Geometry Data and PO Analysis Results for the Single-Caustic Test Configuration

Quantity	Value
Antenna Configuration:	
θ-scan range	10°
ϕ-scan range	360°
Feed tilt range	$11.38^\circ \sim 21.38^\circ$
Frequency	30 GHz
Main spherical reflector	D=10m
	R=25m
Shaped sub-reflector size	3.0m x 1.6m
Shaped tertiary size	2.4m x 1.7m
Gaussian feed	-12 dB taper at $\pm 16^\circ$
Main reflector location	$z'_{10} = -25$ m*
Subreflector location	$z'_{20} = -12$ m*
Tertiary location	$z'_{30} = -15$ m*
Feed location	$z'_f = -12$ m*
PO Results from GRASP7:	
Gain	68.4 dB
Gain variation in scan	± 0.03 dB
Aperture efficiency	70%
Side lobe level	<-25 dB **
Cross polarization	<-35 dB **
Beam efficiency	85%

* See Fig. 5-2 for the geometry and symbol definition

** relative to the main beam peak

Table 7-2

Geometry Data and PO Analysis Results for the Dual-Caustic with Mirror Test Configuration

Quantity	Value
Antenna Configuration:	
θ-scan range (see Fig. 6-4)	
antenna coordinates	$5^\circ \sim 15^\circ$
scan coordinates	5°
ϕ-scan range (see Fig. 6-4)	
antenna coordinates	$\pm 28^\circ$
scan coordinates	360°
Frequency	15 GHz
Main spherical reflector	
major axis	12 m
minor axis	10 m
radius	25 m
Shaped sub-reflector size	3.2 m × 4.6 m
Shaped tertiary size	2.7 m × 4.2 m
Mirror size	< 2.8 m × 4.2 m
Gaussian feed	−15 dB taper at $\pm 22.4^\circ$
Main reflector location	$z_{10} = -25$ m*
Subreflector location	$z_{20} = -12$ m*
Tertiary location	$z_{30} = -27$ m*
PO Results from GRASP7:	
Gain	63 dB
Gain variation in scan	±0.4 dB
Aperture efficiency	50%
Side lobe level	<-28 dB **
Cross polarization	<-25 dB **
Beam efficiency	93%

* See Fig. 6-1 for Geometry,

** relative to the main beam peak

Table 7-3

Summary of Mechanical Error Sensitivity Analysis at 15 GHz

Motion Parameter	Peak Shift[1]	G Change[2]	BE change	SLL Change
Feed Motion				
$\Delta x = 0.5\lambda$	0.02°	+0.07 dB	−1.2%	+3 dB
$\Delta z = 0.5\lambda$	0.04°	−0.04 dB	−1.2%	+0.5 dB
Tertiary				
$\Delta x = 0.5\lambda$	−0.02°	−0.01 dB	0.0%	+0.3 dB
$\Delta z = 0.5\lambda$	0.00°	−0.01 dB		+0.8 dB
$\Delta\theta = 0.1°$	−0.09°	−0.2 dB	−0.5%	+0.9 dB
Subreflector				
$\Delta x = 0.5\lambda$	0.04°	−0.1 dB		+1.7 dB
$\Delta z = 0.5\lambda$	−0.04°	−0.14 dB	−0.5%	+2 dB
$\Delta y = 0.5\lambda$	−0.05°	+0.01 dB	−0.1%	+0.03 dB

1: Peak Shift: Main beam pointing angle change

2: G Change: The change in peak gain

Chapter 8
CONCLUSIONS

A simple method for the synthesis of scanning spherical reflector antenna systems was presented in Chapter 5. The method yields a reflector configuration which avoids the traditional spherical reflector problems of poor aperture illumination and oversizing. Our PO results (see Table 7-1) for a 10-m sphere operating at 30 GHz show excellent antenna patterns and negligible gain loss over a 10° scan range. The spherical tri-reflector configuration has potential in reflector antenna systems with requirements for both wide scan and high gain.

The spherical reflector antenna system design can be applied to both GSO and low earth orbit satellite wide scanning antennas. If the z axis of the scan coordinate (see Fig. 3e) is directed from the satellite to the center of the earth, both the incidence angle of the beam and that of the polarization remain constant during ϕ scan. This is desirable in many remote sensing applications.

The design described in Chapter 5 offers two options. The first option uses an oversized main reflector and the suboptics assembly (consisting of the feed, subreflector and tertiary reflector) is rotated as a rigid unit to scan the main beam. The distribution across the illuminated portion of the main reflector can be controlled by the feed pattern due to the isotropic-to-uniform mapping. This could be applied to some traditional spherical main reflector systems such as the Arecibo Observatory. The second option, which was detailed in this paper, is to tilt the feed as the suboptics assembly is rotated so that the main reflector does not have to be oversized.

Mechanical properties can be further improved to realize a low cost system. For example, our study shows that if the main reflector illuminated area is allowed to move slightly during scan, the subreflector size can be reduced substantially; this, however, reduces the aperture efficiency. Also, if the F/D for the spherical main reflector is increased, the subreflector size can be reduced; of course, this increases the length of the antenna system. A tradeoff study can be performed to reduce the mass of the suboptics assembly.

Further simplification for the mechanical movement of the antenna system is achieved by the design of spherical tri-reflector with mirror discussed

in Ch 6. Tilting the plane mirror about two axes and translating in one dimension allows the whole suboptics assembly (including the feed, the subreflector and the tertiary reflector) to be fixed during scan. The feed in this system is required to tilt in azimuth during ϕ scan to achieve 50% aperture efficiency.

For the spherical tri-reflector system with mirror of Fig. 6-1, the overall mechanical motion is much simpler than previous spherical main reflector scanning systems, and the performance is superior to paraboloidal main reflector scanning systems because of the greater scan range and constant beam efficiency during scan. The mechanical simplification makes the spherical tri-reflector system with mirror practical for space as well as ground applications.

Chapter 9

REFERENCES

[1] Bing Shen and Warren L. Stutzman, "Design of Spherical Tri-Reflector Antennas with High Aperture Efficiency," IEEE Trans. on Antennas and Propagat., June 1993

[2] John Ruze, "Lateral-Feed Displacement in a Paraboloid," IEEE Trans. on Antennas and Propagat., vol AP-13, pp. 660-665, Sept. 1965.

[3] Y. Rahmat-Samii, "Reflector Antennas," Chapter 15 of Y. T. Lo and S. W. Lee, editors, Antenna Handbook, McGraw-Hill: New York, 1988.

[4] Tingye Li, "A Study of Spherical Reflectors as Wide-Angle Scanning Antennas," IRE Trans. on Antennas and Propagat., vol AP-7, pp. 223-226, July 1949

[5] W. L. Stutzman and G. S. Brown, editors, "The Science Benefits of and the Antenna Requirements for Microwave Remote Sensing from Geostationary Orbit," NASA Contractor Report 4408, Oct. 1991.

[6] W. L. Stutzman and G. A. Thiele, Antenna Theory and Design, John Wiley & Sons, Inc.: New York, 1981.

[7] J. E. Phillips and P. J. B. Clarricoats, "Optimum Design of a Gregorian-Corrected Spherical-Reflector Antenna," Proc. IEE, vol 117, No. 4, pp. 718-734, April 1970.

[8] F. S. Holt and E. L. Bouche, "A Gregorian Corrector for Spherical Reflectors," IEEE Trans. on Antennas and Propagat., vol AP-12, No. 1, pp. 44-47, January 1964.

[9] P. Ramanujam, P. J. B. Clarricoats and R. C. Brown, "Offset Spherical Reflector with a Low Side Lobe Radiation," IEEE Proceedings, vol 134, Pt. H, No. 2, pp. 199-204, April 1987.

[10] J. R. Bergmann, J. da Costa, "Offset Spherical Reflector Antenna with Low Cross Polarization," Proc. of the Int. Conf. on Ant. & Prop., (York), pp. 531-534,

April 1991.

[11] P. S. Kildal "Diffraction Analysis of a Proposed Dual-Reflector Feed for the Spherical Reflector Antenna of the Arecibo Observatory," Radio Science, vol 24, No. 5., pp. 601-617, Sept.-Oct. 1989.

[12] P. S. Kildal, "Synthesis of Multireflector Antennas by Kinematic and Dynamic Ray Tracing," IEEE Trans. on Antennas and Propagat., vol. 38, No. 10, pp. 1587-1599, Oct. 1990.

[13] F. Watanabe and Y. Mizugutch, "An Offset Spherical Tri-Reflector Antenna," Transactions of the IECE of Japan, vol E-66, No. 2, pp. 108-115, February 1983.

[14] V. Galindo-Israel, W. A. Imbriale and R. Mittra, "On the Theory of the Synthesis of Single and Dual Offset Shaped Reflector Antennas," IEEE Trans. on Antennas and Propagat., vol. AP-35, No. 8, pp. 887-896, Aug. 1987.

[15] TICRA, Manual for GRASP7, Version 7.5

[16] Watanabe et al. "Beam Waveguide Feeder," United States Patent., No. 4,516,128, May 7, 1985

[17] J. D. Kraus, Radio Astronomy 2nd Edition, Cygnus-Quasar Books, 1986

[18] W. L. Stutzman, S. Stewart, T. Pratt,
Innovative Design of Satellite Earth Terminal Antennas,
VPI&SU Project 230-11-110F-104-8026631, Report No. SATCOM T85-4, November 1985

[19] M. L. Zimmerman,
Computation and Optimization of Beam Efficiency for Reflector Antennas,
NASA grant NAG 3-419, April 1990

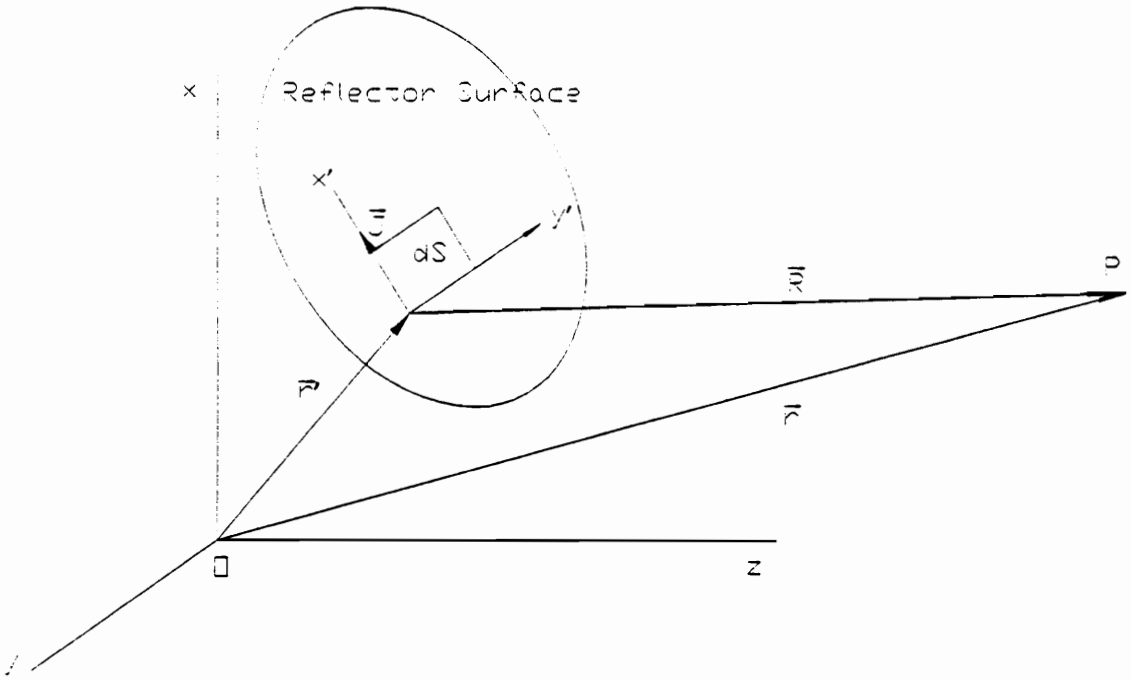

Figure 2-1. Geometry of PO Integration
Showing a differential current element $\bar{J}\,dS$

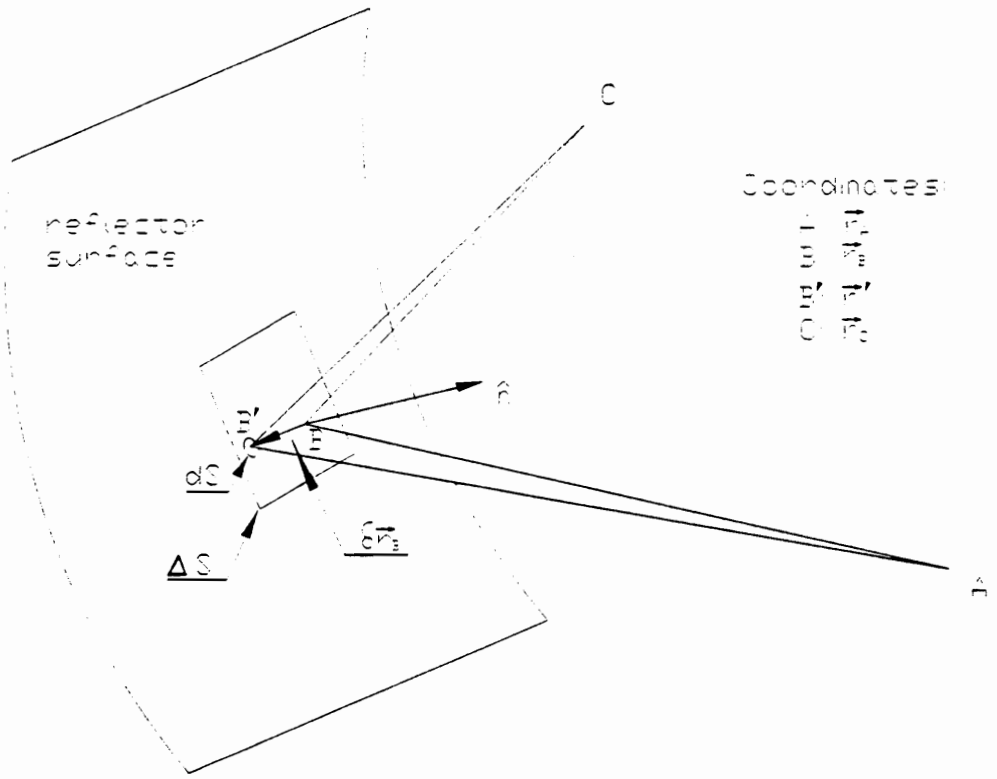

Figure 2-2. Geometry used to prove Fermat's principle from PE

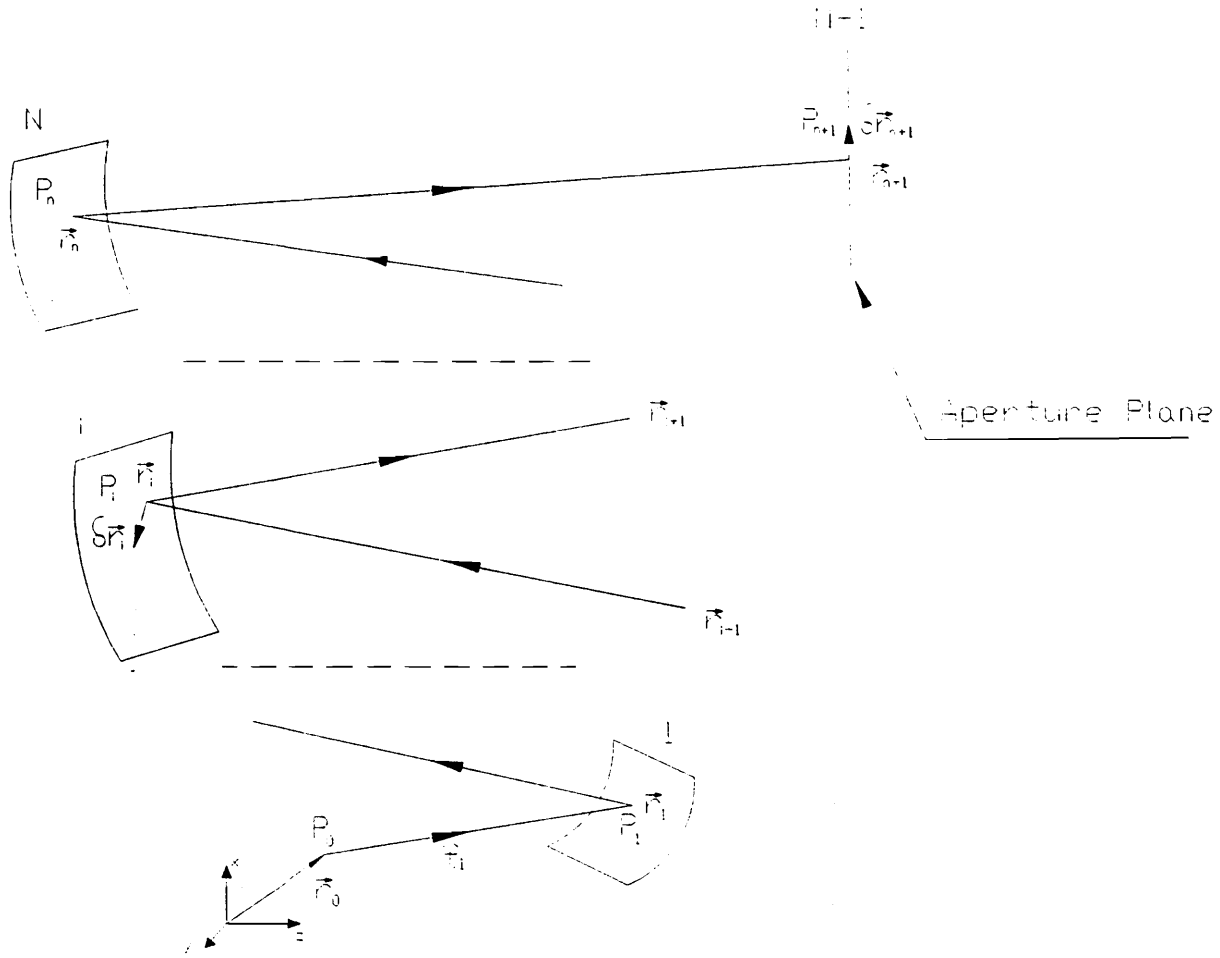

Figure 2-3 Geometry for the Ray Tracing Formulation of (2-10)

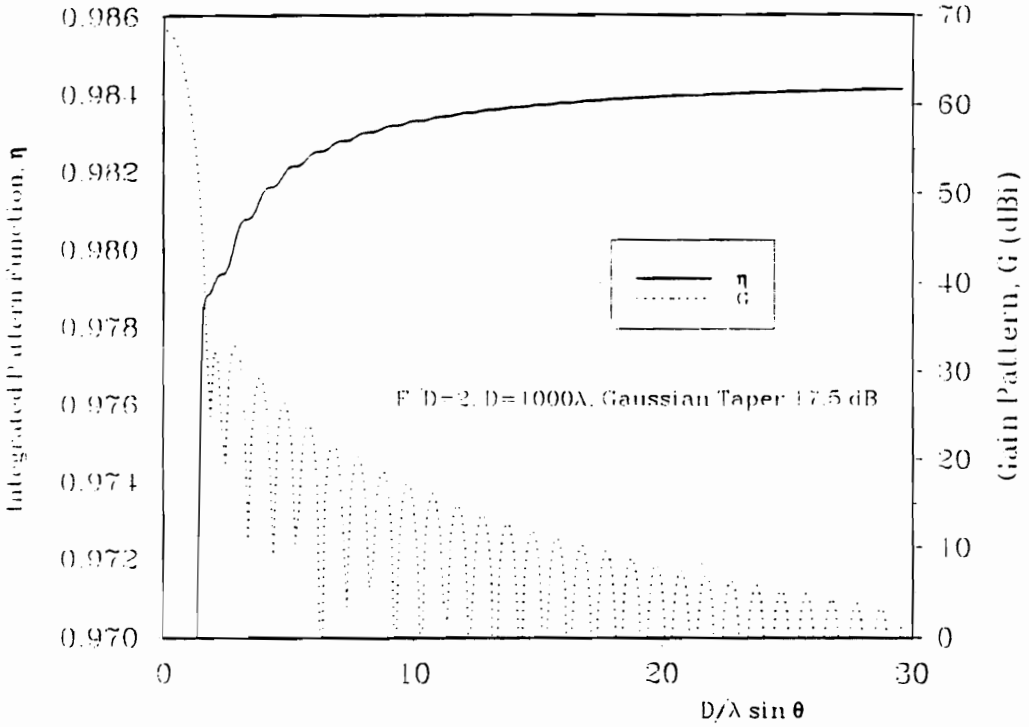

Fig. 3-1 Pattern and integrated pattern function for a prime focus paraboloid with F/D = 2, D = 1000λ, Gaussian taper 17.5 dB

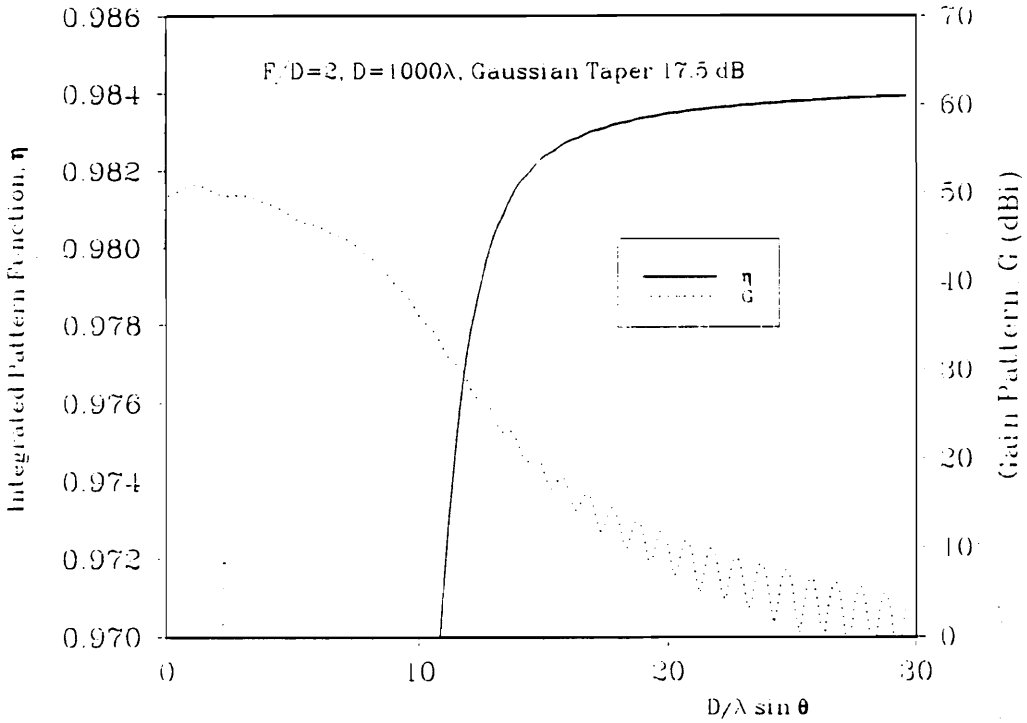

Fig. 3-2 Pattern and integrated pattern function for the antenna in Fig. 3-1 with $\delta F = 100\lambda$ distortion

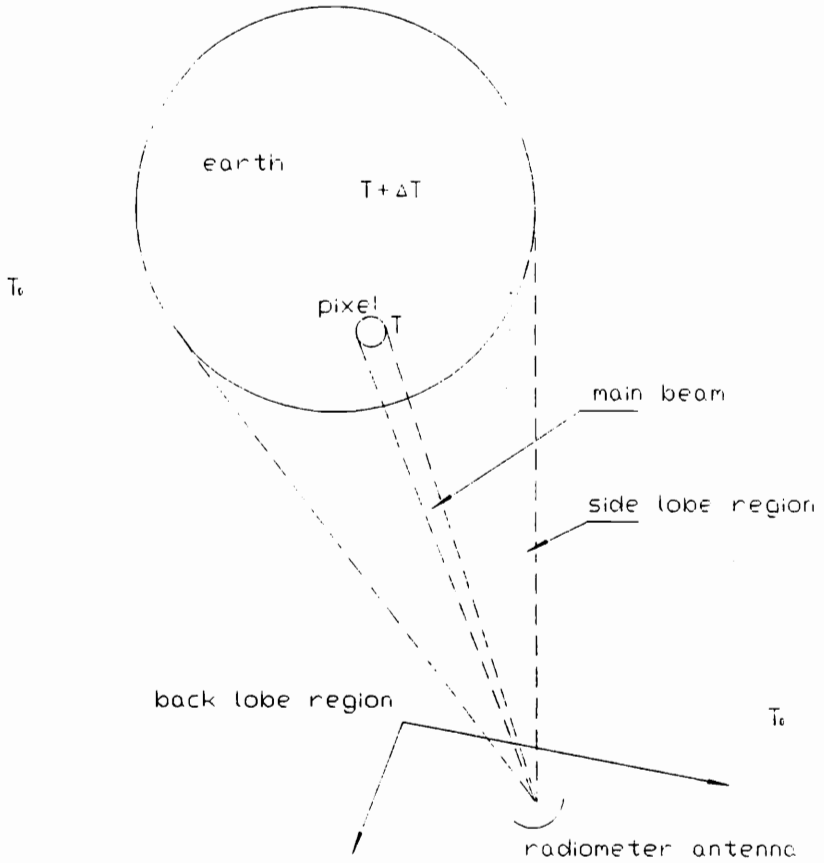

Fig. 3-3 Model of Temperature Distribution for Earth Observation Radiometers

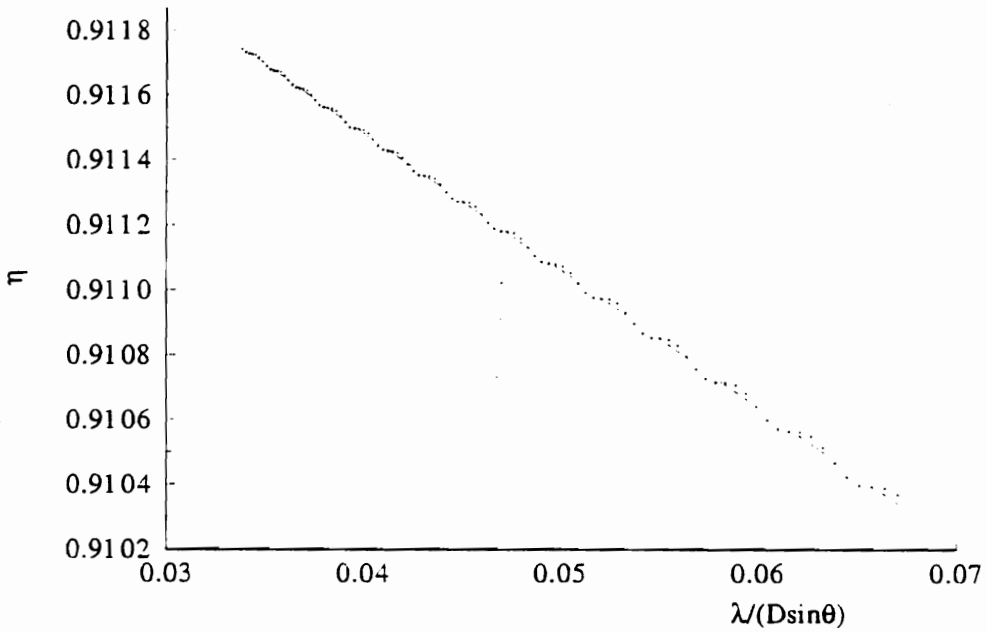

Fig. 3-4 Extrapolation of integrated pattern function for axisymmetric paraboloid with F/D=2 and 10 dB aperture edge taper

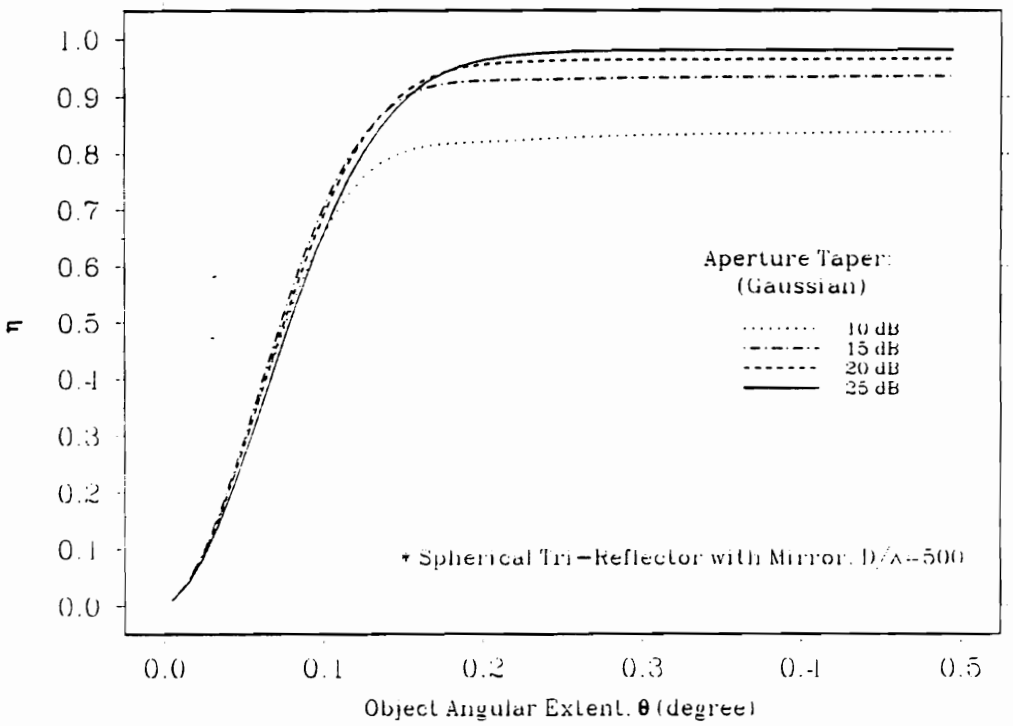

Fig. 3-5 **Integrated pattern function vs. aperture edge taper for spherical tri-reflector antenna system described in Table 7-1**

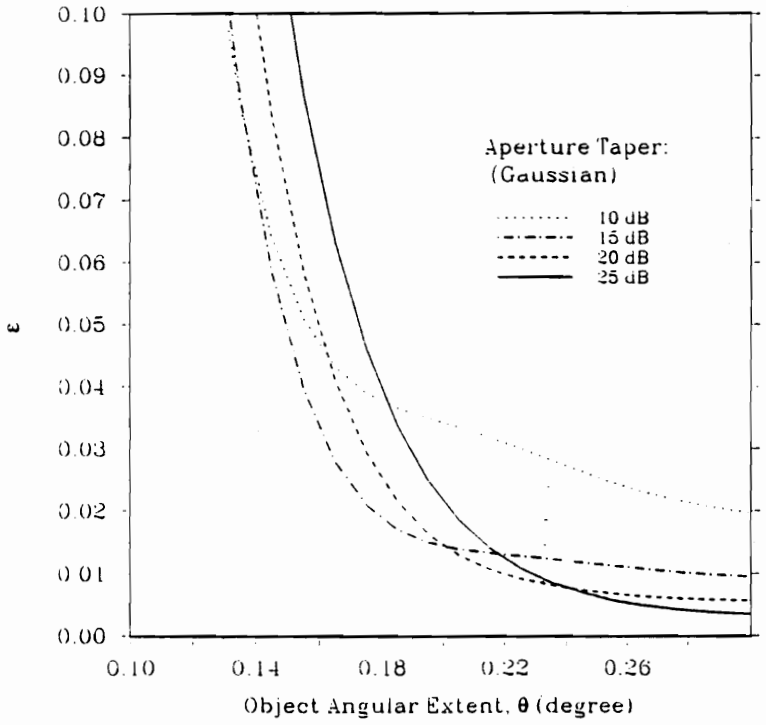

Fig. 3-6 Residue beam efficiency ratio vs. object angular extent for the spherical tri-reflector antenna system described in Table 7-1

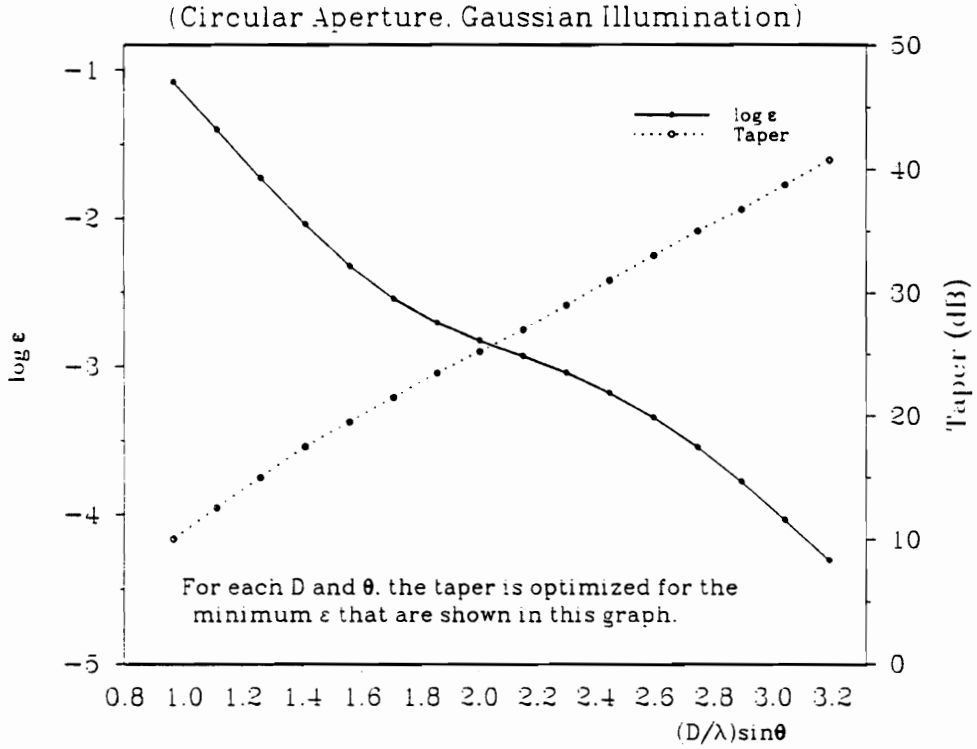

Figure 3−7 Optimum Temperature Sensitivity and Taper

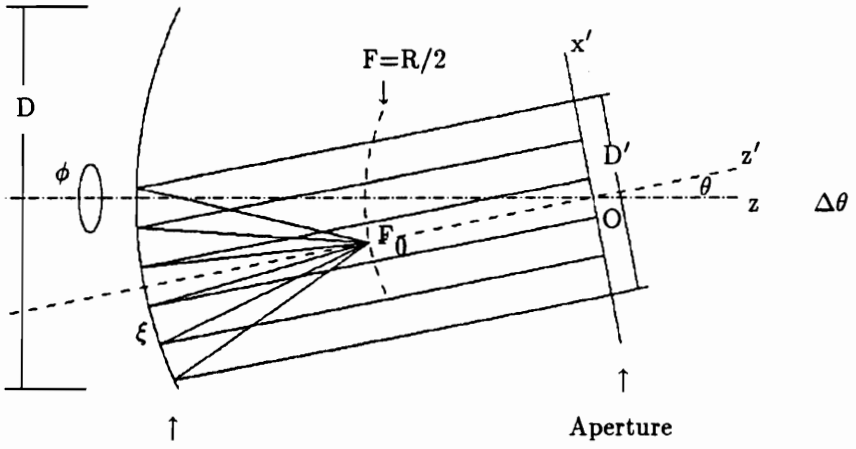

Figure 4-1. Geometry of a prime-focus spherical reflector.

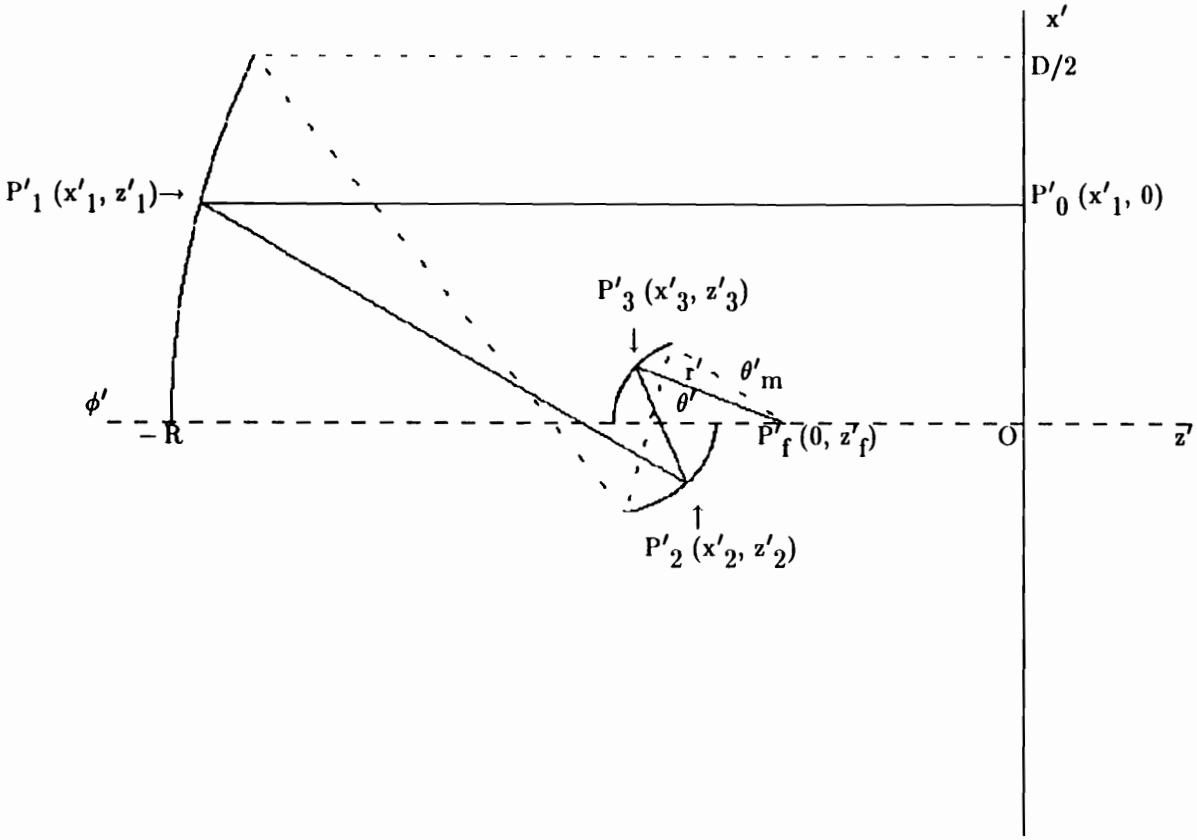

Figure 5-1. The geometry for the synthesis problem in Section 5-2 (dual caustic).

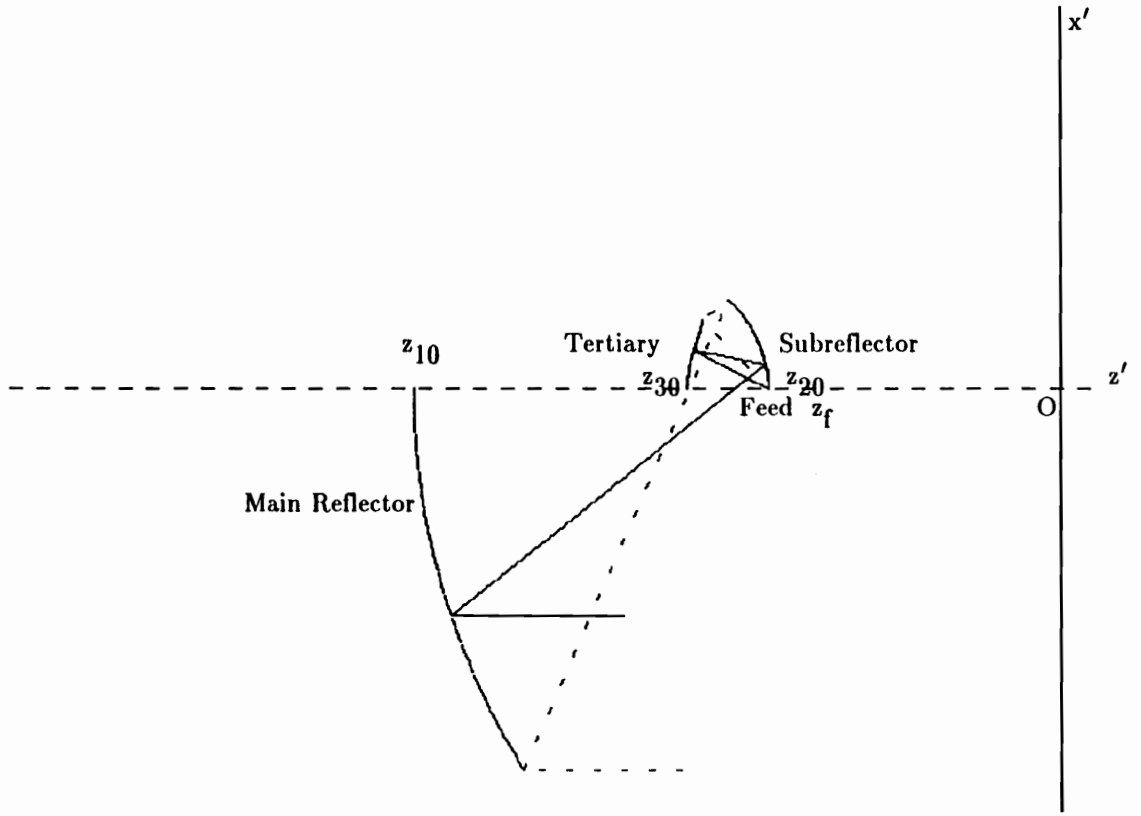

Figure 5-2. The illustration of a single caustic dual-subreflector configuration

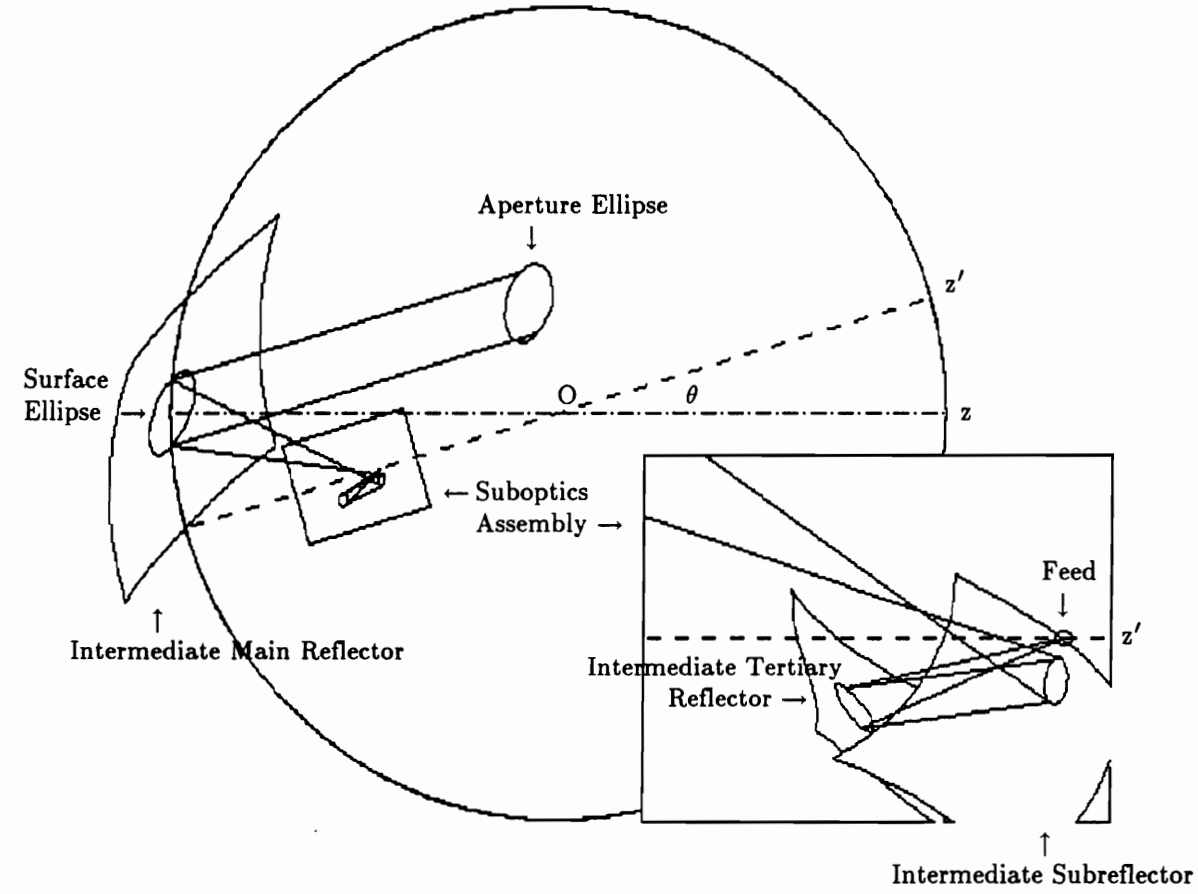

(a) The 3D view of the intermediate configuration for a small θ-scan angle and ϕ=0°

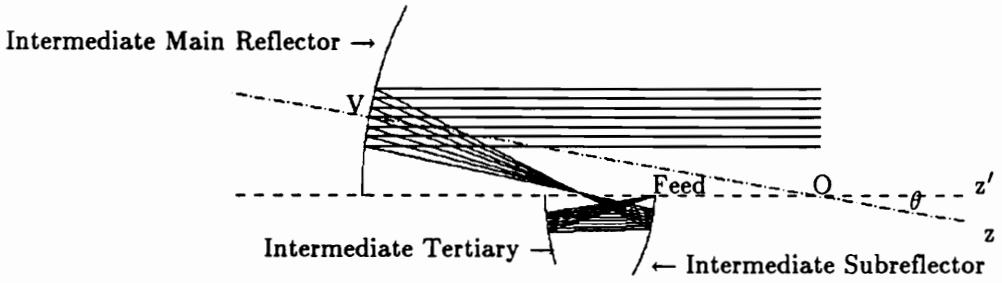

(b) Profile view in the plane containing the z′ and z axes for the case in Figure 4a

Figure 5-3. The intermediate reflector configuration for various scan angles. The whole intermediate configuration is moved as a unit (main reflector, suboptics, and feed) with, in addition, tilting of the feed pattern to maintain the illumination centered on point V. (The prime coordinates are fixed with the moving reflector configuration.) The output ray tube is always parallel to the z′ axis.

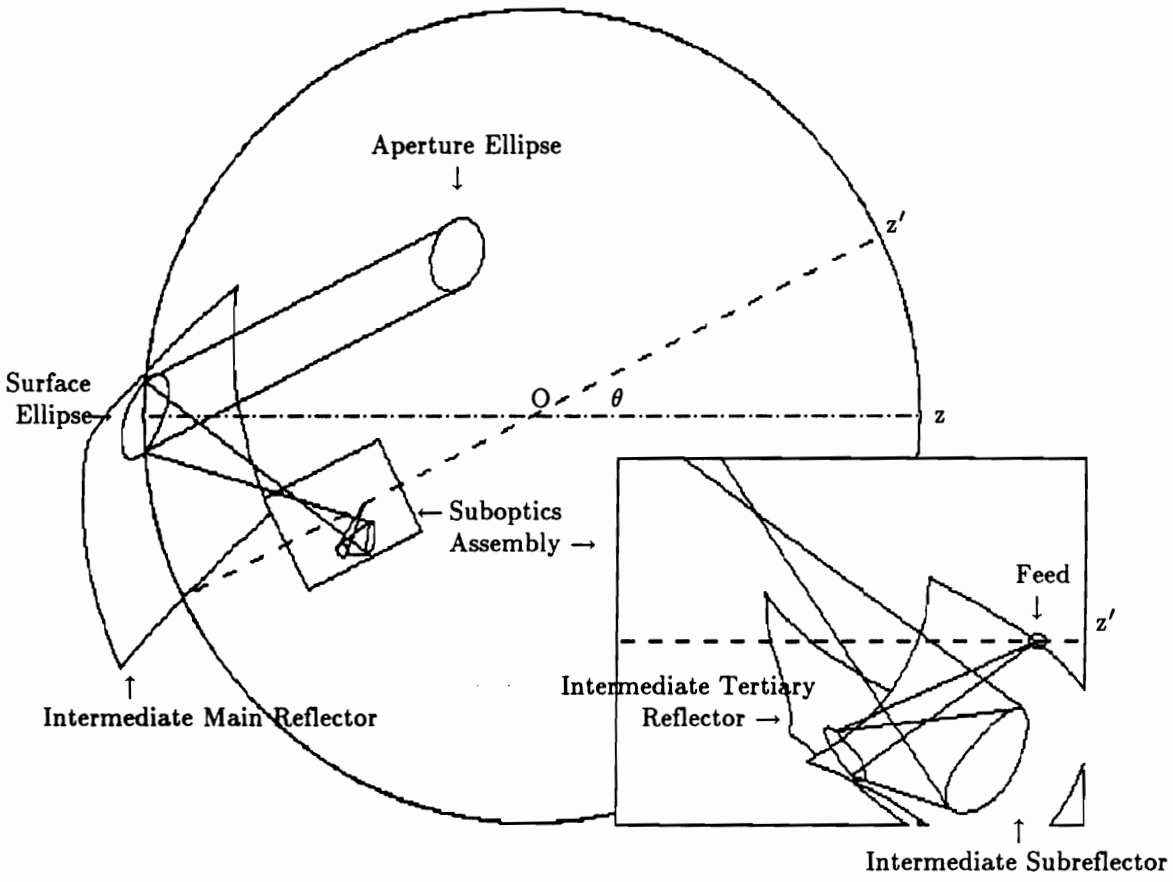

(c) The 3D view of the intermediate configuration for a large θ-scan angle and ϕ=0°

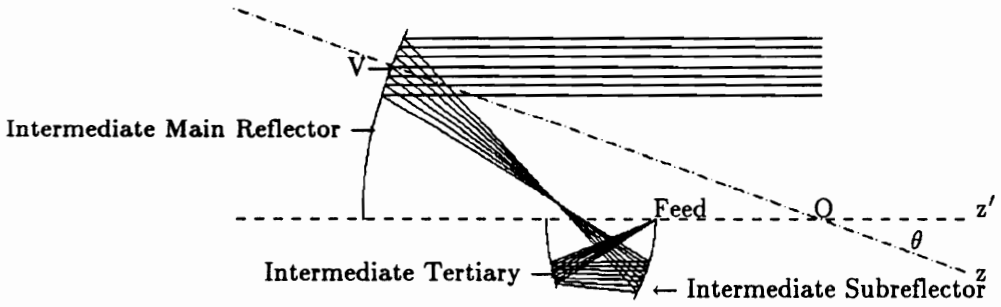

(d) Profile view in the plane containing the z′ and z axes for the case in Figure 4c

Figure 5-3. (Page 2)

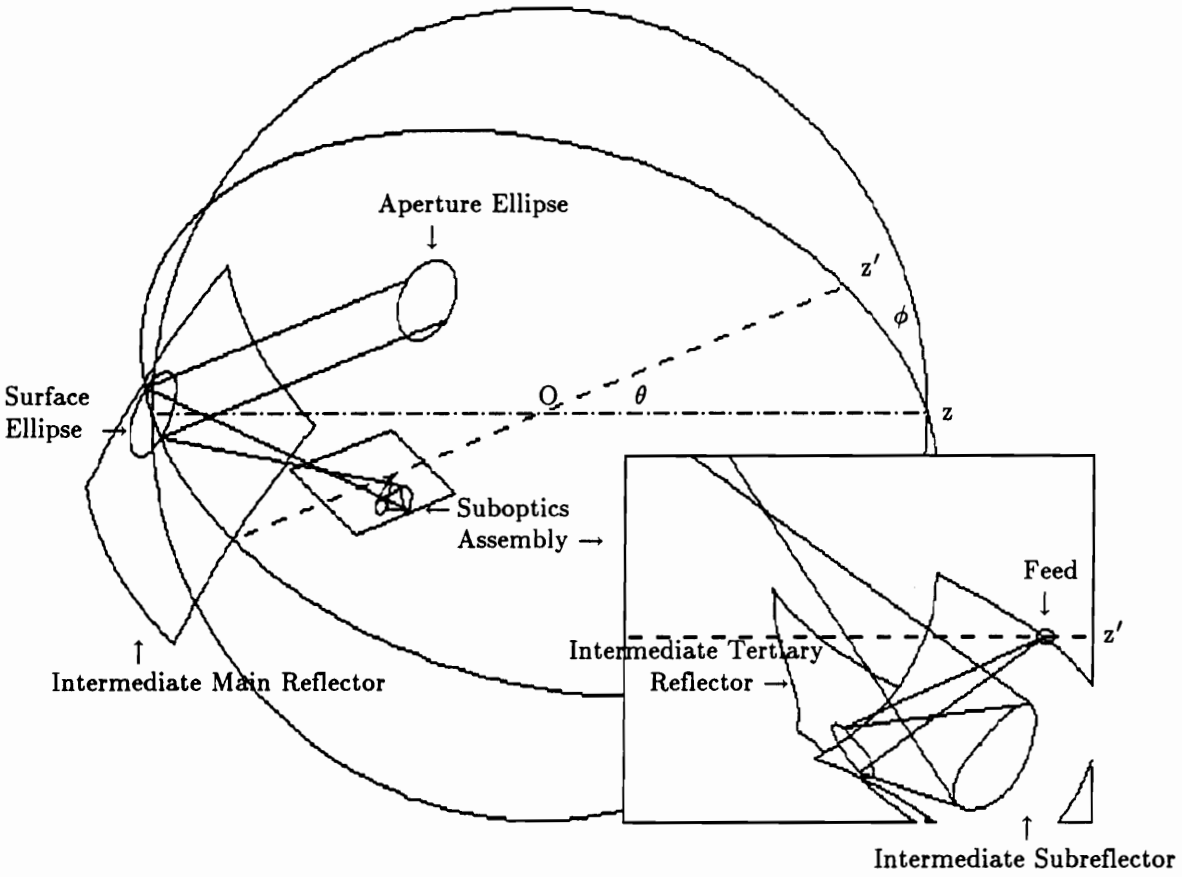

(e) The 3D view of the intermediate configuration for a large θ-scan angle and $\phi>0^{\circ}$

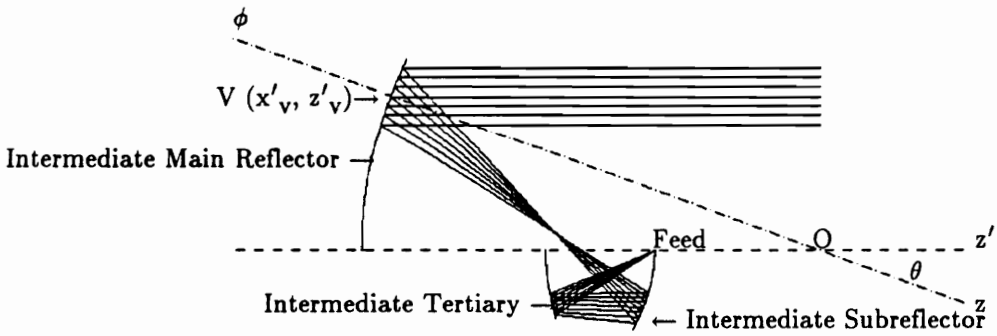

(f) Profile view in the plane containing the z′ and z axes for the case in Figure 4e

Figure 5-3. (Page 3)

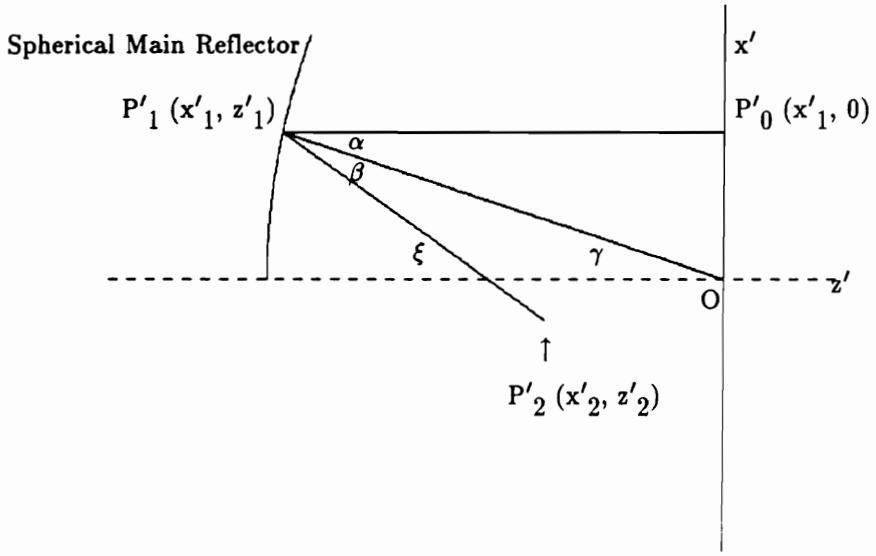

Figure 5-4. The geometry for the derivation of (5-9). See Appendix 5A.

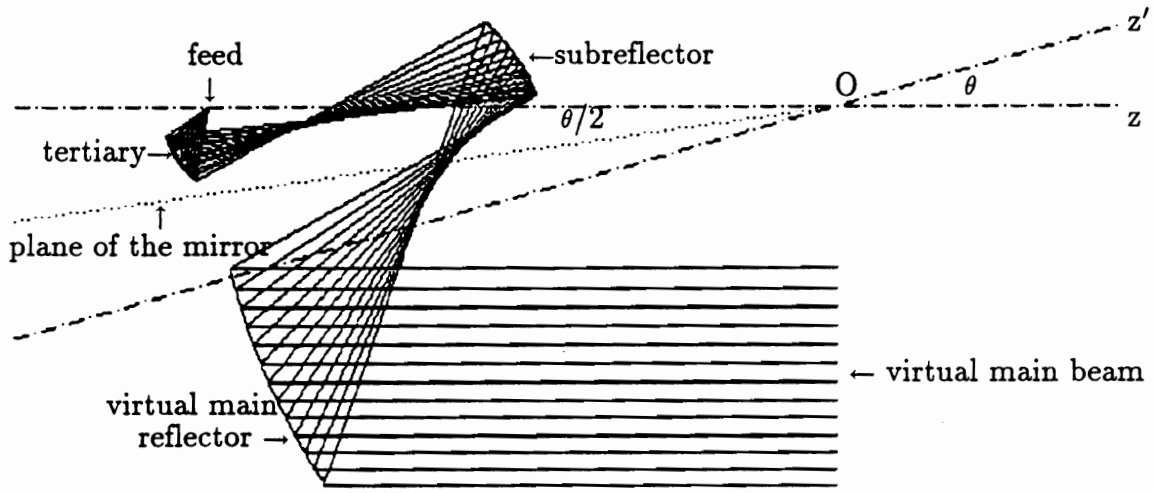

a. Basic spherical tri-reflector system.

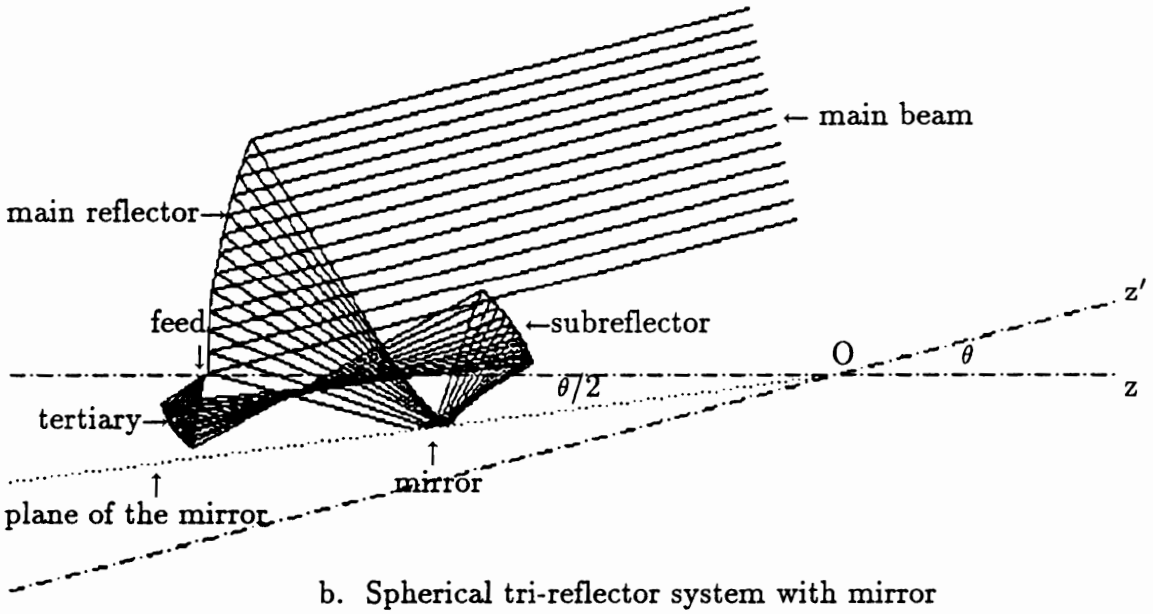

b. Spherical tri-reflector system with mirror

Figure 6-1. The scan principle of the mirror in a spherical tri-reflector system

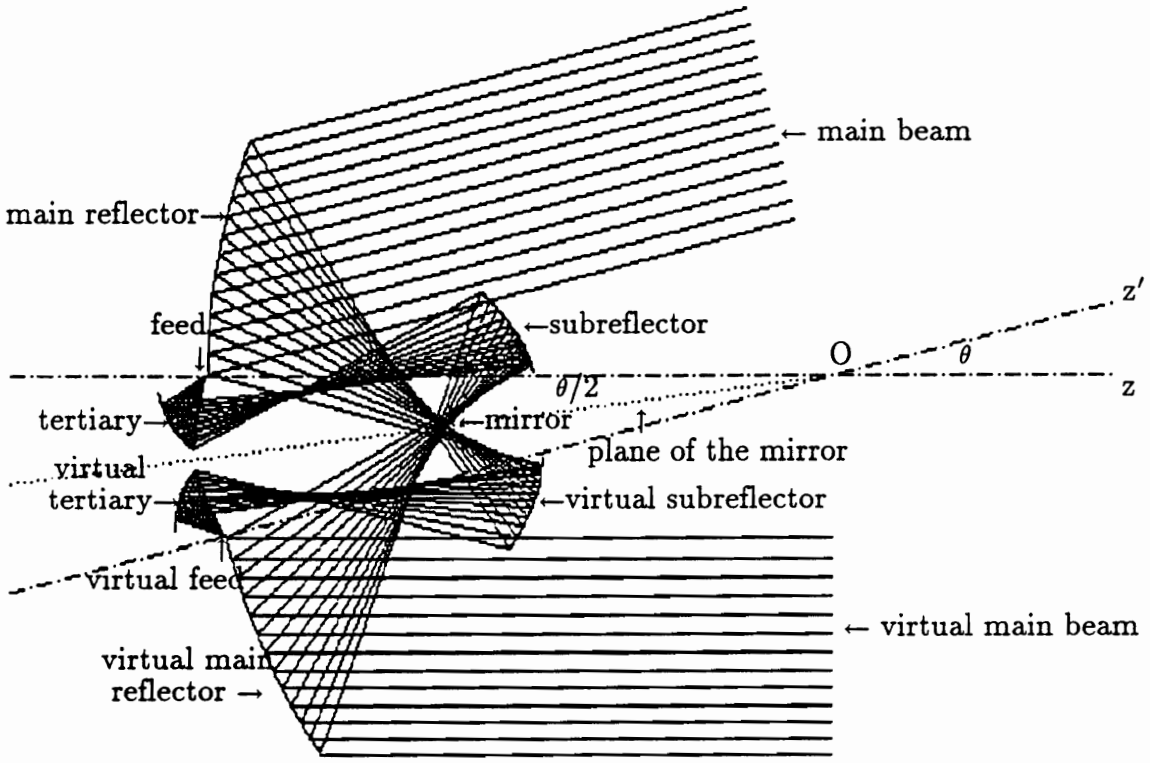

c. Illustration for mirror imaging scanning process

Figure 6-1. (continued)

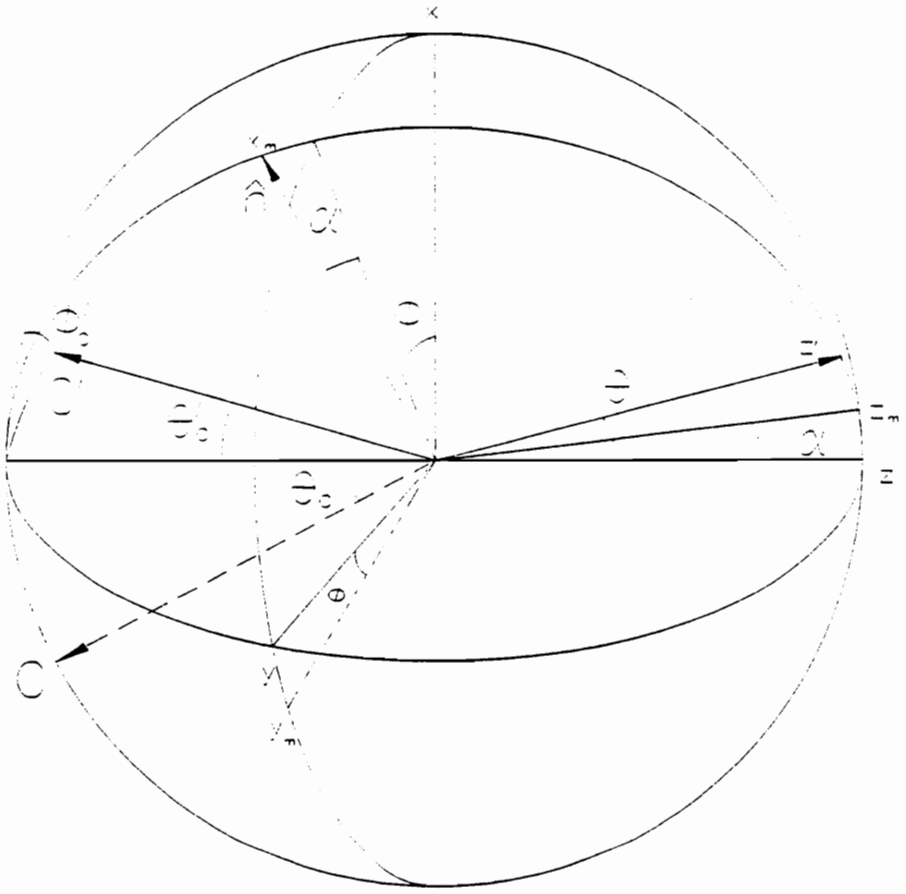

Fig. 6-1 Geometry for Mirror Coordinates and Antenna Coordinates

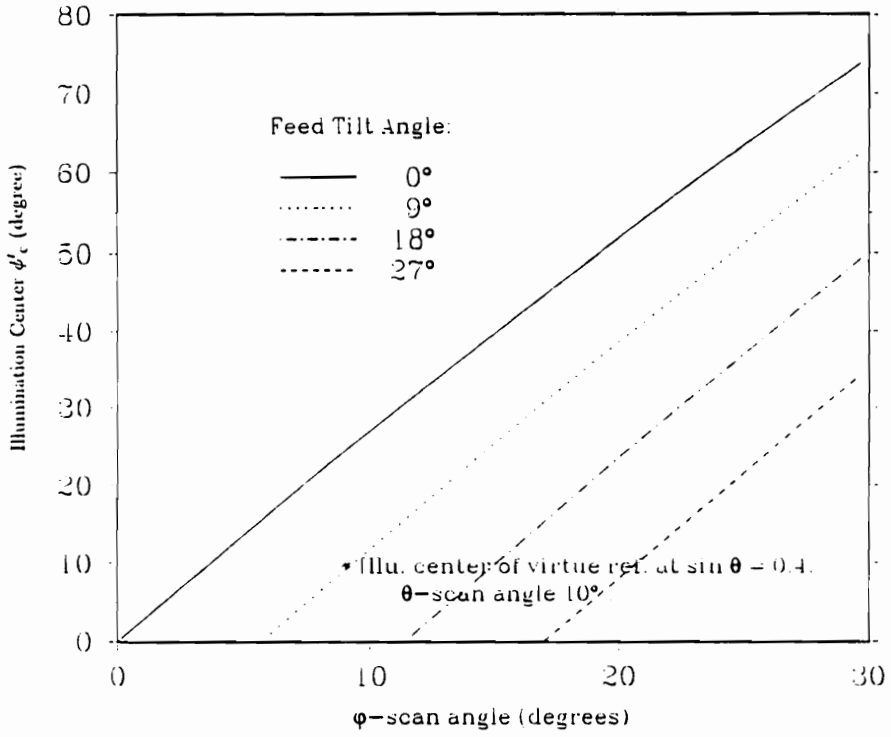

Fig. 6-3 Motion of illumination center ϕ'_c with ϕ-scan for various feed tilt angles

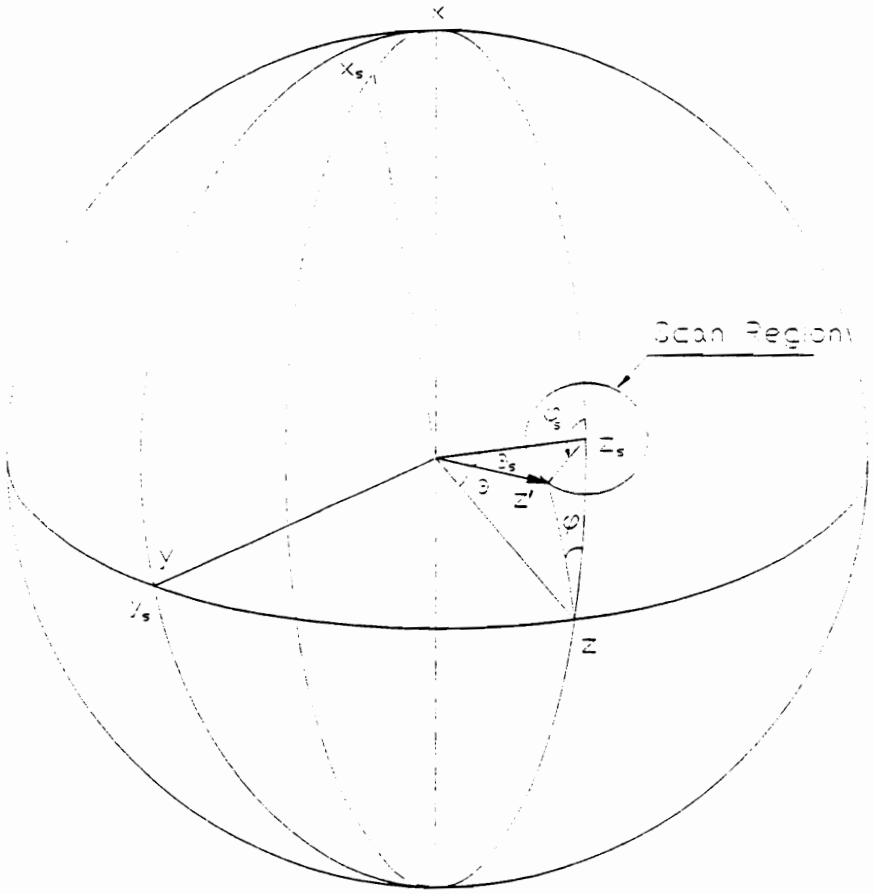

Fig. 6-4 Geometry for Scan Coordinates and Antenna Coordinates

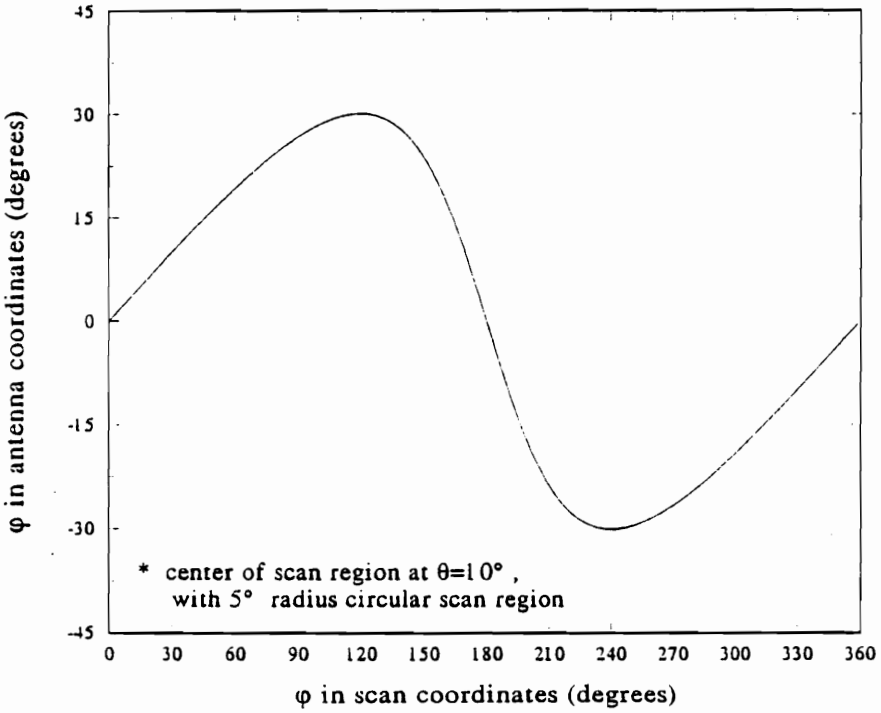

Fig. 6-5. Dynamic range of antenna φ coordinate

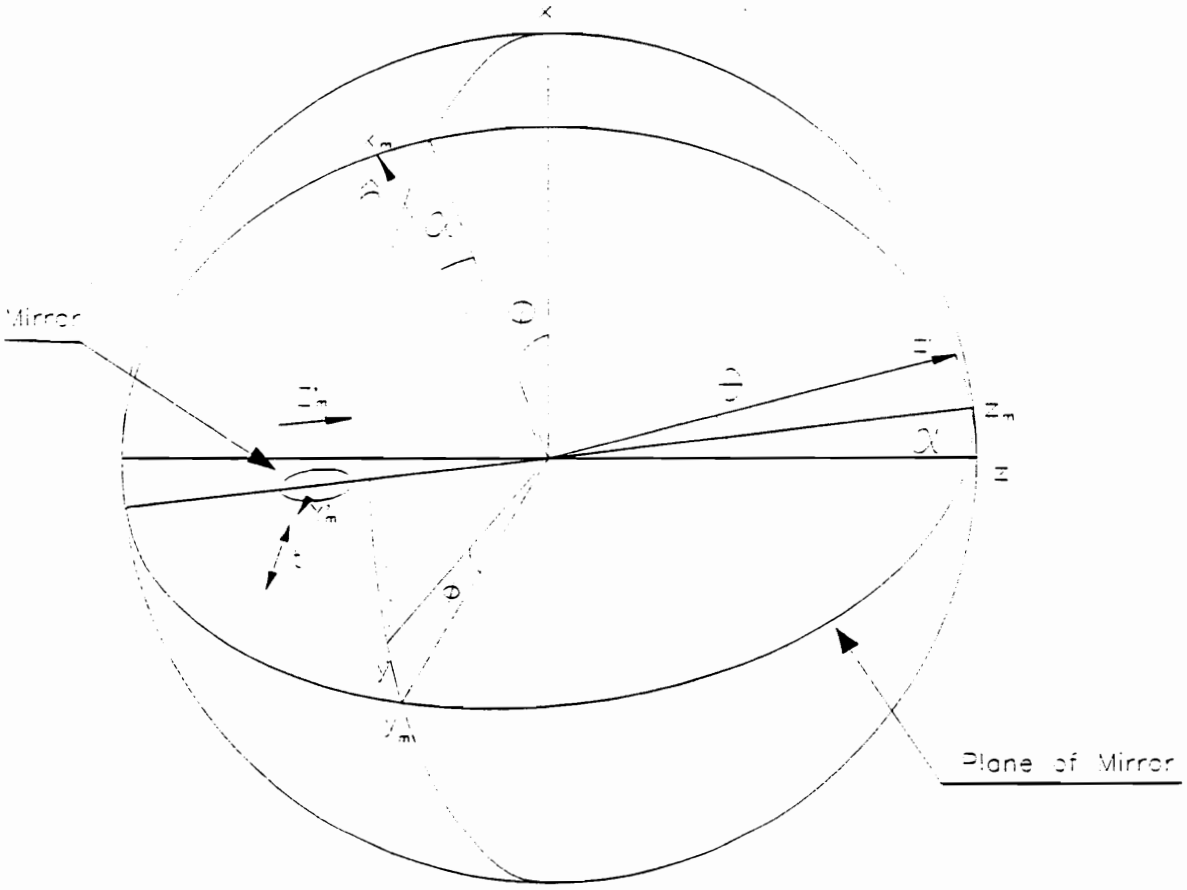

Fig. 6-6 Geometry for Mirror Translation and Rotation Axes

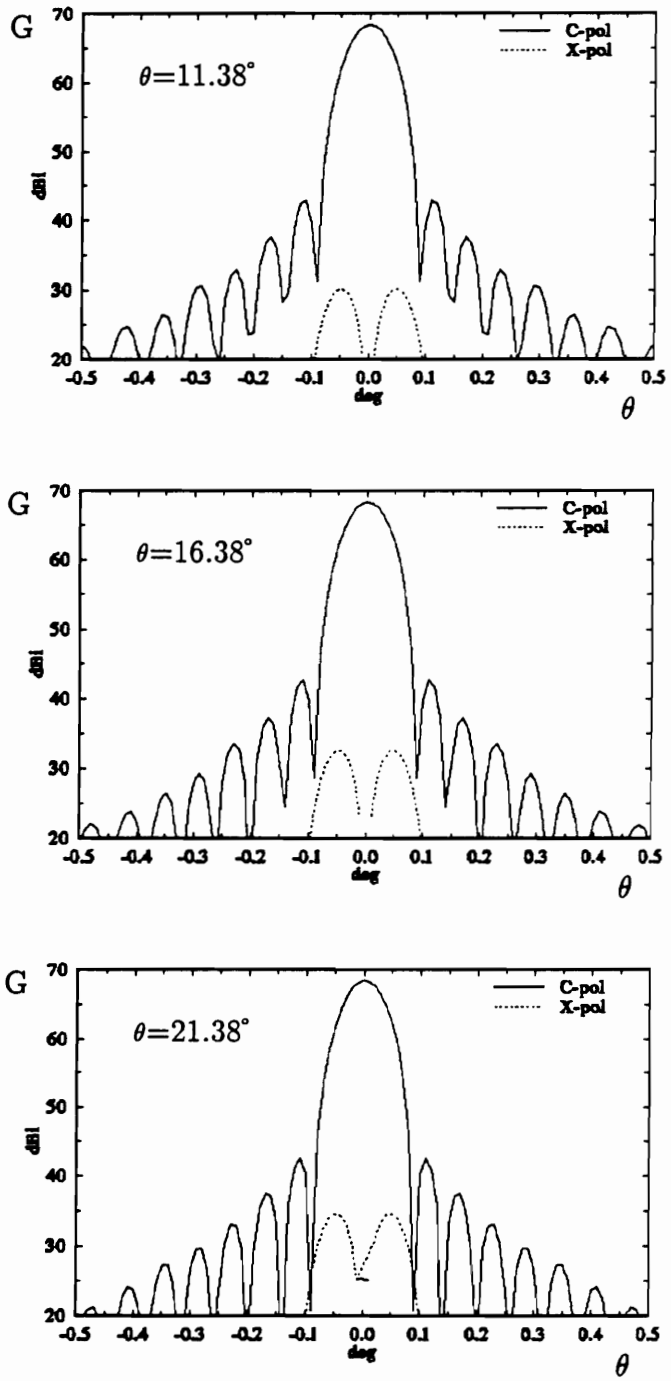

Figure 7-1. H-plane patterns of the tested single caustic configuration of Table 7-1 for various scan angles

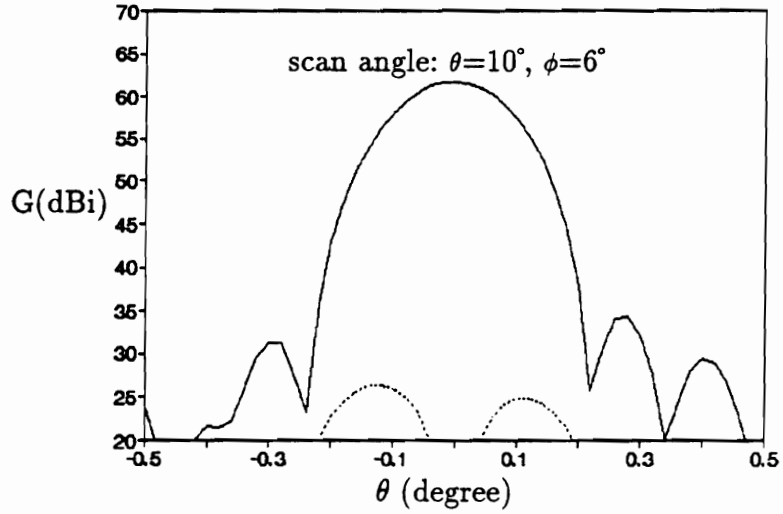

E plane pattern for spherical tri-reflector system with mirror

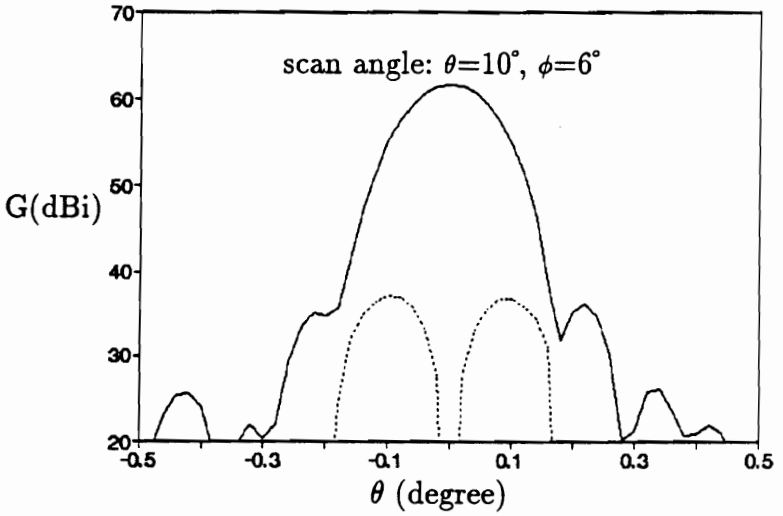

H plane pattern for spherical tri-reflector system with mirror

Figure 7-2. Patterns for the spherical tri-reflector system with mirror of Table 7-2 and as shown in Fig. 6-1. The solid (dashed) curves are Co (Cross) polarized patterns

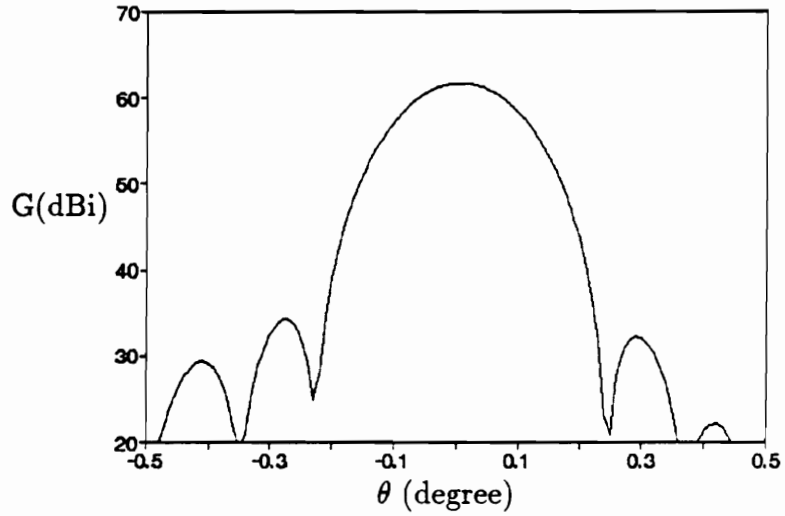

E plane pattern for spherical tri-reflector system without mirror

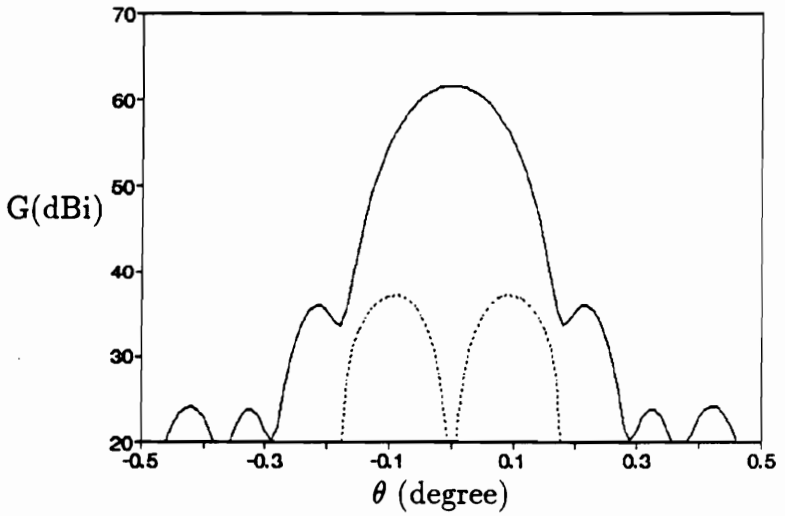

H plane pattern for spherical tri-reflector system without mirror

Figure 7-3. Patterns for the parent spherical tri-reflector system without mirror of Table 7-2 and as shown in Fig. 6-1c

VITA

Bing Shen was born in Shanghai, China. He attended Shanghai Jiao Tong University in 1985-1988, where he got his Bachelor degree in applied physics. He entered Virginia Polytechnic Institute and State University in Fall of 1989, and joined the Satellite Communications Group in 1990. He received his Master's degree in electrical engineering in 1991. He performed graduate research in wide scanning remote sensing antennas and radio wave propagation.